Emittance Measurements at Laser-Wakefield Accelerators

by

Paul Viktor Winkler

A Thesis Submitted to the Faculty of

Mathematics, Informatics and Natural Sciences

Department of Physics

for the Degree of

DOCTOR RERUM NATURALIUM

Universität Hamburg

November 2019

Gutachter der Dissertation:	Dr. Andreas Maier
	PD Dr. Bernhard Schmidt
Zusammensetzung der Prüfungskommission:	Prof. Dr. Daniela Pfannkuche
	Prof. Dr. Jochen Liske
	Prof. Dr. Jörg Rossbach
	PD Dr. Bernhard Schmidt
	Dr. Andreas Maier
Vorsitzende der Prüfungskommission:	Prof. Dr. Daniela Pfannkuche
Datum der Disputation:	17.12.19
Vorsitzender des Fach-Promotionsausschusses Physik:	Prof. Dr. Günter H. W. Sigl
Leiter des Fachbereichs Physik:	Prof. Dr. Wolfgang Hansen
Dekan der Fakultät MIN:	Prof. Dr. Heinrich Graener

Eidesstattliche Versicherung / Declaration on oath

Hiermit versichere ich an Eides statt, die vorliegende Dissertationsschrift selbst verfasst und keine anderen als die angegebenen Hilfsmittel und Quellen benutzt zu haben.

Die eingereichte schriftliche Fassung entspricht der auf dem elektronischen Speichermedium.

Die Dissertation wurde in der vorgelegten oder einer ähnlichen Form nicht schon einmal in einem früheren Promotionsverfahren angenommen oder als ungenügend beurteilt.

Hamburg, den 11.11.19 _____

Paul Viktor Winkler

Abstract

Laser-wakefield accelerators enable the generation of electron beams with initially nm-small emittances and GeV-level beam energies within cm-scale distances and are therefore promissing candidates for drivers of future experiments. However, the percent-level energy-spreads and shot-to-shot fluctuations in beam quality can pose a limit to the transportability of plasma-generated beams, and further impete the measurement of the beam emittance using conventional methods.

In the framework of this thesis, two energy-resolved phase-space diagnostics, a single-shot and a multi-shot method, have been implemented at the LUX laser-plasma accelerator. Electron beams from ionization injection are imaged by a compact quadrupole doublet from a virtual source into a dispersive electron spectrometer, which allows to measure the beam emittance, beam size, divergence and phase-space correlation on the single energy-slice level. The results from both methods agree within 3 %, which verifies the applicability of the single-shot method at our setup and prooves the reproducability of the generated electron beams. A complex variation of the phase-space within the broad energy spectrum is observed.

The implemented diagnostics further allow to measure the chromatic effects of the transport optics on the beam phase-space and a first measurement of the chromatic emittance is presented. For a 2 %-energy-spread sub-interval of the spectrum the normalized beam emittance grows by 10 % from (0.83 ± 0.07) mm mrad to finally (0.93 ± 0.07) mm mrad inside the capturing optic and is conserved afterwards.

With the achieved measurement precision, based on a detailed accuracy study and calibrated with high statistic scans, a reliable phase-space diagnostic has been developed for emittance optimization for future experiments at LUX.

Zusammenfassung

Laser-Plasma-Beschleuniger ermöglichen das Erzeugen von hoch energetischen (GeV-Level) Elektronenstrahlen mit nm-Skala Emittanzen innerhalb von Beschleunigungsstrecken von wenigen cm und sind daher vielversprechende Kandidaten für Treiber zukünftiger Experimente. Die relative Breite der Energieverteilung der Elektronen im %-Bereich sowie Schuss-zu-Schuss-Fluktuationen in der Strahlqualität erschweren jedoch den Strahltransport Plasma-beschleunigter Elektronen sowie die Messung der Strahlemittanz mit konventionellen Methoden.

Im Rahmen dieser Arbeit wurden zwei Energie-aufgelöste Phasen-Raum Diagnostiken, eine Single-Shot und eine Multi-Shot Methode, am LUX Laser-Plasma-Beschleuniger implementiert. Durch Ionisationsinjektion erzeugte Elektronenstrahlen werden von einer virtuellen Quelle mit einem kompakten Quadrupol-Magnet-Dublett in ein Elektronenspektrometer fokussiert, was die gleichzeitige Messung der Strahlemittanz, Strahlgröße, Strahldivergenz und Phasen-Raum-Korrelation einzelener Energie-Intervalle ermöglicht. Die Ergebnisse beider Methoden stimmen zu 3 % überein, was die Anwendbarkeit der Single-Shot Methode als auch die Reproduzierbarkeit der Elektronenstrahlqualtität in unserem Experiment verifiziert. Gleichzeitig wurde eine komplexe Variation der Phasen-Raum-Parameter innerhalb des breiten Energiespektrums gemessen.

Die eingestzte Diagnostik ermöglicht ferner die Messung der chromatischen Effekte des Strahltransports auf den Phasen-Raum, welches eine erste Messung des chromatischen Emittanzwachstums ermöglichte. Im Falle eines 2 %-Energie-Intervals des Spektrums wurde ein Wachstum der normierten Emittanz um 10 % von (0.83 ± 0.07) mm mrad auf (0.93 ± 0.07) mm mrad innerhalb der Fokussieroptik gemessen.

Mit der erreichten Messgenauigkeit, basierend auf einer detaillierten Fehler-Analyse und kalibriert durch Messungen mit hoher Statistik, wurde eine zuverlässige Phasen-Raum Diagnostik entwickelt, welche zur Emittanzoptimierung bei zukünftigen Experimenten am LUX Beschleuniger genutzt werden kann.

Contents

List of Figures

List of Tables

1. Introduction

Highly relativistic electron beams are drivers for modern research facilities [1, 2, 3]. The required electron energies are typically achieved within km-long particle accelerators. Here, the electron beam is repeatedly focused along the accelerator and the motion of the electron beam can be complex. However, the beam emittance, which is a measure of the volume that is occupied by the beam in phase-space, i.e. the space spanned by the electrons' position and momentum, is a conserved quantitiy, for example in the absence of accelerating fields and in case of a small energy variation within the beam [4]. In order to account for a change in beam energy, the normalized emittance is defined as

$$\varepsilon_n = \gamma\,\varepsilon \quad ,$$

where γ is the relativistic Lorentz factor and ε the emittance. The normalized emittance is therefore an important parameter of the electron beam dynamic, because, once determined, for example at the electron source, can be used to compute the electron beam size everywhere along the accelerator, for example at the final focus.

In case of a fixed focusing optics, small normalized emittances are required to minimize the final focus size and to therefore maximize the electron density at the experiment [5, 6]. As an example, normalized slice emittances of 0.2 mm mrad to 0.4 mm mrad from the SLAC injector [7] and normalized emittances of 0.4 mm mrad to 0.6 mm mrad from the injector at the European XFEL [8] have been published recently.

The accelerating fields that can be achieved with conventional RF accelerator technology however are limited to the 100 MeV/m-level [9]. Thus, km-distances are required to accelerate the electrons to energies in the multi-GeV-range. The resulting costs of such facilities on the billion dollar level can only be financed by large international research collaborations. Consequently, only very few of these drivers exist, which limits their availability for researchers.

Hence, alternatives are required to exceed the accelerating field limits of the conventional accelerator technology. Promising candidates are laser-plasma accelerators [10, 11, 12]. Here, electrons are accelerated in the field inside a plasma wave that is excited by an intense laser pulse. Within cm-length scales, accelerating fields of up to 100 GeV/m [13, 14, 15] and electron energies up to 8 GeV [16] have been reported. Plasma-accelerated beams with kA-beam currents, nC-charges, fs-level bunch lengths [17, 18] and normalized emittances on the mm mrad-level [19], [20] have been demonstrated.

However, modern applications also require reproducable electron beams at kHz-repetition rates with sub-percent-level energy-spreads [21]. The latter is typically not achieved by state-of-the-art laser-wakefield accelerators. Energy-spreads on the few percent-level [22, 23, 24, 25] and shot-to-shot fluctuation in beam quality are typically reported [26, 27].

The comparibly large energy-spread and the shot-to-shot instability of laser-wakefiled accelerated beams further impede the measurement of the beam emittance. A standard method to measure the emittance at conventional mashines is a quadrupole-scan [28, 29]. Here, the beam-size on a screen is varied by changing the focusing with a quadrupole magnet. The detected beam distribution on screen is a function of the focusing optic and the beam phase-space, which allows to reconstruct the latter. However, in case of a large energy-spread, focusing of the beam will result in different beam energies to be focused at different positions along the beamline, which is called chromaticity [30]. The detected beam size on screen of a multi-percent energy-spread beam will thus smear out [31]. Further, a quadrupole-scan is a multi-shot measurement and requires stable electron beams. Accordingly, new emittance diagnostics had to be developed to measure the emittance of laser-wakefield accelerated beams from a single shot.

For example, pepper-pot masks are used to devide the beam into many beamlets and to thereby sub-sample the electron phase-space [32, 33]. These measurements are however limited in emittance accuracy, in particular for low emittance and high energy beams [34].

Another method to measure the emittance is the detection of the betatron radiation emitted from the electron oscillations inside the plasma. Spectrally resolving [35, 36] or penumbral imaging [37, 38] the betatron radiation enables to infer the electron beamsize inside the plasma channel. The beam divergence is measured from the electron distribution on a profile screen after the plasma. However, here, a very likely modulation of the electron phase-space by the plasma-to-vacuum interface [39, 40] is not included in the measurement.

The pepper-pot as well as the betatron spectroscopy method further can only retrieve the beam emittance integrated over the full energy spectrum. Considering the full spectrum of multi-percent energy-spread beams for the emittance determination is however questionable. It is not proven that the electron phase-space is the same for all energies. For most applications, the electron beam has to be transported from the source to the experiment with a transport optic, which can typically only transport a limited variation in beam energy, in particular due to chromatic effects. It is therefore not ensured, that the phase-space available for the experiments is the phase-space measured by the two diagnostics discussed above.

Another method to measure the emittance was introduced by Weingartner et al. [19]. A conventional quadrupole-scan is performed, but the beam is additionally dispersed in an electron spectrometer. The beam size on screen can therefore be detected for

individual energy slices, circumventing the challenge of the large energy-spread. However, only the electron phase-space in the non-dispersive axis of the spectrometer can be measured. Weingartner further proposed to reconstruct the emittance from a single shot by simultaneously detecting the beam size for multiple energy slices on the spectrometer screen.

However, in order to apply the single-shot method, it has to be assumed that the initial phase-space properties, namely the beam size, divergence and emittance are the same for all energy slices that are considered for the single-shot retrieval. Weingartner compared the single-shot method to a quadrupole lense position scan at three different energies. Both methods results agreed by $\pm 10\,\%$. However, it has not been shown that the initital phase-space of the single energy-slices that are considered for the single-shot retrieval are independent of the slice-energy.

Another challenge that comes with the large energy-spread of laser-wakefield accelerated beams is the so called chromatic emittance growth. As mentioned above, in case of a large energy variation within the bunch, the foci of the different electron energies are spread along the accelerator. The spatial and angular distribution of the single energy-slices thus differ which causes the energy-projected emittance to grow. This effect is typically not an issue for conventional machines with permille-level energy-spread beams. For laser-plasma accelerators however, chromatic emittance growth has to be considered. According to particle tracking simulations of electron beams with parameters that were determined from experiments, chromatic emittance growth of laser-wakefield accelerated beams has been considered a show-stopping argument for future applications [41, 42]. However, to the authors knowledge, no measurement of the chromatic emittance growth has been shown up to date.

In order to experimentally quantify the chromatic emittance growth of laser-wakefield accelerated beams, measurements at the LUX accelerator were performed. A quadrupole-scan and a single-shot diagnostic were implemented. LUX is a laser-plasma accelerator dedicated for the generation of undulator radiation and is built by the University of Hamburg, in close cooperation with DESY. The LUX facility is further designed for long-term stable electron generation. Recently, more than 24 hours of stable electron acceleration has been demonstrated [43]. The implemented emittance diagnostic follows the concept introduced by Weingartner et al.

Due to the stability of the electron beams, a high statistic quadrupole scan is performed in order to measure the energy-slice phase-space and to compare it to the single-shot method. The electron phase-spaces are measured from a virtual source, allowing for an initial phase-space correlation of the electron beams out of the plasma. In addition, the chromatic effects on the electron phase-space are analysed for both the energy-slice and projected electron phase-space.

The scope of this thesis is the developement of a reliable phase-space diagnostic as a tool for future emittance optimization of the generated electron beams at LUX. Herefore, an in depth analysis of the measurement accuracy in the phase-space retrieval was performed and the influence on the emittance error by the initial electron beam properties as well as the imaging optics and the detector calibration are examined.

The thesis is structured as follows: In chapter 2 an introduction into laser-wakefield acceleration, the ANGUS driver laser, and the LUX beamline is given. The chapter closes with a discussion of the energy-slice phase-space from laser-plasma accelerated beams obtained from particle-in-cell simulations. The electron beam optics and electron beam diagonstics used for the emittance measurements are presented in chapter 3. The concepts of the beam emittance, beam transport and the applied emittance diagnostics methods are discussed in chapter 4. The results from the quadrupole-scan and the single-shot method as well as the chromatic emittance analysis are presented in chapter 6. A final conclusion is given in chapter 7.

2. Laser-Wakefield Acceleration at LUX

Laser-wakefield acceleration (LWFA), also called laser-plasma acceleration (LPA), is a novel and developing technology to generate GeV-level electron beams on the few mm-scale. A detailed summary of laser-wakefield acceleration is beyond the scope of this thesis and the reader may find additional information in [44, 45]. Only the very basic physics of intense laser pulses in a plasma relevant for the experiment and the later analysis are summarized in section 2.1. The basic layout of the ANGUS driver laser is summarized in 2.2. An overview on the LUX accelerator is given in section 2.3. A short introduction into particle in cell (PIC) simulations and a discussion of the simulated electron phase-space from the latter is presented in section 2.4.

2.1. Laser-Wakefield Acceleration

Intense laser pulses can be used to accelerate electrons inside plasma waves. Therefore, high power laser pulses are focused down to tens of µm spot sizes in order to result peak intensities on the $1 \times 10^{18}\,\mathrm{W/cm^2}$-level. Figure 2.1 illustrates the interaction between an intense laser pulse and a plasma. Due to the high laser intensity, plasma electrons are transversely pushed from the laser axis into the direction of the negative intensity gradient, by a ponderomotive force [44]

$$\boldsymbol{F}_p = -m_0 c^2 \boldsymbol{\nabla} \left(a^2/2\right) \quad , \tag{2.1}$$

where m_0 is the electron rest mass, c is the speed of light in vacuum, and a is the normalized vector potential of the laser field. In the highly non-linear regime, when the peak normalized vector potential

$$a_0 \simeq 0.85 \cdot \lambda[\mu\mathrm{m}] \sqrt{I_0[10^{18}\,\mathrm{W/cm^2}]} \gg 1 \quad , \tag{2.2}$$

electrons are fully evacuated along the laser propagation and a positively charged ion channel remains. Here, λ is the laser wavelength and I_0 the laser peak intensity at the focus. The delocated electrons are attracted by the ions and oscillate back to the laser axis, thereby forming a cavity with the length of the plasma wavelength λ_p with

$$\lambda_p[\mu\mathrm{m}] \simeq 33/\sqrt{n_0[10^{18}\,\mathrm{cm^{-3}}]} \quad , \tag{2.3}$$

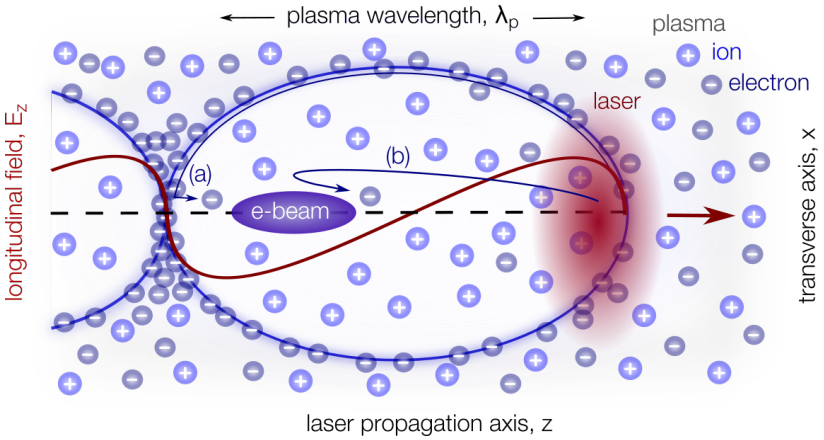

Figure 2.1. – Illustration of a laser pulse forming a plasma cavity. The plasma electrons (-) are displaced by the laser (red) and oscillate back to the laser axis on the length of the plasma wavelength λ_p. The heavy ions (+) remain and a strong longitudinal field (red curve) is generated along the cavity. Electrons can be either injected via self-injection (a) or ionization-injection (b).

where n_0 is the plasma density. For example, in case of a plasma density of $5 \times 10^{18}\,\mathrm{cm}^{-3}$ the plasma wavelength is 15 µm. Inside the plasma cavity strong longitudinal electric fields E_z with

$$E_z[\mathrm{GV/m}] \simeq 96 \cdot \sqrt{n_0[10^{18}\,\mathrm{cm}^{-3}]} \quad , \tag{2.4}$$

with up to 200 GV/m, following the previous example, can be used to accelerate electrons in the direction of the laser [46].

An electron beam can either be externally [47, 48] or internally injected into the plasma cavity. For example, at the end of the plasma period the electron density peaks and electrons can scatter into the cavity (see case (a) in figure 2.1). If the electrons longitudinal velocity matches the phase-velocity of the cavity, respectively the group-velocity of the laser pulse, electrons can be accelerated in the propagation direction of the laser. This process is called self-injection and is a highly statistically dominated, respectively chaotic, mechanism, which typically results in unstable electron beam properties [49].

Another challenge in laser-wakefield acceleration is the continuous injection and acceleration of electrons in the plasma which results in large energy-spreads of the generated electron beams. Hence, work has been started on localizing the injection inside the plasma. For example, in a localized plasma density downramp the plasma period is elongated (see equation 2.3) and the cavity phase-velocity intermediately reduced such that also scattered electrons with a lower longitudinal velocity can be injected [50, 51]. Or, a second counter-propagating laser pulse is used to locally increase the laser intensity at the intersection point of the two lasers [24]. However, both methods are technically difficult to implement.

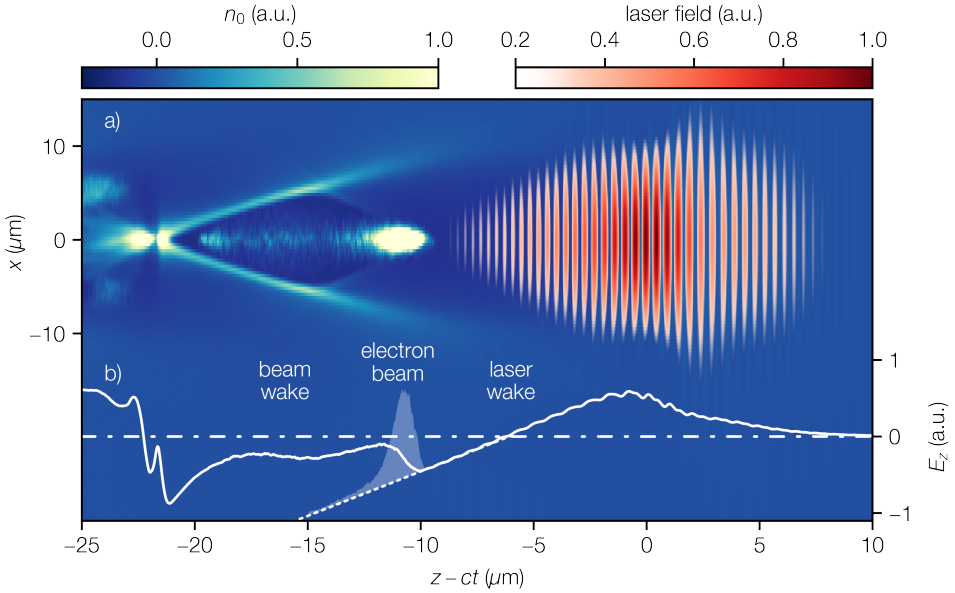

Figure 2.2. – PIC [53] simulation of a laser pulse driving a plasma wake. The longitudinal coordinate is shown in a co-moving frame $z - ct$. a) Normalized plasma electron density n_0. b) Longitudinal electric field lineout at the laser axis. The laser (red), traveling in positive z-direction, modulates the plasma density, such that electrons that are trapped inside the wake are accelerated in the direction of the laser. The electron beam drives an additional wakefield. FBPIC [53] simulation by courtesy of L. Jeppe.

At LUX, nitrogen doped hydrogen gas (see section 2.3) is used for the plasma and the electrons are internally injected via ionization injection [52, 18]. Here, the inner shell electrons of the nitrogen atoms are ionized at the very peak intensity of the laser pulse, i.e. within the plasma cavity. These inner shell electrons then fall back in the plasma cavity and are trapped in the accelerating phase of the field (see case (b) in figure 2.1). Ionization injection is thus not based on electron scattering and electron beams with a comparably higher shot-to-shot stability are generated. However, the inner shell electrons are passing the laser-field and can thereby gain transverse momentum. Thus, comparably larger beam emittances are expected from ionization injection, in particular in the laser polarization axis [20].

Particle-in-cell (PIC) simulations [53] are used (see section 2.4) to model the complex dynamics of the single electron trajectories in the non-linear regime. Figure 2.2 shows a PIC simulation of an accelerated electron beam inside a nitrogen-doped plasma. The laser and plasma properties in the simulation are chosen close to the parameters measured during the experiments. The picture shows the normalized plasma density (a) as well as the longitudinal electric field at the laser propagation axis z (b). The plasma density and fields are plotted in a co-moving frame and at the very end of the density plateau. The transverse laser field (red) is normalized to the laser peak intensity.

The electron density is modulated by the laser pulse. Directly behind the laser, the longitudinal electric field is positive and the field therefore decelerating for electrons. Further behind, the longitudinal field changes sign, which denotes the accelerating phase of the wake. The generated electron beam is located inside the accelerating phase roughly 10 µm behind the laser. At this region, the longitudinal electric field of the wake generated by the laser shows a linear slope (dashed line).

As can be seen, the electron beam is driving an additional wake field, called beam-loading [54], which deforms the wake of the laser. The charge profile of the electron beam inside the laser wake is highlighted by a transparent white area in figure 2.2b. The longitudinal field is varying along the electron bunch and deviating from the linear slope of the wakefield generated by the laser.

In addition to the longitudinal electric field, also strong transverse electric field gradients are present inside the plasma cavity. These transverse electric field gradients on the order of 100 MV/(m µm) [55] are constantly focusing the electron beam. The transverse phase-space volume that can be filled by electrons is determined by these transverse field gradients [56]. The matched beta-funtion β_m [56, 55] inside the focusing channel is proportinal to the square root of the relativistic electron energy $\gamma m_0 c^2$ and inversely proportional to the square-root of the transverse electric field gradient $\partial_r E_r$.

$$\beta_m = \frac{1}{\sqrt{K}} \quad , \quad K = \frac{e}{\gamma m_0 c^2} \partial_r E_r, \tag{2.5}$$

where e is the charge of a single electron, γ the relativistic Lorentz factor, m_0 the electron rest mass, and c the speed of light. Also the transverse field gradients are effected by beam-loading. The transverse phase-space, in particular the beam emittance can thus vary along the beam.

In general, the injection and acceleration processes in the plasma can be highly complex and in particular rely on non-linear mechanisms, as explained above. Small variations in the laser or plasma parameters can lead to an increased instability in electron beam parameters. For example, a fluctuation in laser intensity will cause the electron injection as well as the accelerating and focusing fields inside the plasma cavity to change on a single shot basis. Special demands on the stability of the driver-laser and plasma-source are therefore required in case of laser-plasma accelerators. The generation of reproducable electron beam quality is one of the key design aspects at LUX.

2.2. ANGUS Laser System

High power laser pulses are required in order to achieve the intensities capable to drive a plasma wakefield. Chirped-pulse-amplification (CPA) [57] enables the amplification of initially short fs-scale laser pulses to the PW-level. The laser pulses are stretched in time

by a dispersive optic, such that the longer wavelengths in the spectrum are delayed to the shorter. This allows the pulses to be amplified to orders of magnitude higher energies while the pulse intensity stays below the self-focusing and damage threshold inside the amplifier medium [58]. After amplification, a dispersive optic compresses the pulses to the fs-level again, in order to retain a high power laser pulse.

The ANGUS laser is a 100 TW-class Ti:Sa double CPA [60, 61] based laser system. A detailed description of the laser chain can be found in [59]. A schematic layout of the different amplifieres, pump lasers and pulse shapers is illustrated in figure 2.3. The laser pulses from the oscillator with a central wavelength of 800 nm are stretched in time and amplified by a regenerative amplifier. Afterwards, the pulses are compressed again and send into a cross-polarized wave generator (XPW) to improve the temporal and spatial contrast of the laser. Subsequently, the laser pulses are stretched again and send into a series of amplifiers. The original laser design has been upgraded with a set of diagnostics after each amplifier stage. The laser spectrum, near field, and far field are monitored and stabilized into the subsequent stage [43]. A dazzler [62], an acousto-optic programmable dispersive filter [63], is used to modulate the laser pulse spectrum and phase. A deformable mirror [64] is used to optimize the laser wavefront. The laser is finally compressed to a rms pulse length of 25 fs inside the in-vacuum compressor and sent into the laser transport beamline. The final laser energy into the second compressor can be reduced via an attenuator that transmits only a fraction of the incoming laser beam depending on the laser polarization that was rotated by a half-waveplate [59] before.

The maximum pulse energy available after the amplifier 1 is 1.4 J. The maximum pulse energy after the final amplifier 2 is up to 6.5 J. The last amplifiers can be operated with a maximum pulse repition rate of 5 Hz. However, studies by V. Leroux [65] showed that in case of a too large average power into the final compressor, heating and therefore deformation of the comressor grating substrate can cause a laser pulse quality degradation, in particular a deformation of the laser wavefront. Therefore, the laser repetition rate is typically reduced to 1 Hz in order to keep the average power into the final compressor and the time to reach thermal equilibrium on a reasonable level for experiments.

During the experimental campain in March 2019, whose results are presented in chapter 6, the last amplifier stage of the ANGUS laser was not available. The maximum energy into the final compressor was thus limited to 1.4 J by the previous amplifier stage. Owing to investigations by M. Kirchen, S. Jalas and P. Messner electron generation and experiments at LUX were still possible despite the absence of the last amplifier. The comparably low laser pulse energy, and the therefore reduced average power into the compressor, allowed to increase the laser repitition rate to the maximum of 5 Hz for the experiments.

After final compression, the laser is transported over 10 mirrors and a total length of 35 m into to the accelerator tunnel. At the end of the transport beamline the laser is

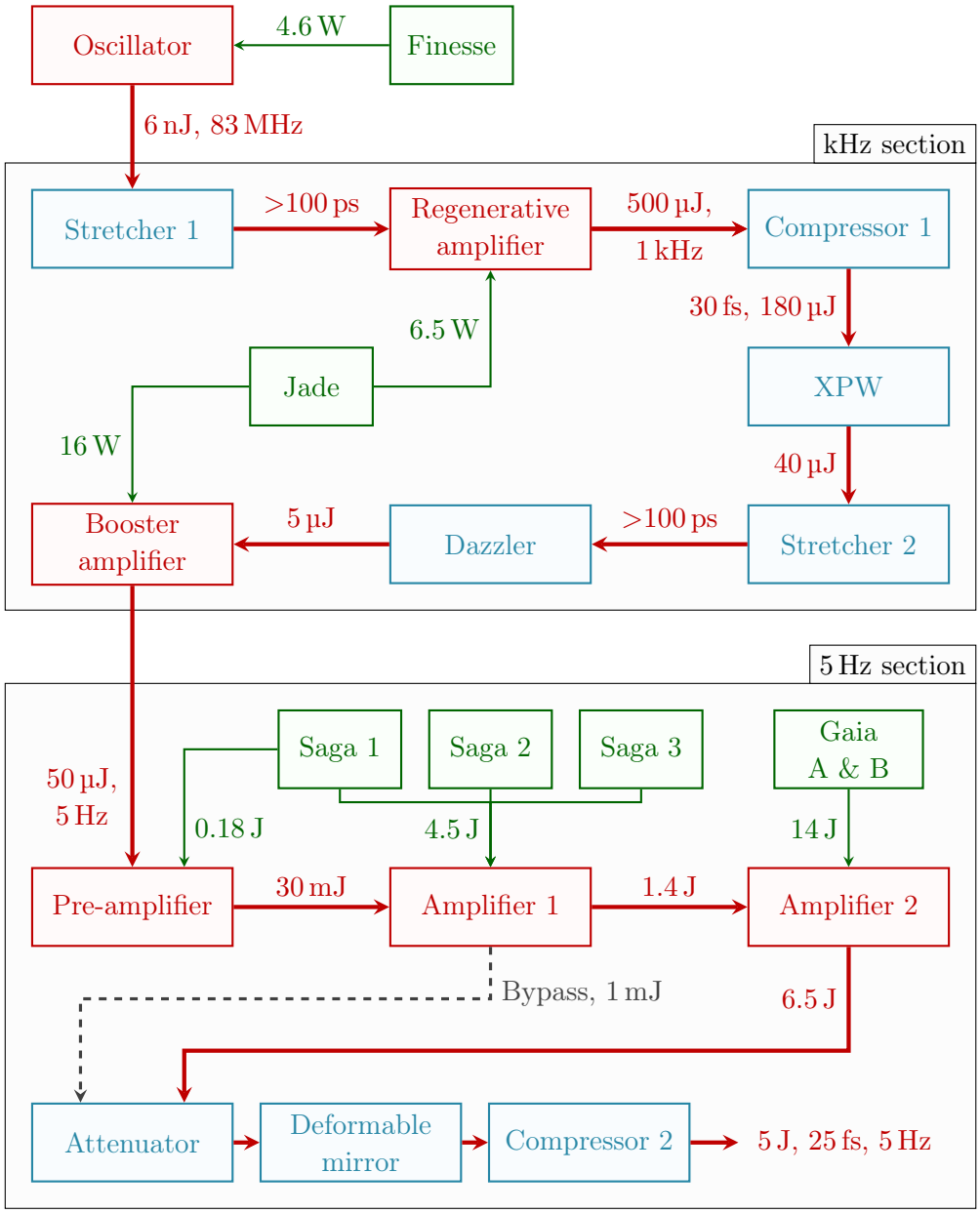

Figure 2.3. – Schematic of the ANGUS laser system. The laser oscillator and amplifiers are colored in red, the pump lasers in green and the pulse shaping components in blue. Figure taken from [59]; courtesy of V. Leroux.

Table 2.1. – List of key laser and plasma target parameters used for the emittance measurements in chapter 6. The laser parameters are given at the final focus at the plasma capillary.

	parameter	value
laser	central wavelength	800 nm
	pulse energy	0.88 J
	pulse length (rms)	30 fs
	focus size (fwhm)	25 µm
	pulse intensity	$4.7 \times 10^{18}\,\mathrm{W/cm^2}$
	a_0	1.35
	repition rate	5 Hz
plasma	gas species	95 % H_2 + 5 % N_2
	peak density	$4.8 \times 10^{18}\,\mathrm{cm^{-3}}$
	density plateau length	1 mm

finally focused by an off-axis parabolic mirror (OAP) with a focal length of 2 m to a radial fwhm focal spot size of 25 µm. The total efficiency of the in-vacuum compressor and the laser transport beamline is 60 %. The final laser energy at the plasma capillary is thus limited to 0.88 J, which results in a total laser intensity at the final focus of $I_0 = 4.7 \times 10^{18}\,\mathrm{W/cm^2}$. The normalized vector potential is $a_0 = 1.35$, accordingly. The most important laser parameters for the experiments presented in this thesis are summarized in table 2.1.

2.3. LUX Beamline Overview

The LUX electron source is a gas cell like plasma target with a 500 µm × 500 µm rectangular interaction capillary milled into a 10 mm × 10 mm large sapphire crystal plate, see figure 2.4. The target is operated with continous gas flow to ensure stable and reproducible plasma conditions, independent of the laser repetition rate. The structure of the target and the longitudinal density profile derived from CFD simulations [66] by P. Messner are shown in figure 2.5. Gas flow into the target is supplied through one inlet coming from the bottom which is splitted into two, resulting in an approximately 1 mm long plateau of constant density. The cut out volume at the exit of the target, leads to a smooth plasma-vacuum transition counteracting the rapid expansion of the electron beam into free drift. Electron beams are generated via ionization injection [52] in a hydrogen plasma, doped with 5 % of nitrogen. In the experimental campaign, the plateau pressure in the capillary was set to 81.4 mbar which yields a peak plasma electron density of $4.8 \times 10^{18}\,\mathrm{cm^{-3}}$.

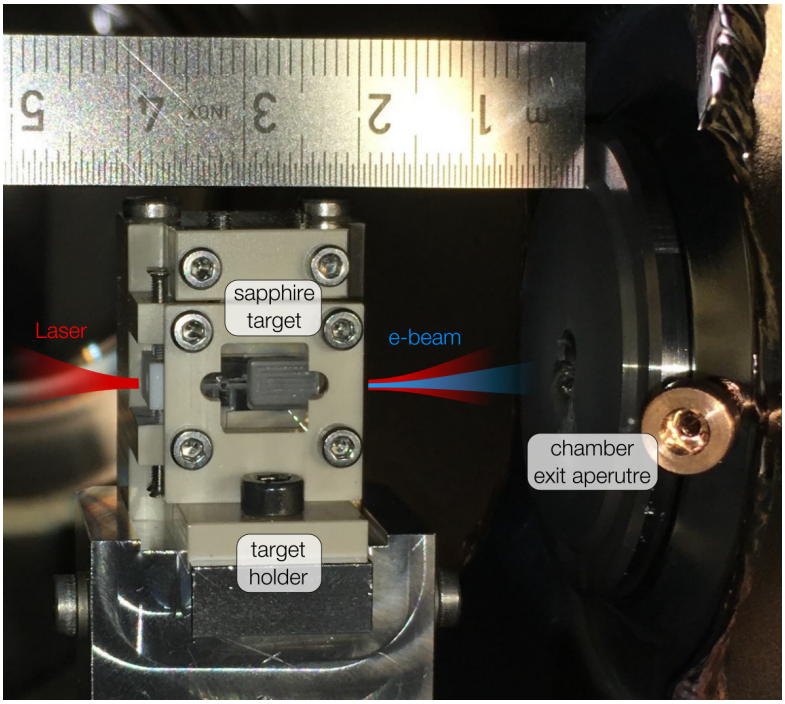

Figure 2.4. – Picture of the sapphire capillary target. Laser (red) and electron beam (blue) exit the chamber through the chamber exit aperture, that is part of a differential pumping system. Picture by courtesy of P. Messner.

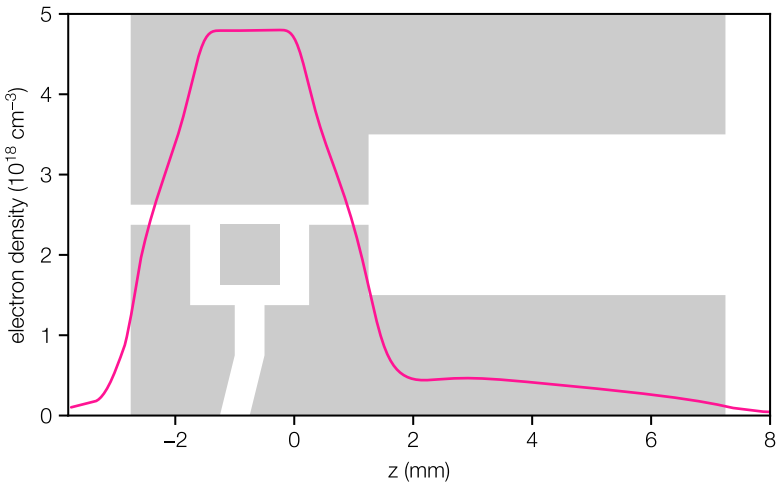

Figure 2.5. – OpenFoam [66] simulation of the gas density profile along the capillary target. The target geometry is illustrated in grey. The laser enters the capillary from the left. The gas density shows a constant plateau inbetween the two inlets and decreases slowly along the outlet at the exit side. Courtesy of P. Messner.

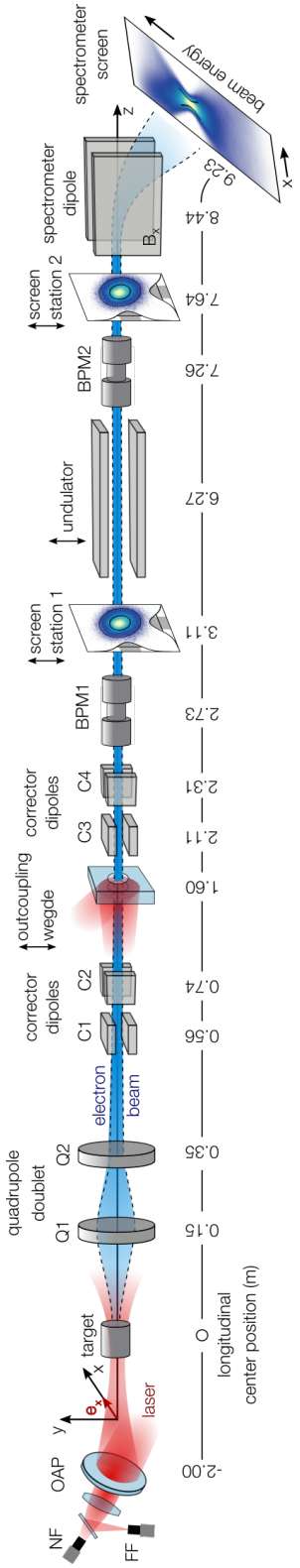

Figure 2.6. – Overview on the LUX beamline. The laser (red) is focused by the off-axis parabolic mirror (OAP) into the plasma target. The generated electron beams (blue) can be focused by two quadrupole magnets ($Q1$ and $Q2$) and steered by four corrector dipoles ($C1$-$C4$). The laser is outcoupled from the beamline after the first corrector pair. Two beam position monitors (BPM) measure the total charge and the center of charge of the beam. Two profile screen stations and an undulator can be driven in and out of the beamline. The electrons are finally deflected onto the spectrometer screen.

An overview of the LUX beamline is shown in figure 2.6. The laser pulses of the ANGUS laser are focused by the off-axis parabolic mirror (OAP) into the plasma channel. The near field and far field of the laser leakage through the parabolic mirror are used to measure the laser direction into the focus and the focus position. The generated electron beams are focused and transported to either the undulator [67] or the electron spectrometer. The LUX electron beam optics and beam diagnostics is built from conventional accelerator technology and discussed in detail in the following chapter.

The laser can be outcoupled from the beamline 1.6 m behind the plasma target and sent to a post-plasma diagnostics. The remaining laser pulse diverging from the plasma thus sets a lower limit on the free aperture of the beam optical elements before the outcoupling section. The undulator and the profile screen stations can be driven out of the beamline.

2.4. PIC Simulations

Particle-in-cell (PIC) simulations are a common tool to model the interaction of high intensity laser pulses in plasma channels. The simulations presented in this thesis were done with the quasi-3d code FBPIC. In FBPIC, the fields are represented via an azimuthal Fourier decomposition [53, 68]. This reduces the computational cost while still modeling important 3d effects. The motion of macro particles in the field grid is calculated and the field generated by the particles is added to the grid. A spectral solver is used to solve the Maxwell equations in Fourier space, which surpresses unphysical behaviour originating from numerical noise [69]. Further, the code allows to describe the particle motion in a co-moving frame with the laser. The reader may find additional material beyond this very brieve introduction in [70, 71, 72].

FBPIC allows to use a realistic flattened-Gaussian profile [73] for the trasnverse laser field distribution, which is close to the ideal laser profile measured in the experiments. However, e.g. wavefront distortions of the laser beam are not included in the simulations. The laser peak intensity can therefore deviate from the laser peak intensity in the experiment. Also the gas density profiles in the simulation are generated from analytical functions or directly read in from fluit-dynamic simulations [66], which may not fully recover the density profiles in the experiment. In addition, experimentally, not all laser properties are measured online and otherwise may include stystematc errors.

Thus, PIC simulations can be used to approximate the electron phase-space to some extend. The simulated electron beam properties, such as the total beam charge, the maximum beam energy or the transverse phase-space of the electrons can quantitively differ from the measured beam properties. Qualitative agreement to the experiment can

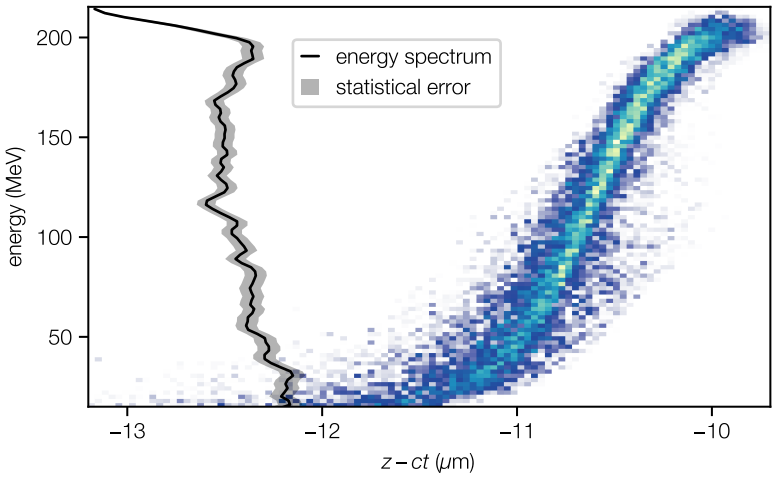

Figure 2.7. – Longitudinal electron phase-space at the end of the plasma. The electron energy positively correlates with the internal bunch position. Electrons are continuously injected and accelerated resulting a continuous energy spectrum (black). FBPIC [53] simulation by courtesy of L. Jeppe.

be achieved by scanning the simulation parameters, e.g. the laser peak intensity and the laser focus position.

FBPIC-simulations with input parameters close to the experiment have been performed by L. Jeppe. The simulated electron density and the longitudinal on-axis field at the end of the plasma to vacuum transition is plotted in figure 2.2 and has been discussed in section 2.1. A histogram of the simulated longitudinal electron phase-space is plotted in figure 2.7. Electrons are continuously injected and accelerated over the full plasma channel length. The electron beam spectrum (black curve) is therefore broadband with a maximum electron energy of 200 MeV[1]. The longitudinal electron phase-space is positively correlated. Electrons with higher energy are located at the head of the beam, electrons with lower energies are located at the tail. The electron energy is mainly increasing linearly with the internal bunch coordinate z. Only a small curvature of the longitudinal phase-space can be seen which originates from beam-loading, thus the electron beam deforming the linear slope of the laser-wakefield. However, no significant peak in the spectrum is observed.

The phase-space plotted in figure 2.7 was simulated with 57 314 macro particles. The electron energies were arbitrarily binned into 100 slices. The finite number of macro particles per energy slice thus results in a relative statistical error of 4 %. The plotted energy spectrum in figure 2.7 has been smoothed in order to surpress numerical noise.

[1]The maximum energy in the raw spectrum from the PIC simulation is 50 % higher and is reduced to match the measured spectrum, see figure 6.1.

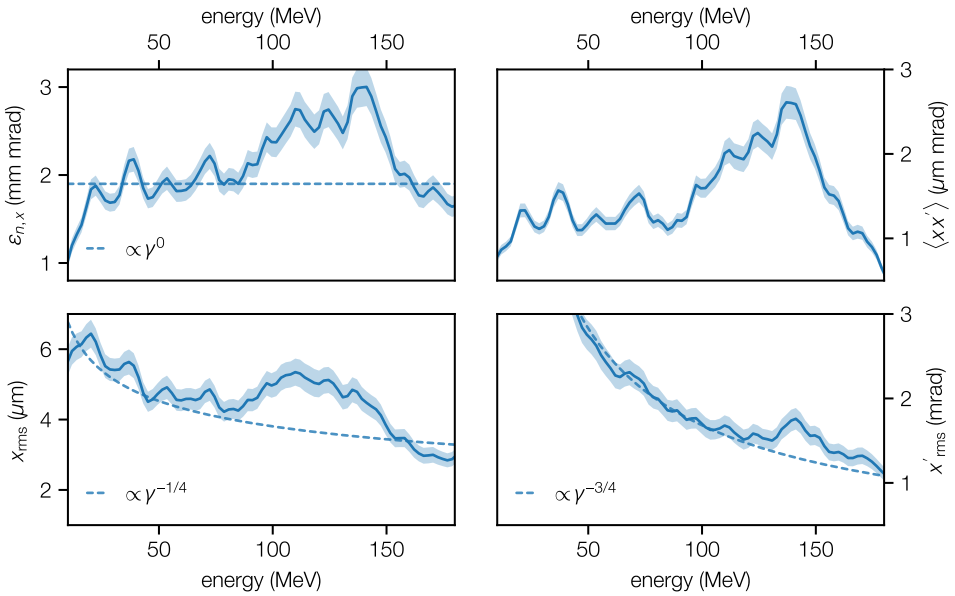

Figure 2.8. – Horizontal phase-space properties of different energy-slices from a PIC simulation (solid lines). The shaded areas denote the statistical error. The dashed lines show the theoretical energy-dependence. The phase-space properties deviate for the head of the bunch with higher beam energy. FBPIC [53] simulation by courtesy of L. Jeppe.

The grey area denotes 1 standard deviation of the statistical error of the simulated energy spectrum.

Additionally, the horizontal phase-space properties for the single energy-slices are calculated. The normalized emittance $\varepsilon_{n,x}$, the rms beam size x_{rms}, rms beam divergence x'_{rms}, and phase-space correlation $\langle x\, x' \rangle$ are plotted in figure 2.8 for each slice-energy. The solid lines and the shaded areas are the simulated phase-space properties and the statistical error from the finite macro particle number, respectively. The theoretical energy dependences derived from the electron motion inside the plasma channel [74] are plotted in dashed lines. The beam size out of the plasma scales with $\gamma^{-1/4}$. The beam divergence out of the plasma scales with $\gamma^{-3/4}$. The normalized emittance therefore is independent of the electron energy (see equations 4.2 and 4.3). For energies below 100 MeV, the energy dependence of the PIC simulated phase-space properties matches the theoretical curves. For energies above 100 MeV the normalized emittance, the phase-space correlation and the beam size after the plasma increase with the energy and are peaked at around 125 MeV. According to the simulated longitudinal phase-space, the higher energies correspond to the head of the bunch. The lower energy phase-space could thus be modulated by the additional wakefield driven by the accelerated electron beam. The head however, forming the wakefield, is not effected by the additional focusing fields. A similar effect as the described is the head-erosion of the driver-beam observed in electron-beam driven plasma-acceleration [75].

According to the simulation, the phase-space properties can thus vary along the beam and the energy spectrum. These energy dependencies have to be considered in an experiment. At the same time, energy-resolved phase-space measurements are required in order to be able to choose the fraction of the spectrum - if possible - that delivers the optimum beam phase-space for the experiment.

The experimental setup, the emittance diagnostics and measurement methods at LUX are described in the following chapters 3 and 4. The results from the emittance measurements are presented in chapter 6. In section 6.6 the energy dependence of the phase-space properties was measured and is discussed. The measurement results qualitively match the simulated phase-space discussed above.

3. LUX Beam Optics and Beam Diagnostics

The LUX electron optics and electron beam diagositcs are introduced in this chapter. The beam optical elements, the quadrupole doublet and the corrector dipoles, are presented in section 3.1. The electron beam diagnostics is summarized in section 3.2. The LUX electron spectrometer is discussed seperately in section 3.3.

3.1. Beam Optics

The LUX beam optics is designed to transport the laser-plasma accelerated electron beams into the undulator or the electron spectrometer. The optics discussed in this section consists of two quadrupole focusing magnets, two pairs of corrector dipoles to steer the electron beam, and the spectrometer dipole. The quadrupole and corrector dipole magnets are located closest to the plasma target in order to manipulate the electron beam and to reduce the beam divergence as early as possible.

The remaining laser pulse after the plasma interaction is outcoupled from the beamline after 1.6 m and diagnosed. Therefore, the beam optics was optimized for a clip free transmission of the remaining laser pulse after the plasma interaction while featuring minimum magnet apertures for maximum magnet field strengths.

3.1.1. Quadrupole Doublet

The focusing optics at LUX consists out of two electro quadrupole magnets forming a compact doublet. Figure 3.1 shows a picture of the installation in the experimental area.

The doublet is build from two DESY XQA [76] electro quadrupole magnets. Each magnet has been modified in order to fulfill the requirements in aperture and field gradient at LUX. The aperture of the first quadrupole magnet Q_1 has been reduced to 12 mm. Each yoke quarter is added by an extra pole tip with the correct hyperbolic curvature that corresponds to the new aperture radius. The second quadurpole magnet Q_2 has first been stretched by additional spacer insets between the yoke quarters and has then been

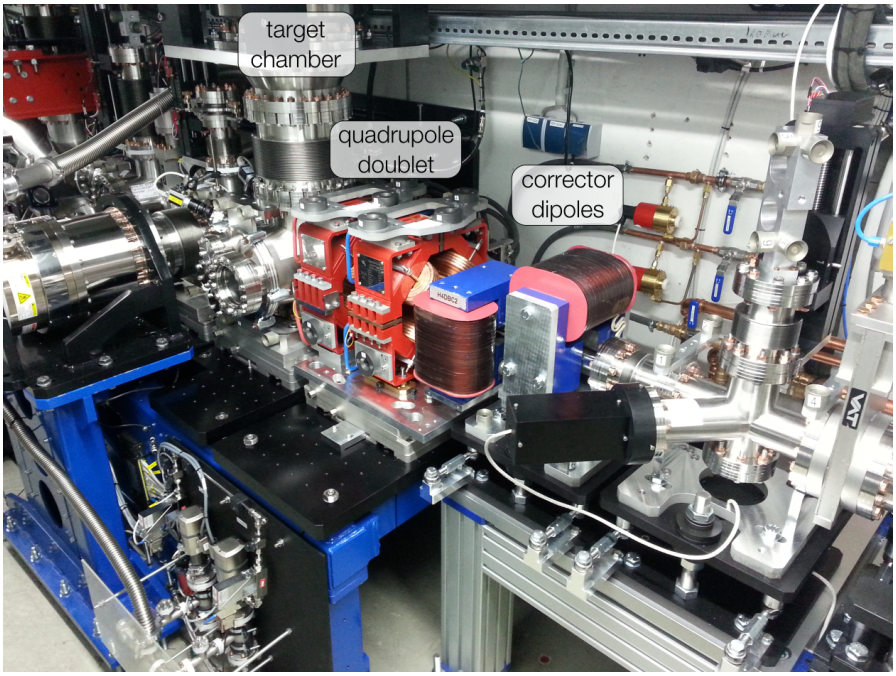

Figure 3.1. – Picture of the LUX target area (left), the quadrupole doublet (red) and the first pair of corrector dipoles (blue).

modified analogously to Q_1. Table 3.1 summarizes the properties of the two quadrupole magnets.

The quadrupole magnet fields were measured with a 1-dimensional Hall probe from *GROUP3* [77] with a relative accuracy of 1×10^{-4}. The measured integrated field gradients per coil current are plotted in figure 3.2. The field gradients are linearly increasing with the coil currents up to 70 A for the first magnet Q_1 and 110 A for the second magnet Q_2. Afterwards, the magnets begin to saturate and the growth in field gradient is less than in the linear regime. The saturation is stronger in the first magnet. Here, increasing the coil current from 100 A to 200 A only results in an increase of 9 % of the field gradient. This behaviour is the limiting factor for the maximum focusable beam energy. However, the resulting field gradients enable to capture beams with energies up to 450 MeV within the first 400 mm behind the plasma target.

The required field gradient profiles along the doublet to focus electron beams of different beam energies are plotted in figure 3.3. The resulting beam envelope along the doublet of mono-energetic beams with 1 mrad divergence from a source 100 mm in front of the first quadrupole magnet are added to the figure. The required field gradients scale linearly with the beam energy. The beam envelopes of the focused electron beams coincide. Due to the nature of quadrupole magnets similarly focusing and defocusing the beam in the two transverse planes, the focused electron beam is asymetrically large after the doublet.

Table 3.1. – Table of quadrupole magnet properties.

property	value
yoke length	100 mm
drift between magnets	100 mm
design distance to target	110 mm
Q_1 apperture	12 mm
Q_1 peak gradient	150 T/m
Q_2 apperture	22 mm
Q_2 peak gradient	70 T/m

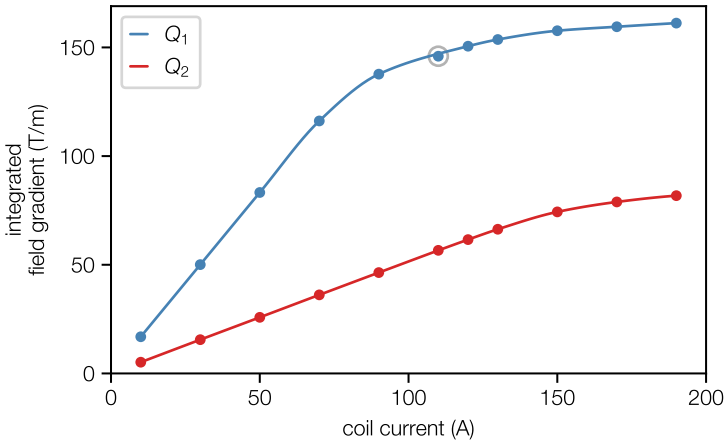

Figure 3.2. – Integrated quadrupole field gradients versus applied coil current. The data points are interpolated by a cubic spline (lines). The data point marked in grey is excluded from the spline fit.

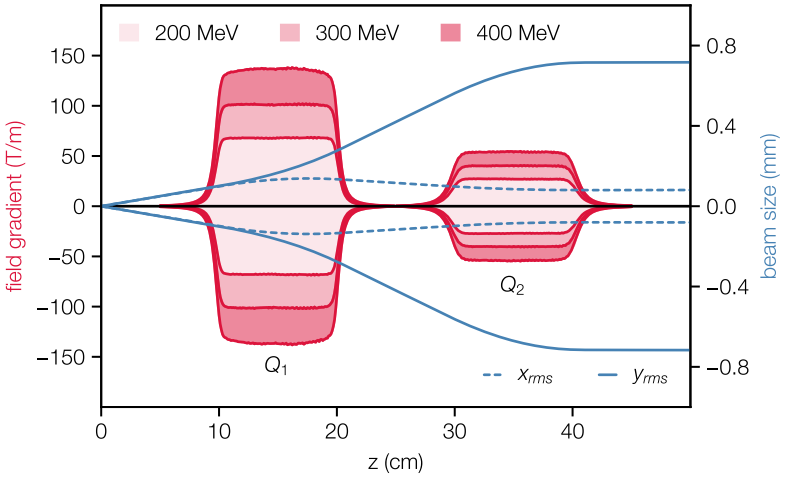

Figure 3.3. – Field gradient profiles of the quadrupole doublet for focusing of different beam energies. The evolution of the beam envelope in x and y is shown in black.

The focused beamsize directly after the doublet is mainly determined by the initial beam divergence. In the example of a 1 mrad divergent beam, the vertical rms-beam size behind the doublet is 720 µm and only 90 µm in the horizontal. This ratio is rather constant due to the geometry of the setup, but the axes can easily be flipped by changing the polarity of the doublet currents.

The transverse field of a quadrupole magnet can deviate from the linear field gradient. The field can in general be expressed in terms of higher order multipoles.

$$B(r,\theta) = \sum_{n=1} C_n e^{-i\alpha_n} (re^{i\vartheta})^{n-1}, \tag{3.1}$$

where C_n is the amplitude and α_n the phase of the nth multipole, r is the radial distance from the magnetic axis and ϑ the azimuthal angle. The strength of the nth multipole increases with r^{n-1} and the radial and azimuthal multipole components oscillate with a $2\pi/n$ periodicity.

In order to also quantify the field quality the quadrupole magnets have been measured using rotating coils [78]. The magnetic field inside the coil area changes with the rotation angle which induces a voltage. Since the influence of higher order field components vanishes in the center of the magnet, rotating coils are in favour for the measurement of the field quaility, because a rotating coil measures the azimuthal field component over almost the full aperture radius and integrated over the full magnet length. A Fourier analysis of the evolution of the azimuthal field component per rotation angle then yields the field amplitude and phase of each multipole field component. However, the resolution of rotating coil measurements is limited by mechanical imperfections and a relative precision of less than a few percent can not be expected.

The field quality measurements in figure 3.4 were done with two double coils which were specifically built for this measurement. Each double coil consists of two coplanar coils with different coil diameters and winding numbers. The diameters and winding numbers were chosen such that the same voltage is induced for the quadrupole field component. Hence, electronic subtraction of the single coil signals cancels out the induced voltage by the quadrupole component and a direct measurement of the higher order multipoles is available. Due to mechanical imperfections the signal of the quadrupole component of Q_1 could not be erased completly, which can be seen from the π-periodicity of the signal in subfigure 3.4a.

For the second magnet Q_2 (subfigure c) no signal with a two period oscillation during one coil rotation is observed, which indicates the absence of a quadrupole field in the differential measurement. The multipole amplitudes decrease for higher order n for both magnets. However, the relative sextupole ($n = 3$) and octupole ($n = 4$) component are above 1×10^{-3}, which indicates a misalignment bewteen the extra pole tips. Nonetheless, since the magnets' centers are located 150 mm and 350 mm behind the target, the electron

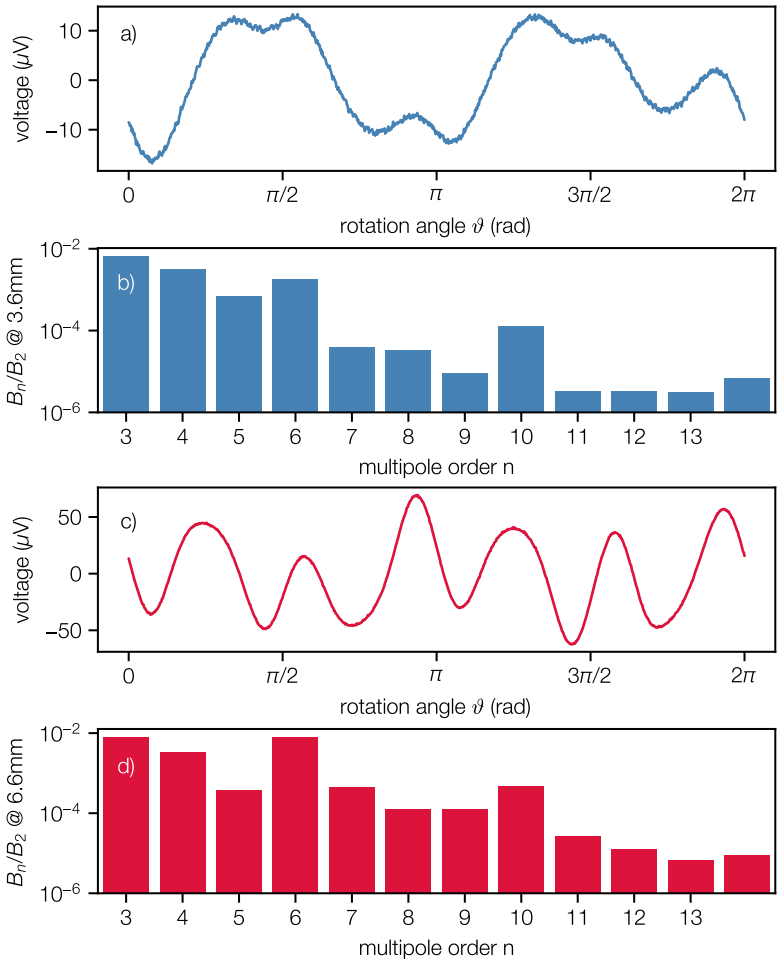

Figure 3.4. – Rotating coil measurements of the LUX quadrupole Q_1 (a) and Q_2 (c). Subplots (b) and (d) show the relative multipole field amplitudes obtained from a Fourier analysis.

Table 3.2. – List of corrector dipole properties.

corrector	C_1	C_2	C_3	C_4
type	TCA40	TCA50	TCA40	TCA40
position (mm)	558	742	2112	2311
yoke length (mm)	100	100	100	100
aperture (mm)	40	50	40	40
field at 3 A (mT)	150.2	129.4	150.5	150.0
effective length (mm)	163	173	163	163
orientation	hor	vert	hor	vert

beams diverging from the target are still small and thus only see a small fraction of the field non-linearity. The emittance growth introduced by this field non-linearity has been estimated to be on the order of 0.1 mm mrad and is thus below the detection limit.

3.1.2. Corrector Dipoles

Two pairs of corrector dipole magnets are installed in the LUX beamline. The first pair of horizontally and vertically deflecting dipoles is located directly 100 mm behind the quadrupole doublet. The second pair is located another 2 m downstream the beamline, respectively 0.5 m behind the laser outcoupling mirror. The dipole apertures are varying between 40 mm and 50 mm due to the laser size at the respective position before outcoupling. Table 3.2 summarizes the corrector dipole properties.

The corrector dipoles enable to correct for a spatial and angular offset of 5 mm and 5 mrad of the beam behind the target or the quadrupole doublet, respectively. However, due to the magnets large gap sizes and therefore large extent fringe fields, the magnetic field of the first corrector pair can leak into the second quadrupole Q_2. Further, the corrector dipoles disperse the electron beam before the electron spectrometer. The negative effects of dispersion before the spectrometer dipole are discussed in chapter 4.3.4. As a consequence, the corrector dipoles were not used for the emittance measurements in chapter 6. However, the corrector dipoles were used for the beam-based alignement of the quadrupole magnets in chapter 5.

3.2. Beam Diagnostics

The LUX beamline features three different types of electron beam diagnostics. The total charge and center of charge are detected by two non-invasive beam position monitors (BPM, subsection 3.2.1). In addition, scintillator screen stations (subsection 3.2.2) enable to measure the transverse beam profile at two different positions in the beamline. The

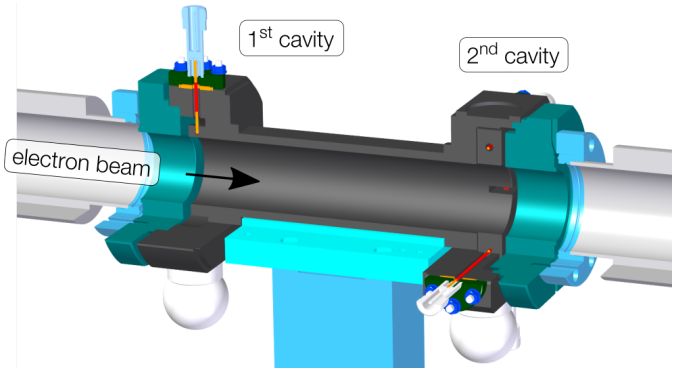

Figure 3.5. – Cross section of a cavity BPM. Two resonators at the entrance and exit pick up the electro-magntic field modes of the incomming electron beam. Figure taken from C. Werle [67].

third diagnostics is the electron spectrometer, which is discussed in a seperate section (3.3), due to its importance for the emittance measurements in chapter 6.

3.2.1. Beam Position Monitors

Two cavity beam position monitors (BPM) [79, 80] are installed in the LUX beamline. The BPM comissioning was mainly done by C. Werle with the help of B. Hubert. Each BPM consists out of two cavities. Each cavity functions as a pick up resonator of a magneto-optical mode at a resonant frequency of 3.3 GHz from the beams electro-magnetical field. Cross talk between the two cavities is by design suppressed [81, 82].

The first cavity picks up the TM01 mode, which linearly scales with the total beam charge. The second cavity picks up the horizontal and vertical TM11 mode which linearly scale with the product of the total beam charge and mean beam position. Combining the two information enables a non-invasive center of charge detection on a single shot basis. A cross section of a cavity BPM is shown in figure 3.5. The two cavity BPM at LUX are chosen to define the electron design axis. The elctron beam is defined to be on axis in case of the BPMs reading a center position of 0.

However, by design, the BPM signals are not sensitive to the beam energy, respectively the beam energy spectrum. This can lead to a distortion of the position measurement of the core part of the beam when the beam is dispersed by the previous beam optics. Accordingly, the BPM readings may be carefully interpreted with focused electron beams.

Table 3.3. – List of profile screen properties.

parameter	screen station 1	screen station 2
postion (mm)	3114	7644
scintillator material	LYSO:Ce	YAG:Ce
scintillator size (mm x mm)	24 x 32	30 x 30
scintillator thickness (µm)	400	500
camera	BASLER avA2300-25gm	
objective	Schneider MAKRO/SYMMAR 5.9/120	

3.2.2. Beam Profile Screens

Behind each BPM a beam profile screen is installed. Both screen stations and their optical system were designed by DESY, MDI [83]. Only the vacuum chambers and the scintillator screens were adapted to the LUX requirements. Both profile screens are mounted to a manipulator in order to be driven in and out of the beamline. The first screen is a LYSO:Ce scintillator crystal [84]. The screen built into the second screen station is a YAG:Ce scintillator [85]. The screens are orientated orthonagally to the electron beam. The optical system is built in a Scheimpflug configuration, which realizes the focal plane to be tilted onto the screen plane, though the objective and camera are mounted under 45° to the electron beam axis.

Special care was taken on the laser light shielding. The remaining on-axis laser pulse energy after the outcoupling section can still be on the hundrets of mJ level. These background photons would overshine the scintillator light by far. Further, refocusing of the remaining laser pulses by the vacuum pipe can result a laser focus on the scintillator which would cause generation of white light and would damage the scintillator. Therefore, the scintillator crystal is shielded by a 100 µm thick stainless steel foil on the laser side. Additionally, an inset pipe is mounted into the chamber entrace to block the light leakage into the chamber.

3.3. Electron Spectrometer

The LUX electron spectrometer was designed by C. Werle [67]. Figure 3.6 shows a CAD rendering of the full assembly.

The electron spectrometer was designed to simultaneously detect a maximum broad energy range from 40 MeV to 2.5 GeV. In particular, the full range is continuously recordable without any clipping of the electron beam along the dispersive axis. The electron beams are deflected by a 40 cm long permanent dipole. The spectrometer is therefore located at the very end of the LUX electron beamline. The dipole magnet is

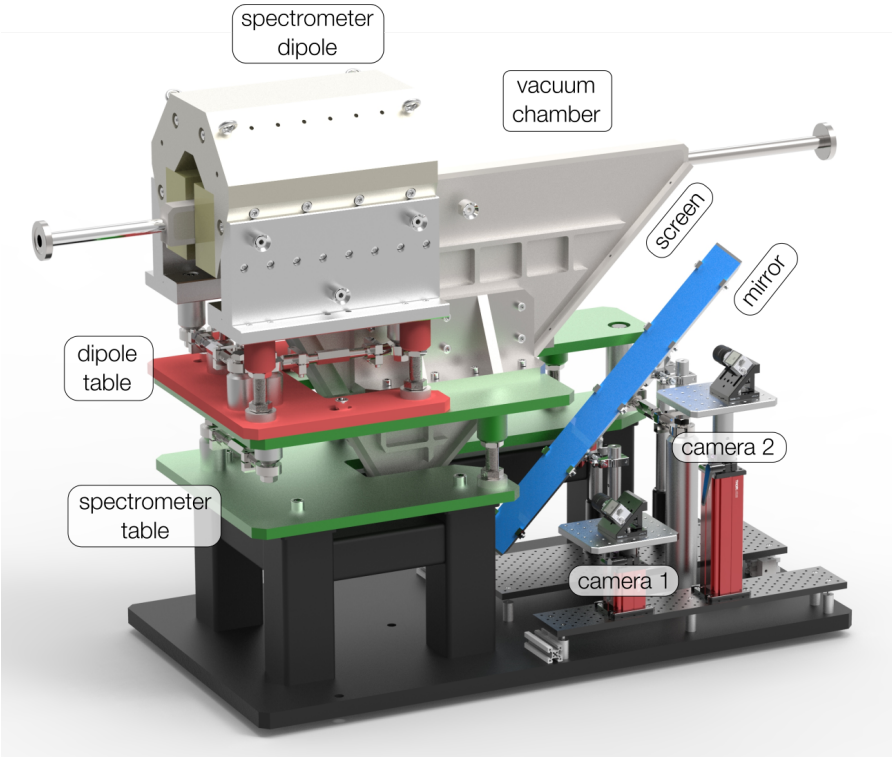

Figure 3.6. – Picture of the LUX electron spectromter. Figure taken from C. Werle [67]. The triangular vacuum chamber and the dipole magnet (top-left) are mounted to individual adjustment tables (green and red). The scintillator light is detected by two cameras over a mirror (blue).

Table 3.4. – List of electron spectrometer dipole properties.

property	value
integrated field (along z) (T m)	0.386
peak field (T)	0.962
gap width (mm)	40
gap height (mm)	150
gap length (mm)	400
number of poles	48
pole material	VACODYM 764 TP
pole size (mm^3)	50 x 50 x 65

Table 3.5. – Expansion of the measured spectrometer dipole 3D fieldmap grid.

axis	lower limit	upper limit	step size	grid points
x	−6 mm	6 mm	3 mm	5
y	−220 mm	60 mm	5 mm	57
z	−330 mm	330 mm	5 mm	133

mounted on a seperate alignment table, such that both the chamber and the magnet can be aligned individually to the tunnel coordinate system. The electron beams are vertically deflected by the dipole magnet onto an 80 cm long scintillator screen. The scintillator light is reflected by a mirror and detected with two CCD cameras.

3.3.1. Spectrometer Dipole

The spectrometer dipole is an assembly of in total 48 permanent magnets. 12 magnets each are attatched to four structural identical C-shape iron yokes that guide the magnetic flux outside the dipole gap. The design of the magnetic structure was originally done by the *Hemholtz-Zentrum Dresden-Rossendorf* [86]. The four yokes have a total length of 0.4 m with a peak field of 0.962 T. The magnet properties are listed in table 3.4.

The specrometer dipole field was measured with a 3-axis Hall probe on a 3-dimensional grid. The detector was a *SENIS Integrated 3-Axis Hall Probe C-H3A-xx* [87] with a relative precision of 1×10^{-3}. The dimensions of the 3D fieldmap grid are listed in table 3.5. It was ensured that the magnets fringe fields at the entrance and the two exit sides were included. The fieldmap contains 37 905 data points for each field component and was taken on two consecutive days.

For the field measurements, the spectrometer dipole was mounted on its alignment table and was leveled with a water level. Due to the dipole being built out of many single permanent magnets, whose magnetization can differ in strength and direction, the field

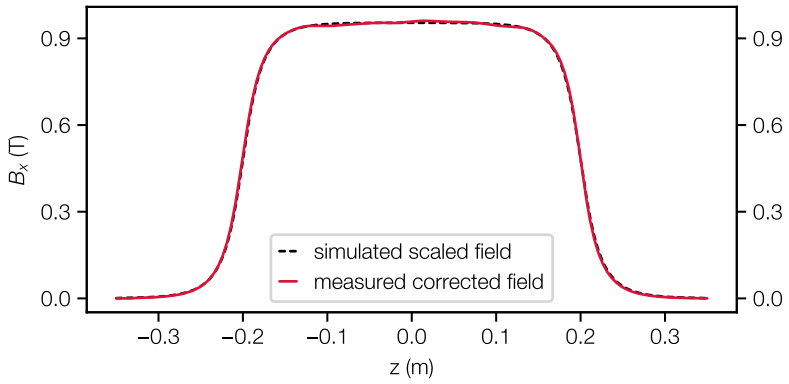

Figure 3.7. – Spectrometer dipole field lineouts along the coordinate axes. The simulated and measured fields coincide. All three field components vary along the dipole and thus focus and defocus the electron beams.

inside the gap varies within a range of 1 %. Hence, the Hall probe was not aligned to the magnetic field, but was adjusted with a leveling device by eye. The 3-axis mover of the Hall probe was adjusted relative to the dipole gap.

However, neither a small misalignment nor a rotation between the Hall probe, the mover and the dipole coordinate frame during the field measurement can be excluded. A comparison of the measured fieldmap with an ideal field by L. Hübner [88] enabled to afterwards determine the misalignments and to account for them. Here, the fieldmap was iteratively rotated and shifted until the field in the symmetry plane of the magnet (the y-z-plane) was maximized for the main field component and minimized for the other field components. The result was a shift of the mover axis of 1.4 mm relative to the dipole axis and a rotation of the Hall probe of 40.3 mrad and of the dipole of 6.8 mrad relative to the mover frame. The measured field map was corrected for these deviations accordingly.

In a next step, a FEM simulation of the spectrometer dipole was done using *Computer-Simulation-Technology* (*CST*) [89]. Since the permeability of the spectrometer dipole was not measured and not stated by the manufacturer, the *CST* fieldmap was scaled such that the field integral matches the field integral of the corrected measured fieldmap.

The fields main compenent B_x along the dipole's central axes is plotted in figure 3.7. The scaled *CST* fieldmap and the corrected measured fieldmap are in good agreement. The field of the simulated and measured fieldmap coincide and have the same shape and field extent. Due to the rather large dipole gap of 4 cm, the fringe field in the longitudinal direction extents from 6 cm inside to 6 cm outside the magnet. The effect is even stronger in the vertical axis. Here, the fringe field extents the gap by 8 cm. Since the dipole gap height is only 15 cm, this results in the field not being flat at any position. Hence, the

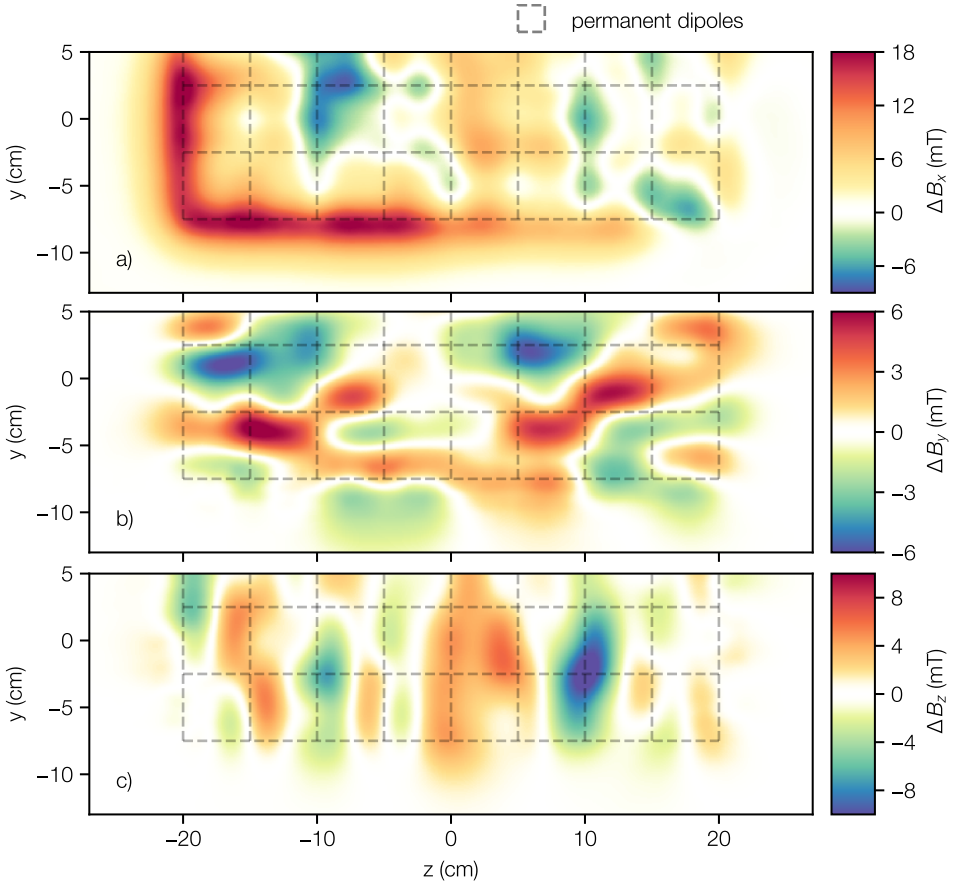

Figure 3.8. – Difference between the corrected measured fieldmap and the ideal simulated and scaled field map. The deviation can be explained by the different amplitude and orientation of magnetization of the single permanent dipoles that built the magnet. Figure adapted from L. Hübner [88].

electrons experience a vertically focusing and a horizontally defocusing force along the full magnet length.

The deviation between both field maps in the symmetry plane is plotted in figure 3.8. The deviation originates from the varying strength and direction in magnetization of the 48 single poles. Particle tracking simulations through both fieldmaps did only show differences in particle trajectories which are below the spectrometer screen resolution.

Accordingly, the *CST* simulated field map was used for the later analysis, since it can be computed on a bigger and much denser grid.

3.3.2. Spectrometer Calibration

The spectrometer screen is a 80 cm long KODAC LANEX OG 16 [90]. It is directly taped to the electron spectrometer chamber. On a 16 mm wide area, the spectrometer chamber wall is reduced to only 1 mm thickness, in order to keep the influence on the electron beam by the material at a minimum. Due to the usable screen width being limited to 16 mm, charge can be lost in the non-dispersive axis of the spectrometer. The screen is rotated by 45° to the initial electron axis. Two cameras are detecting the scintillator light. The scintillator light is deflected by 90° by a mirror in order to mount the cameras out of the electron deflection plane of the dipole magnet to reduce radiation damage. The electron energy can be measured from the signal position on screen, which has to be properly referenced to the camera pixel coordinates. The camera pixel to electron energy calibration was done in three steps.

Lens Distortion Correction

Each of the two cameras is imaging a length of 37.7 cm of the screen in the dispersive axis. The distance of the cameras to the screen is 40 cm and thus a large full angle of 50° is covered by the camera objectives. The therefore stronger curvature of the objective lenses leads to a "fish-eye"-like, or a "barrel" distortion of the images [91, 92].

Figures 3.9a and 3.9b show the raw images of a printed checkered board, that was installed in front of the scintillator screen wall. Note that the plotted aspect ratios are chosen far from 1 to improve the visibility of the curvature introduced by the imaging camera optic. Sources at the border of the field of view are imaged too close to the camera chip center. This results in a change in imaged screen width by up to 10 % difference between the center and the outer edges of the field of view.

The checkered board consists out of white and black squares with a width and height of 2 mm. The corners of the black and white squares on the board are detected in the images with a peak detection algorithm. A common lens distortion correction algorithm [92] is used to unsqueeze the images. The polynomials used in this thesis are

$$\begin{aligned}
\tilde{x}_c &= \tilde{x}\left(1+\sum\nolimits_{i=1}^{4} k_i R^{2i}\right) + \left(2p_1\tilde{x}\tilde{y} + p_2\left(R^2+2\tilde{x}^2\right)\right)\left(1+p_3R^2\right), \\
\tilde{y}_c &= \tilde{y}\left(1+\sum\nolimits_{i=1}^{4} k_i R^{2i}\right) + \left(2p_2\tilde{x}\tilde{y} + p_1\left(R^2+2\tilde{y}^2\right)\right)\left(1+p_3R^2\right), \\
R &= \sqrt{\tilde{x}^2+\tilde{y}^2},
\end{aligned}$$

where $\tilde{x}$ and $\tilde{y}$ are the pixel coordinates in the raw images in the horizontal and vertical direction, which are given relative to the distortion origin close to the chip center pixel. The k_i denote the radial distortion coefficients and p_i the tangential.

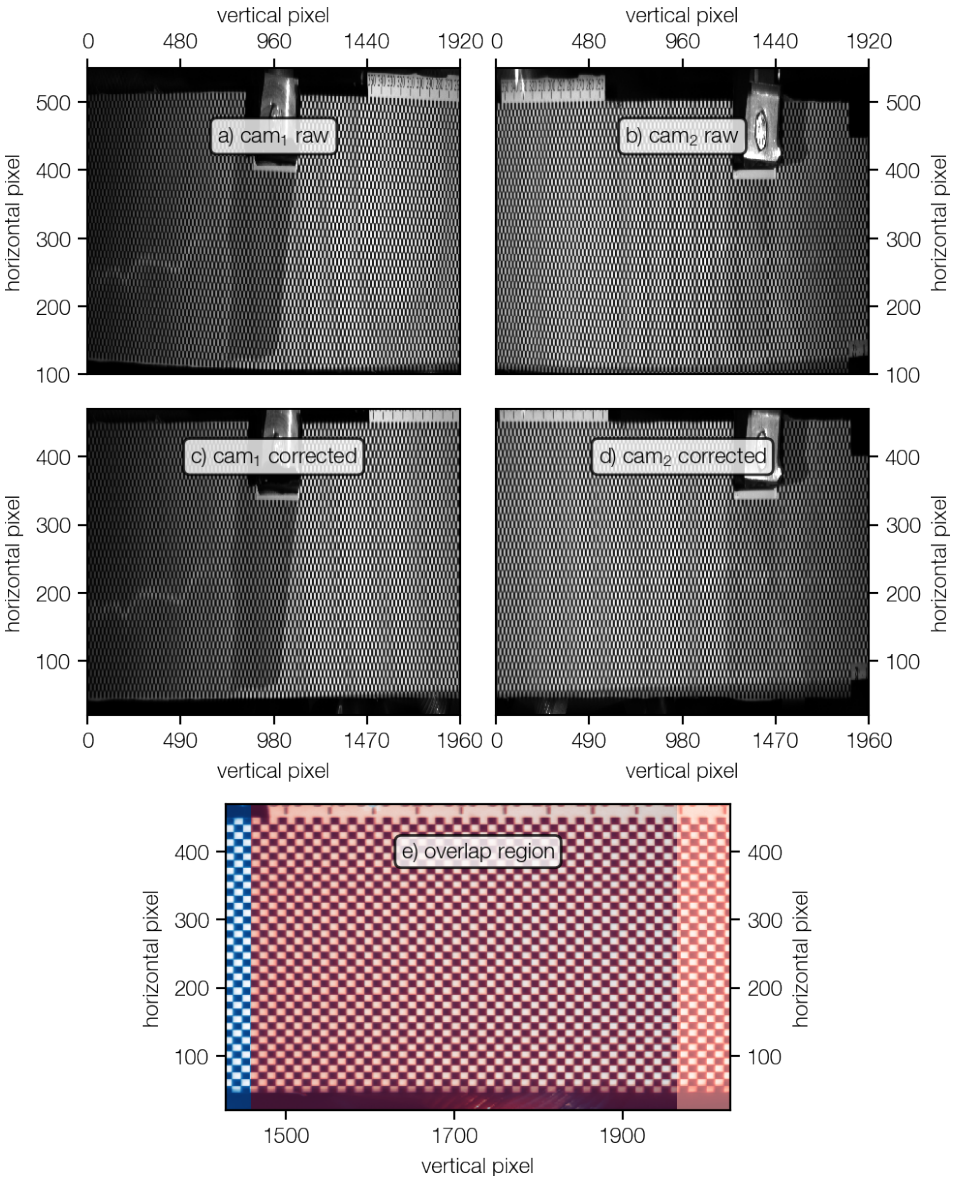

Figure 3.9. – Image lens distortion correction. Figures a) and b) show the raw spectrometer camera images of a checkered board in front of the spectrometer screen. Figures c) and d) show the distortion corrected images. After correction, the images of cam 1 (blue) and cam 2 (red) show the same pattern in the overlap region (e).

After the distortion correction a global rotation of the image by an angle θ_{rot} is applied to the corrected coordinates $\tilde{x}$ and $\tilde{y}$ to account for a rotation of the camera arround the screen normal.

Finally, a global scaling factor c_z is multiplied to the coordinates to stretch or squeeze the image linearly, in order to adjust for small differences of the camera distances to the sreen. The equations above are minimized to undistort the pixel coordinates such that the found edge positions in the 2 mm checkered board have equal spacing across the images. Additionally, the deviation in the overlap region of the cameras was minimized for both cameras simultaneously. The image correction coefficients for both cameras are listed in appendix B.1.

The undistorted checkered board images are depicted in figures 3.9c and 3.9d. A superposition of both undistorted camera images in the overlap region is plotted in figure 3.9e. After correction, the images are interpolated back to a linearly spaced regular grid, i.e. to allow for a projection of the image along the tunnel axis.

Intensity Distortion. Another distortion by the lens objectives is the reduction in detected signal intensity towards the edges of the field of view. The *LANEX* screen is a Lambertian-like radiator with an angular dependent drop in emitted photon-flux away from the normal incidence axis, approximated by a cosine-dependence [90]. In addition, the total opening angle of the radiation that is collected by the camera objective narrows with the incident angle into the objective. The signal intensity in the outer regions of the field-of-view is further attenuated by vignetting inside the objectives.

A LED foil is used to determine the cumulative drop in intensity in dependence of the angle of incidence into the objective, respectively in dependence of the source position in the screen plane. The LED foil [93] is 138 mm × 34 mm large and translated along the screen wall in order to cover the full dispersive axis of the spectrometer (see figure 3.10b). Images of the LED foil at five different positions were taken with each camera. The recorded signals were projected onto the dispersive axis. Though the signal from the LED is inhomogeneously intense along the foil, the realtive attenuation of the signal along the dispersive axis can still be determined by the comparison of the signal at the differnet LED foil positions. The product of a 3^{rd}-order polynomial and an arbitrary cosine of 4^{th} power, $\cos((x-x_0)/w)^4$, is minimzed simultaneously for all 5 projected LED signals. x_0 and w denote the center and width of the cosine function. The measured projected signals and the polynomial fits as well as the fitted cosine of 4^{th} power is plotted in figure 3.10c. The detected signal from the scintillator plane reduces to 60 % towards the edges compared to the center of the field-of-view.

This calibration is used to correct the recorded signals in the later data analysis. However, it must be mentioned that this calibration is limited in accuracy and only denotes a first order correction. The power of 4 of the cosine is predicted by theory for ideal scintillators and objectives [94]. The real intensity variation can show a stronger dependence on the

solid angle. The fit quality however is not accurate enough to distinguish between higher exponentials or a larger width w of the cosine. Further, the signal dependence from the position on screen should be a radial function, but is only corrected in the dispersive axis of the spectrometer. This is an acceptable compromise since the measurement of the rms-beam size on screen for the emittance calculation (as described in section 4.2.2) in the non-dispersive axis only depends on the shape of the signal and is thus independent of the total signal intensity.

Pixel-to-mm Calibration

A mm-scale is taped next to the scintillator screen. A peak detection algorithm is used to find the single mm-scale lines in the camera images (see figure 3.11a). The ruler mm-scale can be referenced to the tunnel coordinate system by the chamber wall geometry. The found mm-scales in the camera images were background corrected and interpolated by a cubic spline in order to allow for sub-pixel precision. Due to the lens distortion correction, the vertical pixel-to-mm calibration is almost a flat curve. Figure 3.11b shows the deviation of the pixel-to-mm calibration from a linear fit for both cameras. The fast fluctuations originate from the limited peak detection accuracy. The slow variations are remaining lens distortions. The mean area on screen that is imaged by a single pixel is 193 µm. The deviation from a linear calibration is thus within ±1 pixel accuracy.
The imaging objectives of the cameras is rotationally symmetric and the pixel size and spacing on chip is equal in both planes. Therefore, the slope of the mm-to-pixel calibration can also be applied in the other screen axis.

mm-to-MeV Calibration

The calibration between screen-mm and electron energy was done with particle tracking simulations using ASTRA [95]. Single on-axis electrons with energies reaching from 25 MeV to 3 GeV were tracked through the simulated and scaled 3D dipole fieldmap. The electron energies were equally spaced by 0.1 MeV.

Figure 3.12 shows the trajectories of beams with example energies through the spectrometer. The electrons can exit the dipole on the bottom and rear side. Energies arround 300 MeV exit the dipole at the bottom-rear-edge.

Combining all steps above results the pixel-to-energy calibration curve plotted in figure 3.13. The field of view of the two cameras overlaps by 500 pixel and the individual calibration curves show a smooth transition. The relative energy resolution per pixel is plotted below. The relative width of a single pixel in the dispersive axis is below 0.1 %. Only for energies above 400 MeV the relative energy resolution increases to 0.2 %. Note that this is only the resolution limit introduced by the finite pixel size. The pixel

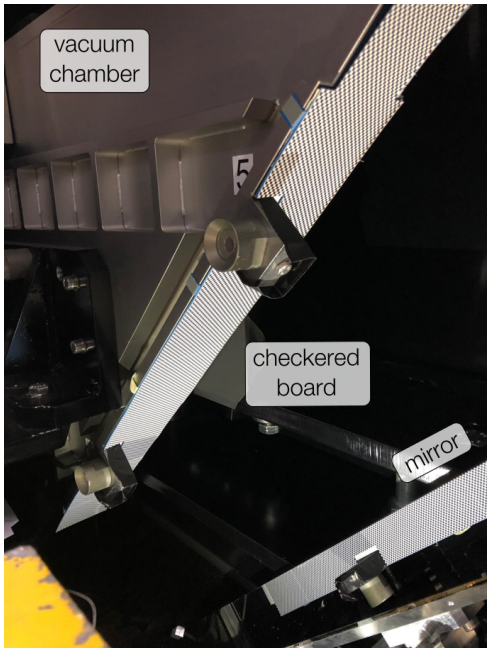

(a) Picture of the 2 mm-checkerd-board taped to the spectrometer chamber wall.

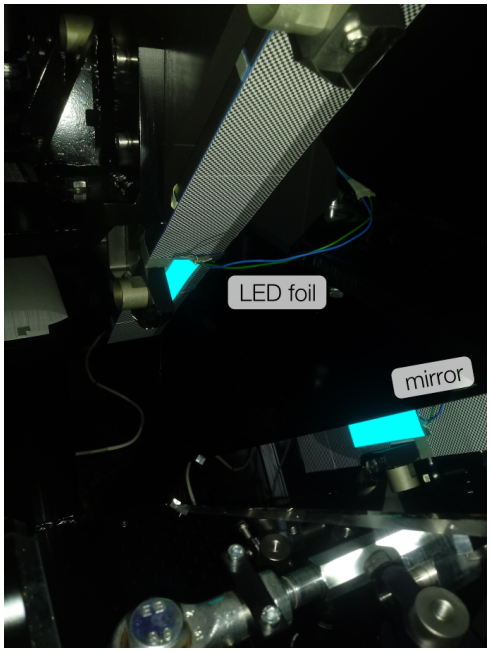

(b) Picture of the LED foil in front of the checkered board.

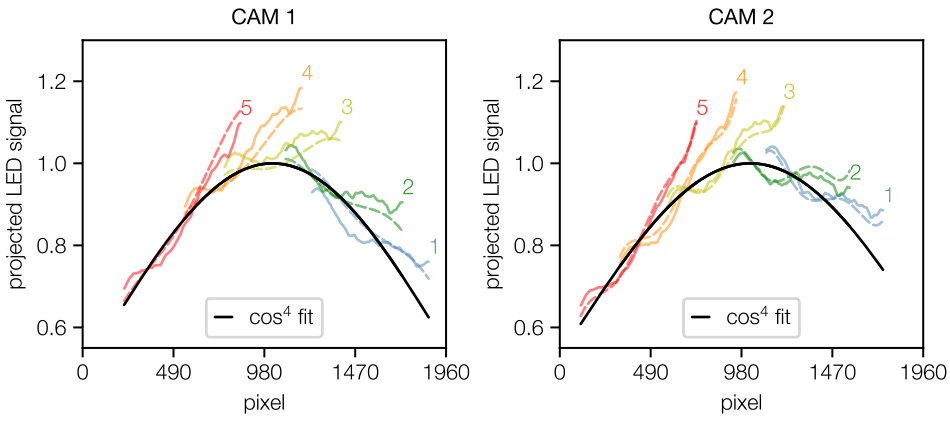

(c) Simultaneous fit of the inhomogeneous projected LED foil signals at different positions 1 to 5 and a cosine of 4th power fit for both spectrometer cameras.

Figure 3.10. – Spectrometer Camera Signal Calibration.

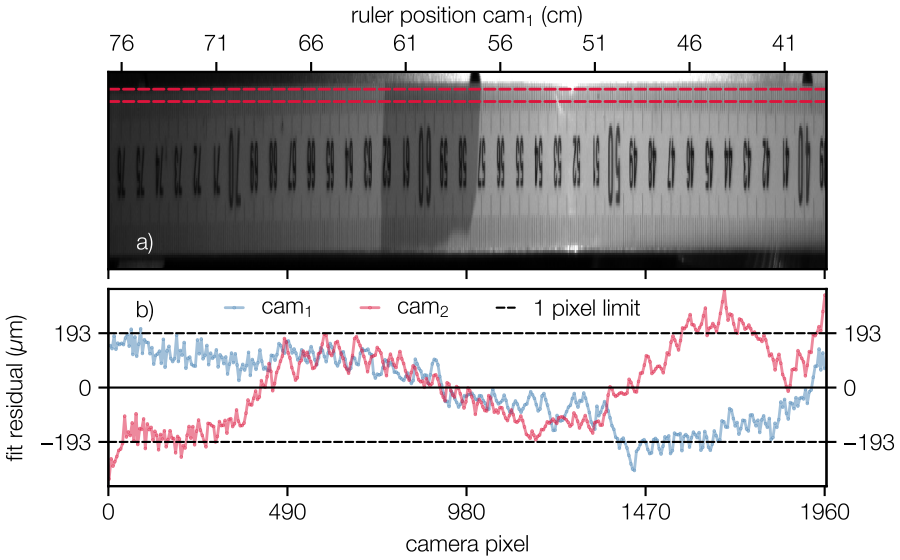

Figure 3.11. – Spectrometer screen pixel calibration. a) Camera 1 image of the spectrometer ruler. b) Linear fit residual to the found mm-scale positions.

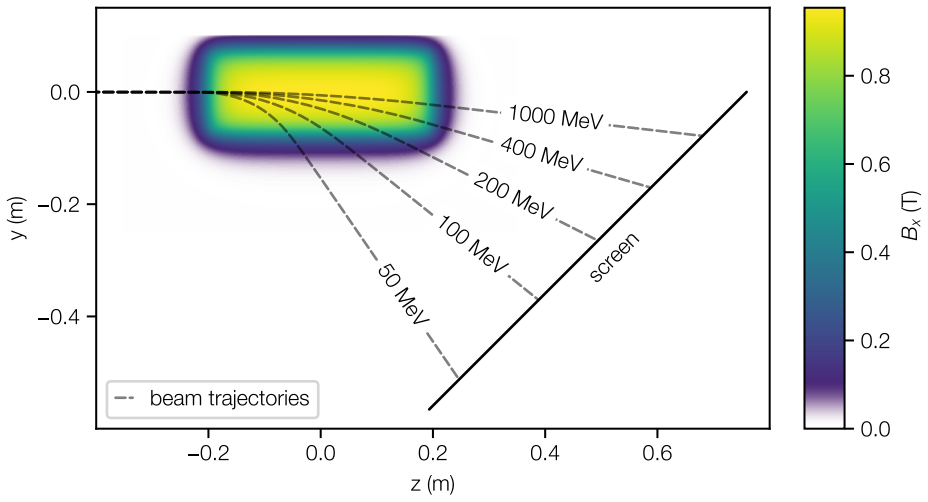

Figure 3.12. – Trajectories of example electron energies through the spectrometer geometry. The electrons can exit the dipole at the bottom and rear side.

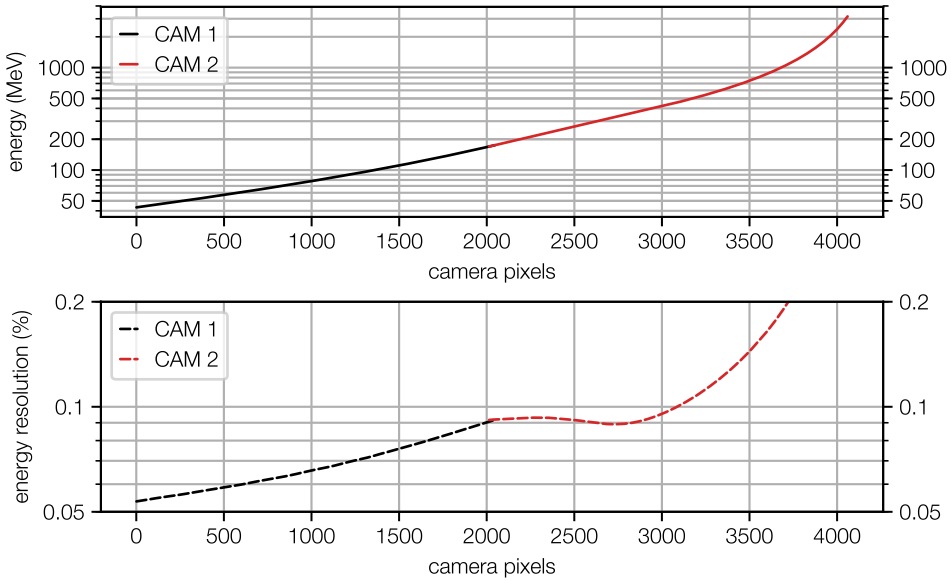

Figure 3.13. – Camera pixel to beam energy calibration and relative energy per pixel resolution.

resolution was designed to match the granularity of the scintillator screen. However, there are other effects that also influence the resolution in the energy measurement. See chapter 4.

As described in section 3.3.1, the field inside the magnet varies in all axis. Therefore, horizontal and vertical field gradients act on the incoming electron beams depending on the electrons position and angle into the spectrometer. The single electron beam path through the dipole and the drift space to the spectrometer screen are complex functions of the beam energy. In particular, the total path length to the spectrometer screen s is a function of the beam energy,

$$s = s(E). \tag{3.2}$$

In order to model the electron beam dynamic correctly, additional electrons with spatial and angular offsets into the spectrometer were simulated for each simulated energy. The electrons with transverse offsets in x and y from $-5\,\text{mm}$ to $5\,\text{mm}$ in steps of $0.5\,\text{mm}$ and angles x' and y' of $-2.5\,\text{mrad}$ to $2.5\,\text{mrad}$ in steps of $0.5\,\text{mrad}$ were simulated from $8\,\text{m}$ behind the target up to the spectrometer screen. These 4-dimensional phase-space grids with in total 53 361 electrons were simulated for every $1\,\text{MeV}$-step of the energy calibration.

This data was used to compute a transfer map, that directly translates an incoming electron beam phase-space into the dispersed electron distribution on the spectromter screen, including all focusing and path length effects of the spectrometer dipole. The

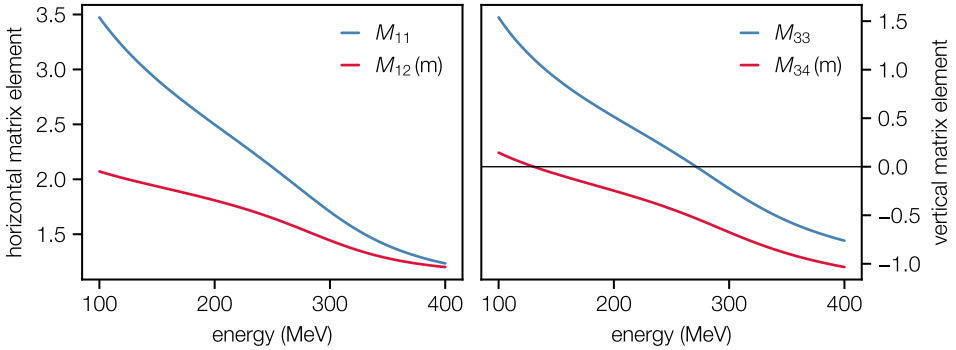

Figure 3.14. – Matrix elements of the spectrometer transfer map. The spectrometer dipole is focusing in the vertical and defocusing in the horizontal plane.

first order coefficients of the transfer map make up the spectrometer transfer matrix. In contrast to common linear beam dynamics the energy dependence of the electron motion in the beam optics at LUX is not described by means of matrix elements from a 6d-matrix, but computed for each individual beam energy in order to model the energy dependence as precise as possible, effectively to all orders in energy.

The matrix elements determining the electron beam size on screen are plotted in figure 3.14. The matrix elements M_{11} and M_{12} of the horizontal plane are plotted in dependence of the beam energy. Both matrix elements are greater than 1 and the spectrometer is thus defocusing the beam in the horizontal axis. The right plot shows the matrix elements in the vertical plane. Here, the M_{33} reduces to 0 at a beam energy of 270 MeV. This corresponds to a minimum in beam size and the spectrometer dipole thus imaging the incoming electron beam (at 8 m) at this energy.

The second order coefficients obtained from the ASTRA simluation are plotted in figure 3.15. The second order coefficients are labeled according to common tensor algebra. Only elements describing the transverse coordinates are considered. The elements T_{ijk} of the $4 \times 4 \times 4$-dimensional tensor T denote the influence on the i-th coordinate by the product of the j-th and k-th coordinate, with $i, j, k \in \{1, 2, 3, 4\}$, respectively $\in \{x, x', y, y'\}$. E.g. the element T_{123} expresses the influence of the product $(x'\, y)$ before the spectrometer dipole onto the x-position on the spectrometer screen. The tensor elements being 0 for all energies are not plotted in figure 3.15. The units of the second order coefficients are plotted in the figure legends. The units are chosen to describe the influence of the input product in mm and mrad onto the respective coordinate on screen in µm or µrad. The maximum beam offset before the dipole is given by the entrance pipe diameter of 22.5 mm and the recordable screen width of 16 mm. The maximum possible angle into the spectrometer is thus limited to 1.3 mrad. In case of unfocused beams directly diverging into the spectrometer, this can introduce a deviation from the first order trajectory by a few hundret µm. Only considering electron beams with a BPM2

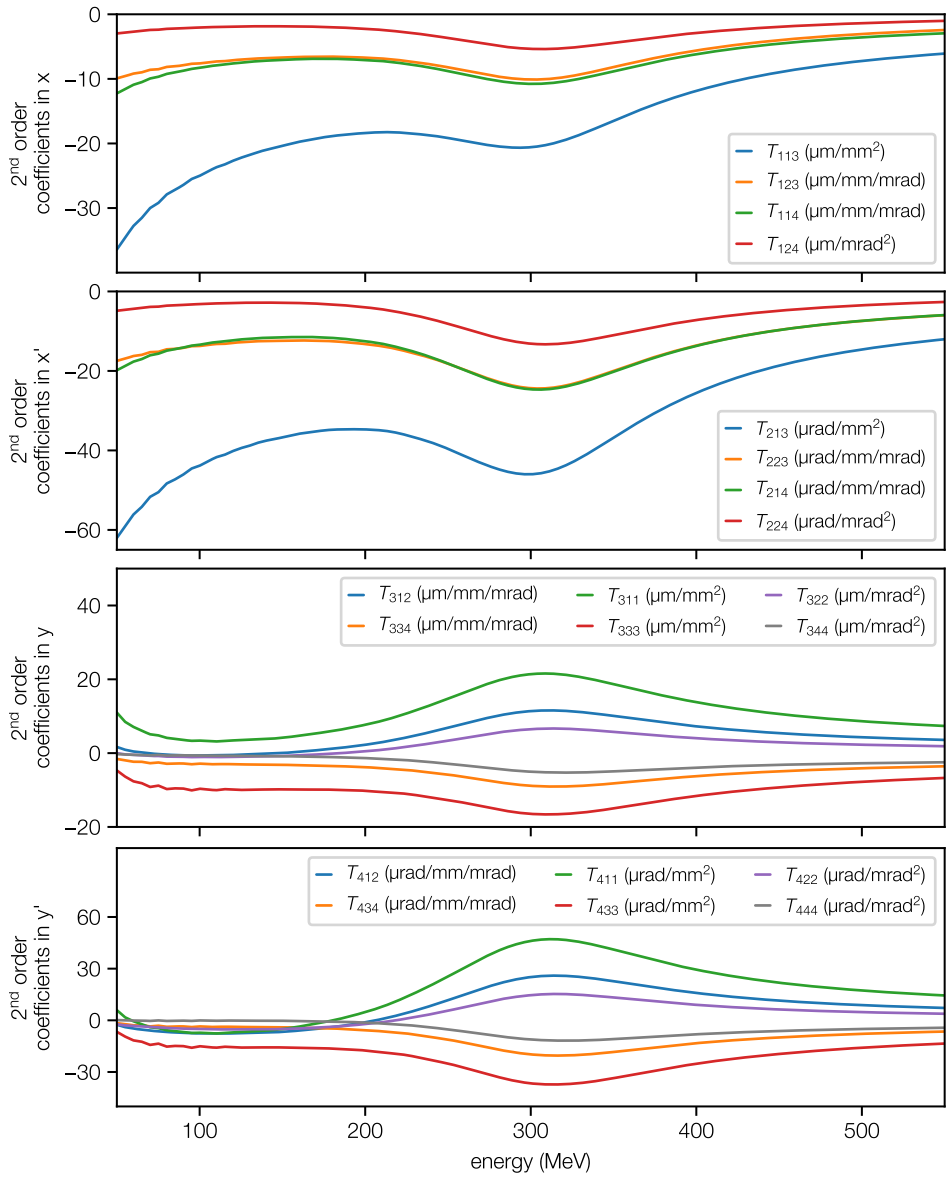

Figure 3.15. – Second order transfer elements of the spectrometer dipole. Figure adapted from [88].

position reading less than $\pm 5\,\mathrm{mm}$ reduces this error to below the single pixel limit. In case of focused electron beams the electron focus is kept centered inside the cavity BPMs and on the spectrometer screen and second order effects by the dipole are negligible. However, transverse alignment between the quadrupole magnets and the electron source is required to have the electron beams exiting the doublet close to the design axis.

4. Particle Beams and Beam Transport

The important definitions for the description of particle beams and the beam transport through a magnet optics are summarized in this chapter. Special care is taken on the influence of imaging errors in the closing sections. The coordinate system is defined in appendix A.1. In the following, the electron beam properties will be discussed for the horizontal axis x, but are analogously defined for the vertical axis y.

4.1. Emittance and Phase-Space

In this thesis the phase-space is defined as the space spanned by the electrons position x and the angle x' of the electrons relative to a design axis (sometimes also referred to as the trace-space). The angle x' is further defined as the transverse electron momentum normalized to the longitudinal electron momentum,

$$x' = \frac{p_x}{p_z} \quad . \tag{4.1}$$

Experimentally, only the statistical properties of the projection of the electron beam onto a detector screen are accessible, such as

$$\begin{gathered}
\text{the mean beam position } \langle x \rangle \quad , \\
\text{the mean beam direction } \langle x' \rangle \quad , \\
\text{the rms beam size } x_{\mathrm{rms}} = \sqrt{\langle x^2 \rangle} \quad , \\
\text{the rms beam divergence } {x'}_{\mathrm{rms}} = \sqrt{\langle x'^2 \rangle} \quad , \\
\text{the correlation between transverse position and angle } \langle x\, x' \rangle \quad .
\end{gathered}$$

Here, the angled brackets denote the average, respectively the second central momentum, over all electrons of the distribution. The rms phase-space emittance, further only referred to as the emittance, is proportional to the volume occupied by the beam in phase-space [4, 96] and defined as

$$\varepsilon = \sqrt{\langle x^2 \rangle \langle x'^2 \rangle - \langle x\, x' \rangle^2} \quad . \tag{4.2}$$

Note that, due to defining the emittance in terms of the rms-beam properties it is generally defined for any particle distribution. The emittance can be illustrated as the area of an ellipse with equivalent rms-properties and covering a certain fraction of the particle distribution. The phase-space dynamic of the electron beam is then equivalent to the transformation of the phase-space ellipse. In case of a spatially and angularly Gaussian distributed beam the rms emittance coveres a fraction of 68 % of the particles.

Along an accelerator beamline, the rms beam size and divergence of an electron beam are constantly changing. However, the phase-space volume, i.e. the emittance, is a conserved quantity in the absence of accelerating fields and in case of a sufficiently small energy variation within the beam. In order to account for a change in longitudinal momentum, respectively for acceleration of the electron beam, the normalized emittance is defined as

$$\varepsilon_{\mathrm{n}} = \gamma\,\varepsilon \quad , \tag{4.3}$$

which is a conserved quantity under acceleration. Here, γ is the relativistic Lorentz factor. The normalized emittance is thus an important beam parameter in accelerator physics. In case of a known focusing optics, the normalized emittance, once determined, can be used to compute the electron beam size at any position along the beamline.

However, in case of a large energy variation within the beam, the total energy projected emittance is not conserved. Figure 4.1 shows an ASTRA [95] simulation of the evolution of the rms-beam size and the phase-space ellipses of three different energy beams along the LUX focusing doublet. In the initial drift section, the three energy-slice ellipses shear coherently according to

$$\langle x\,x'\rangle_s = \langle x\,x'\rangle_0 + z\langle x'^2\rangle_0 \quad , \tag{4.4}$$

since the divergence is independent of the beam energy. Inside the first quadrupole magnet Q_1, the beam is chromatically focused and the different beam energies thus transform differently in phase-space. After the second quadrupole magnet the beam divergence is reduced to a minimum, but the energy-slice phase-space ellipses are sheared and not overlapping. Hence, the total phase-space area occupied by all energy-slices is larger and the total emittance increased. This is called chroamtic emittance growth [97].

Without derivation [41], a chromatic term adds quadratically to the initial beam emittance $\varepsilon_{\mathrm{n},0}$ during beam transport, such that

$$\varepsilon_n = \sqrt{\varepsilon_{\mathrm{n},0}^2 + \varepsilon_{\mathrm{chr}}^2} \quad , \tag{4.5}$$

where ε_n is the total emittance and $\varepsilon_{\mathrm{chr}}$ the chromatic fraction of the emittance added during beam transport.

As an example, in order to quantify the chromatic fraction of the emittance, the projected normalized emittance can be expressed in x-p_x space. Using the relation $p_x/(m_0c) = \gamma x'$,

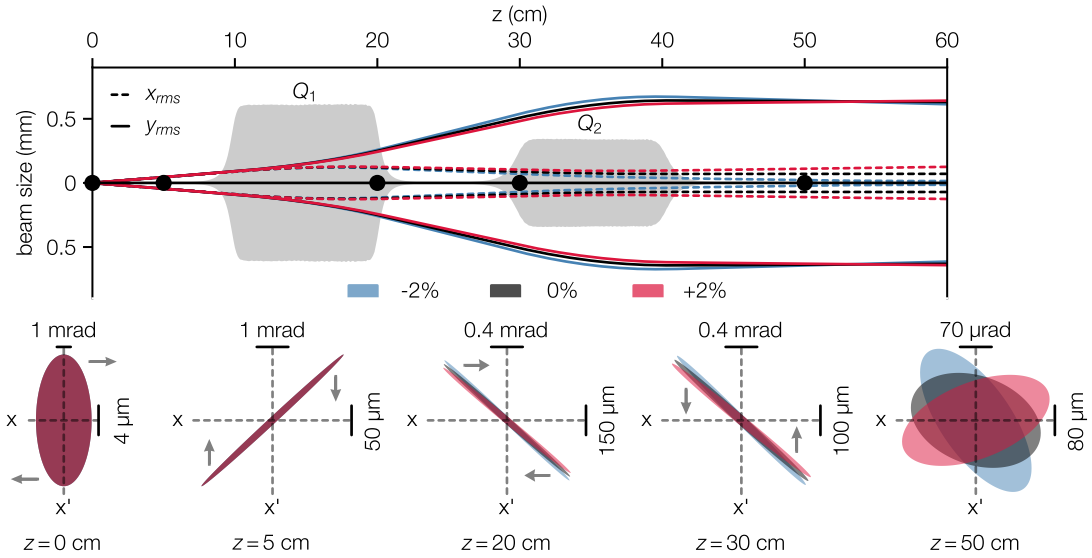

Figure 4.1. – Electron phase-space along the LUX focusing doublet. The top plot shows the evolution of the horizontal (dashed) and vertical (solid) rms-beamsize inside the quadrupole doublet for three different beam energies with an energy variation of ±2 %. The presence of the quadrupole field is illustrated in grey (compare to figure 3.3). The phase-space ellipses of the three energy slices at five different positions (black dots) are plotted below. Due to the chromatic focusing by the magnets, the phase-space ellipses shear incohernently. The grey arrows denote the phase-space manipulation introduced by the subsequent drift or focusing magnet.

the projected normalized emittance (compare to appendix A.2) reads

$$\varepsilon_{\mathrm{n},x-p_x} = \sqrt{\langle x^2\rangle \left\langle \gamma^2\, x'^2\right\rangle - \langle x\,\gamma\, x'\rangle^2} \quad . \tag{4.6}$$

In free drift, neglecting a correlation between electron position x and momentum p_z and considering the relative energy spread σ_E/E with

$$\left(\frac{\sigma_E}{E}\right)^2 = \frac{\langle\gamma^2\rangle - \langle\gamma\rangle^2}{\langle\gamma\rangle^2} \quad , \tag{4.7}$$

as in [42], equation 4.6 can be expanded to

$$\varepsilon_{\mathrm{n},x-p_x} = \sqrt{\langle\gamma\rangle^2\big(\langle x^2\rangle\langle x'^2\rangle - \langle x\,x'\rangle^2\big) + \big(\frac{\sigma_E}{E}\big)^2\langle\gamma\rangle^2\langle x^2\rangle\langle x'^2\rangle} \quad . \tag{4.8}$$

The first term in equation 4.8 is the normalized emittance, which is conserved during drift. The second term is the chromatic contribution to the emittance $\varepsilon^2_{\mathrm{chr}}$. $\varepsilon_{\mathrm{chr}}$ is linearly dependent on the rms-energy spread. In contrast to the first term, no linear correlation is subtracted andthe chromatic contribution is thus linearly growing in drift. Note that equation 4.8 is only valid in the initial drift space and not valid inside or after a focusing magnet, since a focusing magnet is energy dependently manipulating the beams phase-space. The description of the evolution of the beam emittance and the initital beam parameters inside the LUX magnet optics are discussed in the following.

4.2. Beam Transport and Emittance Measurement Methods at LUX

The particle motion in linear beam dynamic can be expressed in terms of matrix multiplication with a transport matrix M [4, 96]. The mean position and mean direction of the electron beam at any position s inside the accelerator are determined by the beam optical elements with

$$\big\langle x\big\rangle_s = M_{11}\big\langle x\big\rangle_0 + M_{12}\big\langle x'\big\rangle_0 \tag{4.9}$$

$$\big\langle x'\big\rangle_s = M_{21}\big\langle x\big\rangle_0 + M_{22}\big\langle x'\big\rangle_0. \tag{4.10}$$

The beam size, divergence, and correlation in horizontal trace-space are determined equivalently by calculating the second central moments with [96]

$$\big\langle x^2\big\rangle_s = M_{11}^2\big\langle x^2\big\rangle_0 + 2\,M_{11}M_{12}\big\langle x\,x'\big\rangle_0 + M_{12}^2\big\langle x'^2\big\rangle_0 \tag{4.11}$$

$$\big\langle x\,x'\big\rangle_s = M_{11}M_{21}\big\langle x^2\big\rangle_0 + (M_{11}M_{22}+M_{12}M_{21})\big\langle x\,x'\big\rangle_0 + M_{12}M_{22}\big\langle x'^2\big\rangle_0 \tag{4.12}$$

$$\big\langle x'^2\big\rangle_s = M_{21}^2\big\langle x^2\big\rangle_0 + 2\,M_{21}M_{22}\big\langle x\,x'\big\rangle_0 + M_{22}^2\big\langle x'^2\big\rangle_0. \tag{4.13}$$

The index 0 refers to the initial particle distribution before transport, e.g. the beam distribution at the end of the plasma target. M_{ij}, $i, j \in \{1, 2\}$ refer to the transport matrix elements. A more detailed derivation of particle beam dynamics is presented in appendix A.2. The matrix elements are further functions of the beam energy E, the focusing forces of the optical elements $\mathbf{k}$ and the coordinate s.

Equation 4.11 connects the beam size $x_{\mathrm{rms,s}} = \sqrt{\langle x^2 \rangle_s}$, e.g. measured at a scintillator screen, to the initial beam parameters, namely the intial beam size $x_{\mathrm{rms},0}$, the initial beam divergence $x'_{\mathrm{rms},0}$ and an initial phase-space correlation $\langle x\, x' \rangle_0$ at the source, respectively behind the plasma. It is thus connected to the initial beam emittance (see equation 4.2). Consequently, equation 4.11 can be used to experimentally determine the beam emittance. The beam size is measured for varying matrix elements M_{11} and M_{12}, for example varying in the focused energy, and equation 4.11 is fit to the measured rms width data as a function of the varied parameter. The fit results are the beam properties at the position $s = 0$.

Standard methods to measure the beam emittance typically suffer from the large energy-spread and shot-to-shot fluctuations in beam parameters of plasma-generated electron beams. A method to circumvent the challenge of large energy-spread beams is a method proposed by *Weingartner et al.* [19], where the electron beam is focused into a dispersive electron spectrometer. Inside the electron spectrometer, the beam energies are spatially separated and can be analysed individually on the spectrometer screen. *Weingartner et al.* further propsed to measure the beam size on the spectrometer screen simultaneously for different energy-slices of the beam, which enables to measure the beam emittance from a single shot. The implementation of this single-shot emittance diagnostics at LUX is presented in the following sections.

4.2.1. Experimental Setup

At LUX, the electron beams diverging from the plasma are focused by the quadrupole doublet into the electron spectrometer, see figure 4.2. In the horizontal axis, the beam is focused by the first quadrupole magnet and defocused by the second. In the vertical axis the beam is first defocused before being focused. In total, the beams divergence is reduced in both axis after the doublet, but the beam is asymmetrically large. Inside the spectrometer dipole the beam is additional focused in the dispersive axis and defocused in the non-dispersive axis, due to fringe field effects. The quadrupole field gradients are chosen to result in a total focusing of a certain beam energy in both axis on the spectrometer screen.

Describing the beam transport by means of linear beam dynamic is not capable of describing the focusing forces acting on the beam inside the plasma. It is only capable of describing the beam propagation in terms of free drift from an effective source position

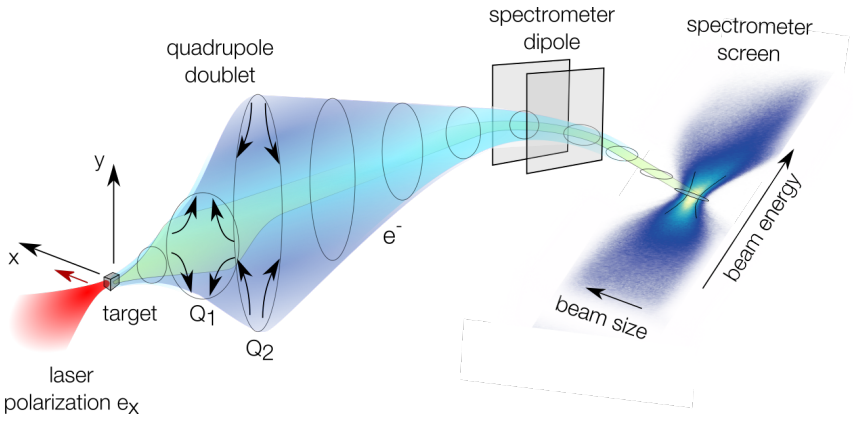

Figure 4.2. – Illustration of the experimental setup at LUX. The laser (red, polarized in x) is focused into the plasma target. The generated electron beams diverging from the plasma are captured by the quadrupole doublet and focused asymmetrically onto the spectrometer screen. The spectrometer dipole is dispersing the beam in the vertical y-axis.

at a virtual plane inside the target area (see figure 4.3). This virtual source position can deviate from the longitudinal position of the target exit. E.g. a mean phase-space correlation of the beam out of the plasma directly translates into a longitudinal shift Δz of the virtual source plane (according to equation 4.4). The beam optics is set to image the electron beam from this virtual source into the spectrometer screen plane.

Due to the short focal length of the quadrupole magnets of 0.1 m and the long drift length to the electron spectrometer of 8 m, the LUX focusing optics is acting as a telescope. Including the additional focusing and defocusing forces by the spectrometer dipole, the source size at the virtual plane is magnified by a factor of in total 315 (9.5) in the horizontal (vertical) axis, in case of a 150 MeV beam. The strength of magnification in general reduces towards higher energies (e.g. down to a magnification factor of 150 at 400 MeV) due to a less strong defocusing of the beam by the spectrometer dipole.

Hence, the LUX beam optics on the one hand features a high energy resolution in the dispersive axis, since the different beam energies are well separated in the screen plane. On the other hand, the resolution in beam size detection in the non-dispersive axis is enhanced. A typical initial source beam size of 3 µm is imaged to a focus size of 1 mm in the non-dispersive plane. In the dispersive plane, the corresponding focus size is only 30 µm large and therefore much smaller than the size imaged to a single camera pixel by the objectives. The energy bins corresponding to the camera pixel rows can thus be treated as separate energy-slices of the beam. The corresponding energy width of the single slices is on the 0.1 % level which is comparable to the energy deviation of electron beams generated by conventional accelerator technology [3].

However, the quadrupole doublet can only be set to focus one particular beam energy.

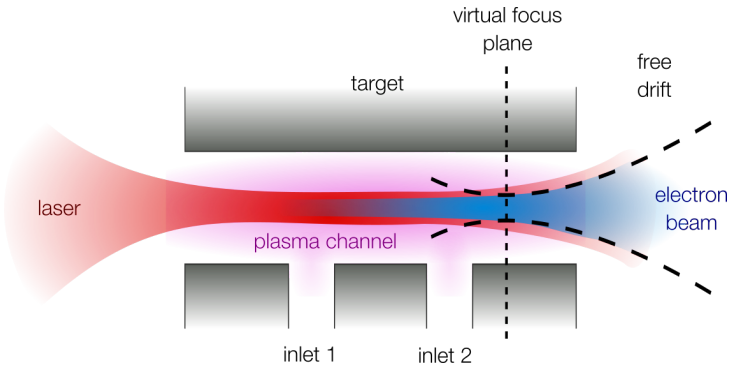

Figure 4.3. – illustration of the plasma capillary target at LUX. The electron phase-space can be modified in the density downramp at the target exit. The electron beam size and divergence then evolve from a virtual source plane, where the phase-space correlation is defined to be 0.

All other electron energies will be either less focused or over-focused by the doublet. This results in lower energies to be focused before the spectrometer screen and higher energies to be focused behind. In both cases the detected beam size on screen increases with the energy deviation from the focused energy.

The transport matrix elements determining the horizontal and vertical beam size on screen are plotted as a function of the energy in figure 4.4 for an intitially symmetric 3.1 µm large and 0.8 mrad divergent beam imaged into the spectrometer screen plane.

A consequence of the chromatic focusing of the doublet is that the beam size increases rapidly in the dispersive axis for off-focus energies and the high energy resolution only being present in a narrow energy interval of ±2 % centered around the focused energy. Inside this narrow energy band, the rms-beam size can be detected individually for each energy slice that corresponds to the limit of a single camera pixel row.

Figure 4.5a shows an example image of a beam profile of a focused electron beam on the spectrometer screen. The rms beam size is measured for every energy-slice in a narrow interval of ±2 % arround the focused energy of 149 MeV. The measured beam size is separately plotted in figure 4.5b. The beam size on screen shows a minimum at the focused energy and is increasing towards higher and lower energies.

In case of an initial mean angle of the electron beam from the source relative to the design axis, the electron beam enters the quadrupole doublet with a transverse offset from the magnetic axis. The additional dispersion by the quadrupole magnets in combination with the long drift to the spectrometer dipole causes the effective dispersion axis on the spectrometer screen to be sheared. In case of an initial horizontal beam pointing the electron profile on screen is sheard by a shearing angle θ_s, see figure 4.5a. The shearing angle θ_s is thus a direct measure of the initial beam angle from the source in the horizontal

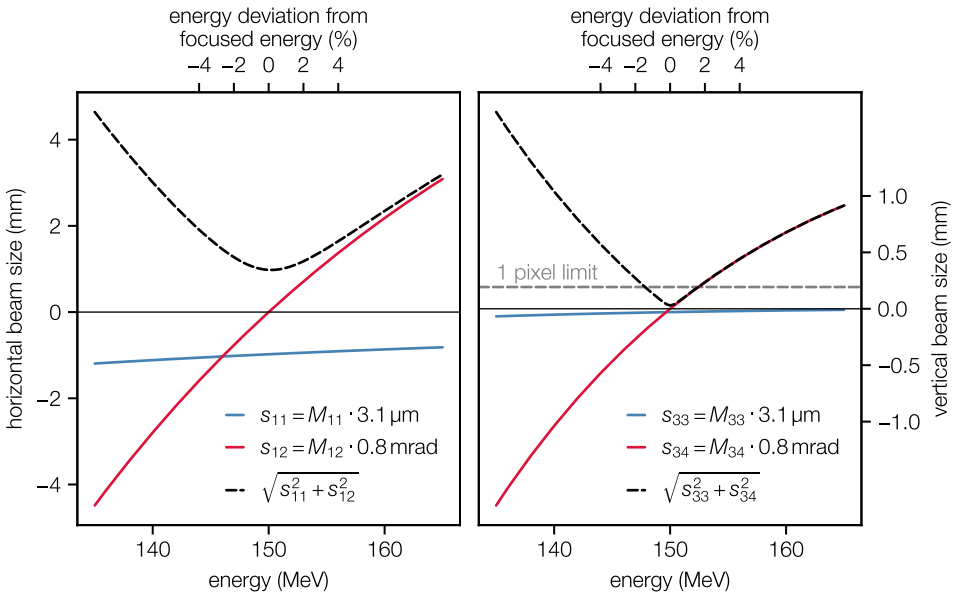

Figure 4.4. – Horizontal and vertical beam size on screen in dependence of the beam energy. The image of the electron focus is much larger in the horizontal x-axis than in the vertical y-axis due to the asymetric focusing by the doublet. In the dispersive plane (y), the imaged beam size is below or close to the single pixel resolution limit in an energy range of $-2\,\%$ to $2\,\%$ around the focused energy.

direction with

$$\langle x \rangle_s = M_{11} \langle x \rangle_0 + M_{12} \langle x' \rangle_0. \tag{4.14}$$

Single shots with a measured shearing anlge $\theta_s > 0.1\,\text{mrad}$ are excluded from the emittance analysis since the influence of the vertical beam properties onto the measurement of the horizontal beam properties increases with θ_s (see section 4.3.4).

4.2.2. RMS Beam Size Detection

As described above, the rms beam size is calculated for each energy slice individually. Figure 4.6a shows an example image of a detected focused beam profile on the spectrometer screen. Five lineouts at the focused energy and $\pm 2.5\,\text{MeV}$ and $\pm 5\,\text{MeV}$ are plotted in different colors in figure 4.6b and are additionally marked in the same color code in 4.6a. The weighted mean $\langle x \rangle$ and rms beam size x_{rms} are calculated analytically for each energy slice.

$$\langle x \rangle = \sum (c_i x_i) / \sum c_i \quad , \tag{4.15}$$

$$x_{\text{rms}} = \sqrt{\sum c_i (\langle x \rangle - x_i)^2 / \sum c_i} \quad . \tag{4.16}$$

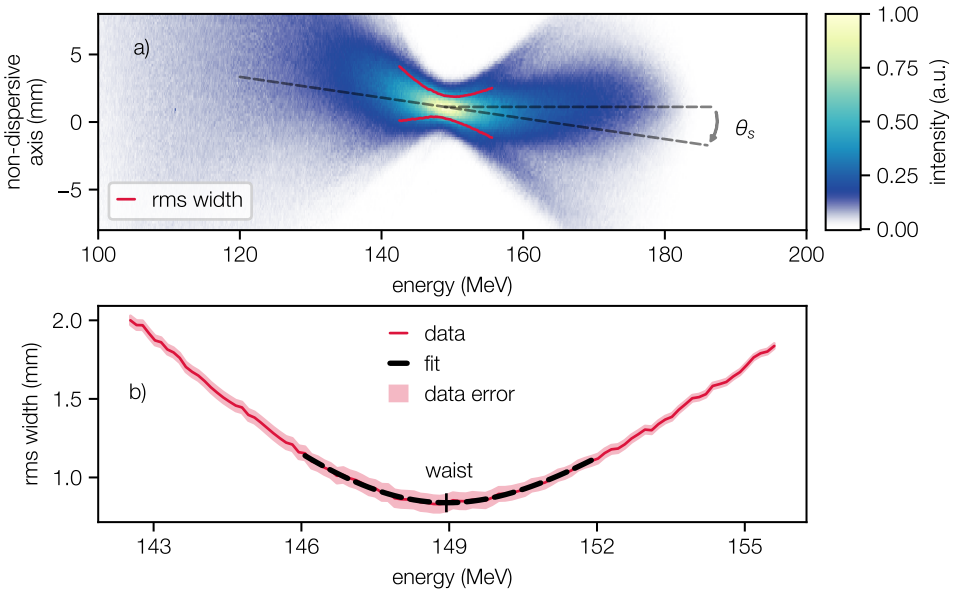

Figure 4.5. – a) Example camera image of a measured beam profile on the spectromter screen. The rms beam width is measured in the non-dispersive axis for each energy slice and plotted in b). Equation 4.11 is fit to the data in order to retrieve the beam emittance. The dispersive axis on screen can be sheared by the angle θ_s in case of initial horizontal beam pointing.

Here, the summation is performed over all i pixels in a single column with coordinates x_i and counts c_i. The presence of camera noise in the signal can cause the rms calculation to result in a too large value, since the influence of counts on the rms increases with the square of the distance from the mean signal position.

In order to suppress the influence of camera noise onto the rms beam size calculation the signal outside an interval $[\langle x\rangle - n_{\mathrm{cut}} \cdot x_{\mathrm{rms}}, \langle x\rangle + n_{\mathrm{cut}} \cdot x_{\mathrm{rms}}]$ is cropped to zero and the rms beam size is re-calculated. The iterative decrease in calculated rms beam size is illustrated in figure 4.6c. The plotted beam profile corresponds to the central energy slice lineout at the focused energy in figure 4.6a. The dashed lines denote the interval limits considered for the rms calculation for the 1st, 2nd, and 3rd iteration. The resulting ± 1 rms beam size is plotted as a filled area under the profile curve centered around the profiles weighted mean. For this plot a cut factor n_{cut} of 2 has been chosen examplarily in order to illustrate the influence of the profile cropping onto the rms calculation. The calculated rms beam size reduces with each iteration. However, the rms beam size in figure 4.6c is not converged after $n_{\mathrm{rep}} = 3$ iterations.

Further, with a cut factor of $n_{\mathrm{cut}} = 2$, the signal is already severly cut at the outer wings to values up to $\sim 20\,\%$ of the maximum signal. In case of too strong signal cropping the calculated rms can underestimate the real rms width of the distribution. This effect is

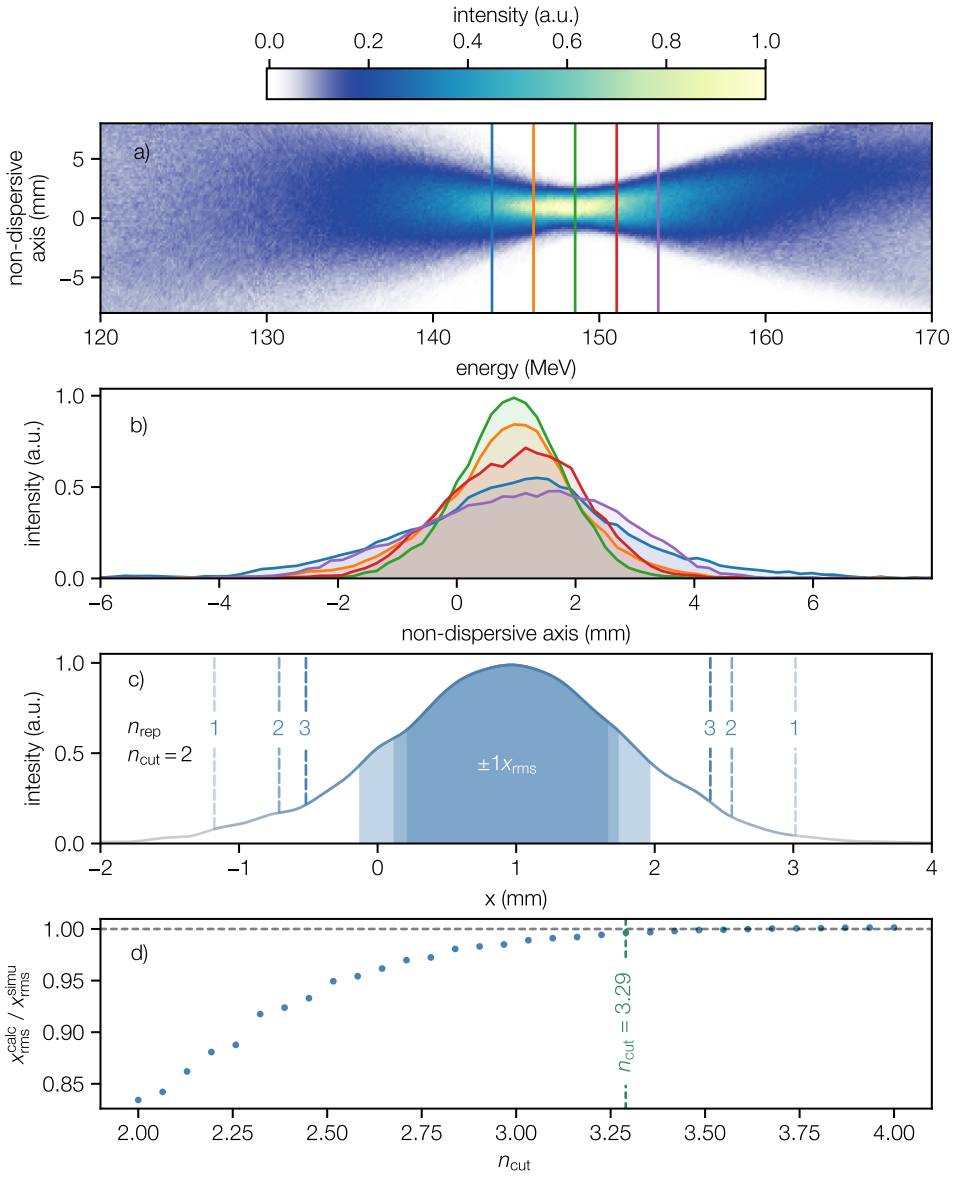

Figure 4.6. – a) Example camera image of a measured beam profile on the spectromter screen. b) Energy slice distributions at the focused energy and at ±2.5 MeV and ±5 MeV off the focused energy. c) Example of 3 iterations of rms- calulation and signal croping with a cut factor $n_{\mathrm{cut}} = 2$. The dashed lines indicate the signal range used for the rms calculation after each iteration. The filled area below the signal curve denote the calculated ±1 rms width after each iteration. With $n_{\mathrm{cut}} = 2$ too much signal is cut at the wings. d) Comparison of simulated and calculated rms beam size. A cut factor of n_{cut} of 3.29 is used for the analysis. The error in rms detection increases rapidly for smaller cut factors.

in paricular strong in case of binned data (as it is the case for the pixel counts) and the signal only being located within a few bins (typically 10 to 30 pixels, respectively 1 mm to 3 mm).

Therefore, generic particle distributions have been generated and binned accordingly to the spectrometer screen resolution. The rms width of the resulting histogram was iteratively calculated with $n_{\mathrm{rep}} = 3$ iterations and for different cut factors n_{cut}. The ratio between the iteratively calculated rms beam width and the simulated "input" beam width in dependence of the cut factor is plotted in figure 4.6d. The calculated rms understimates the width of the distribution for smaller cut factors. In case of a cut factor of 2 as exemplarily used in figure 4.6c the error in calculated rms is already 15 %.

The cut factor has to be chosen as a compromise between accuracy in rms beam size calculation and a potential error from the camera noise. With the observed signal-to-noise level of the spectrometer cameras (see section 4.3.5) a cut factor of $n_{\mathrm{cut}} = 3.29$ is chosen for the data analysis in chapter 6. The error in rms beam size detection is thus on the 1 % level as highlighted in figure 4.6d. The area inside $\pm 3.29\, x_{\mathrm{rms}}$ of a gaussian distribution corresponds to 99.9 % of the total distribution.

For the emittance analysis discussed in the following section only energy slices with the full signal interval $[\langle x \rangle - n_{\mathrm{cut}} \cdot x_{\mathrm{rms}}, \langle x \rangle + n_{\mathrm{cut}} \cdot x_{\mathrm{rms}}]$ being detectable on screen are considered. Electron beam profiles on screen, that are too far off the screen center in the non-dispersive axis are therefore excluded. Hence, increasing the cut factor to even larger values causes more shots to be dropped from the analysis. With a cut factor of 3.29 the rms calculation converges after 3 iterations. The measured rms beam size on screen is then used for the emittance retrieval.

At LUX two different methods are used to measure the beam emittance: A quadrupole scan method and the single-shot method. The differences between the two methods are discussed in the following.

4.2.3. Quadrupole-Scan Method

The field gradients of the quadrupole magnets are varied to focus different beam energies onto the spectrometer screen. Accordingly, the imaged beam size on the spectrometer screen for each beam energy will change with the quadrupole focusing. The change in beam size at a single energy slice, respectively a single pixel column of constant energy

E, is measured in dependence of the focused energy F.

$$\begin{aligned}
\langle x^2 \rangle_{E,F_1} &= M_{11}^2(E,F_1)\langle x^2 \rangle_0 + 2\, M_{11}(E,F_1)M_{12}(E,F_1)\langle x\, x' \rangle_0 + M_{12}^2(E,F_1)\langle x'^2 \rangle_0 \\
\langle x^2 \rangle_{E,F_2} &= M_{11}^2(E,F_2)\langle x^2 \rangle_0 + 2\, M_{11}(E,F_2)M_{12}(E,F_2)\langle x\, x' \rangle_0 + M_{12}^2(E,F_2)\langle x'^2 \rangle_0 \\
&\vdots \\
\langle x^2 \rangle_{E,F_n} &= M_{11}^2(E,F_n)\langle x^2 \rangle_0 + 2\, M_{11}(E,F_n)M_{12}(E,F_n)\langle x\, x' \rangle_0 + M_{12}^2(E,F_n)\langle x'^2 \rangle_0
\end{aligned}$$

This measurement can be done individually for multiple energy slices. This method is equivalent to a standard quadrupole scan. The only difference is that the electron beam is additionally dispersed by the spectromter dipole. The advantage is that single energy slices with a relative energy bandwidth of 0.1 % can be analyzed separately. However, only the beam size in the non-dispersive axis of the spectrometer is accessable.

4.2.4. Single-Shot Method

An alternative method to determine the beam emittance is to detect the beam size for different energy-slices E_i, while the quadrupole focusing is kept unchanged.

$$\begin{aligned}
\langle x^2 \rangle_{E_1,F} &= M_{11}^2(E_1,F)\langle x^2 \rangle_0 + 2\, M_{11}(E_1,F)M_{12}(E_1,F)\langle x\, x' \rangle_0 + M_{12}^2(E_1,F)\langle x'^2 \rangle_0 \\
\langle x^2 \rangle_{E_2,F} &= M_{11}^2(E_2,F)\langle x^2 \rangle_0 + 2\, M_{11}(E_2,F)M_{12}(E_2,F)\langle x\, x' \rangle_0 + M_{12}^2(E_2,F)\langle x'^2 \rangle_0 \\
&\vdots \\
\langle x^2 \rangle_{E_n,F} &= M_{11}^2(E_n,F)\langle x^2 \rangle_0 + 2\, M_{11}(E_n,F)M_{12}(E_n,F)\langle x\, x' \rangle_0 + M_{12}^2(E_n,F)\langle x'^2 \rangle_0
\end{aligned}$$

Due to the multi-percent energy-spreads of laser-wakefield accelerated electron beams, the beam size of the different energy slices can be simultaneously detected and the emittance can thus be measured from a single-shot [19]. However, the single-shot method forces the assumption, that the initial beam properties are the same for all energies E_i considered for the fit of equation 4.11 [34].

In general, the focusing strength of a quadrupole magnet is linearly proportional to the field gradient and inversly proportional to the beam energy

$$k \propto g/E.$$

It is thus mathematically equivalent to either increase the beam energy or to reduce the field gradient by the same factor. However, this symmetry is not given for the focusing by the spectrometer dipole. The quadrupole scan and the single-shot method therefore are two independent techniques to measure the emittance.

The required accuracy in the description of the optical elements, the electron beam imaging and beam detection in the LUX beamline is discused in the following section.

4.3. Electron Beam Imaging and Detection Accuracy

Accurate imaging of the electron beam in both transverse axis from a plane in the target area onto the spectrometer screen is crucial for the accuracy in emittance measurements. In particular, due to the large magnification of the electron beam by the beam optics, also small deviations in the beam focusing can result in a large error in the reconstructed beam properties.

In order to estimate the required precision and the remaining error in the description of the electron beam and beam optics, both analytical considerations and particle tracking simulations are performed. Quasi-random electron phase-space distributions are generated and tracked to the spectrometer screen plane. Generic spectrometer camera images are created from the electron distributions on screen including a modeling of the camera noise. Finally, the generic images are processed by the same analysis tools used for the measured data.

The purpose of this chapter is to discuss the precision limits in initial phase-space reconstruction by the emittance measurement methods and to distinguish between systematic and statistical errors. Only a selection of the most prominent parameters effecting the emittance measurement are discussed in the following. The parameters are sorted into effects by initial beam parameters, the beam focusing, the optics alignment and the analysis method.

The errors on the reconstructed beam emittance, size, divergence and phase-space correlation are simulated for various error sources. Due to a residual error in rms-detection on screen (see section 4.2.2), the reconstructed phase-space properties deviate from the simulated properties by a few permille.

4.3.1. Source Phase-Space Effects

The general change in rms beam width on screen in dependence of the beam energy by a change in initial beam parameters is shown examplarily in figure 4.7.

Initial Phase-Space. The focus size on screen, i.e. the beam size at the focused energy of 150 MeV in this example, is mostly determined by the source beam size. The increase in beam size on screen for off-focus energies is dominated by the initial beam divergence from the source (see subfigure a).
An additional correlation in transverse phase-space at the source results in a shift of the focused energy, as shown in subfigure b. However, in this generic case also the emittance changes since the source beam size and divergence are kept constant. This causes the focus size on screen to be reduced in comparison to a beam with no initital correlation.

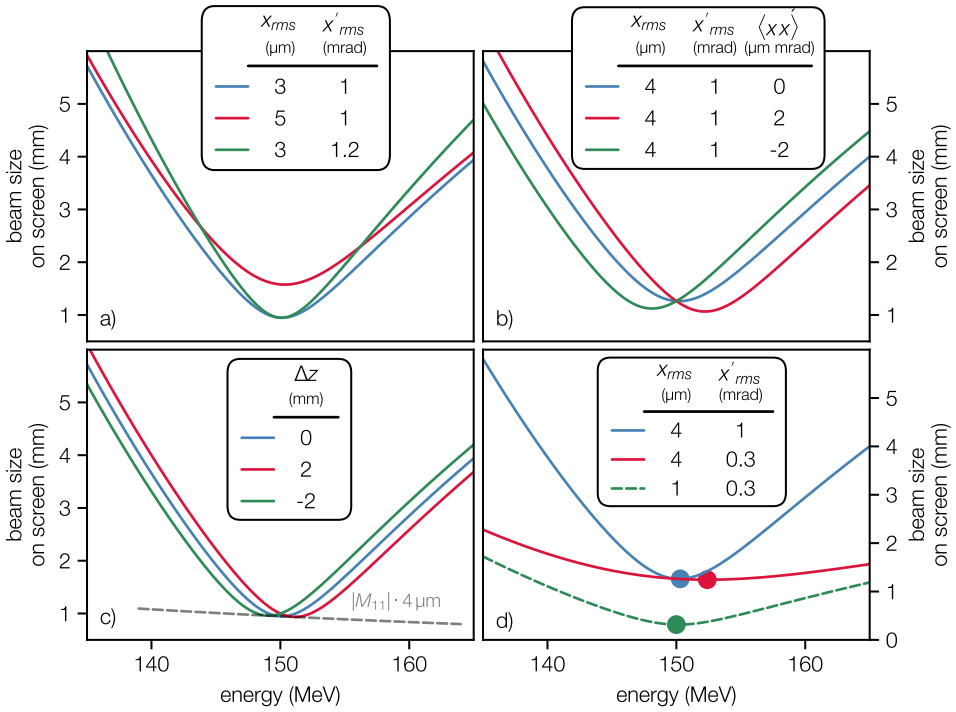

Figure 4.7. – a) Influence of the initial beam size and divergence on the measured beam profile on the spectrometer screen. b) A correlation in phase-space at the imaged plane shifts the focused energy on screen. c) An equivalent effect is observed for a mismatch Δz between imaged plane and virtual source plane. d) In case of a too small initial beam divergence, respectively a too large intital beam size, the focused energy on screen can be detected wrongly.

Virtual Focus. Subfigure 4.7c shows the effect on the beam width on screen by a shift of the virtual source plane by ±2 mm. Here, also a shift of the focus position in the energy axis is observed, but since the simulated beams are having the same emittance, the focus size on screen just follows a curve introduced by the beam optics M_{11} element. Setting the quadrupole doublet to image a plane being too far from the virtual source plane, is equivalent to setting a too long focal length of the focusing magnets, respectively a too small field gradient. Therefore a beam energy smaller than the set focused energy is focused onto the spectrometer screen. Note that a mismatch between the imaged and virtual source plane is further equivalent to a correlation in transverse phase-space due to the additional or missing drift of the beam between the two planes.

In case of a well characterized beam optics this behaviour can be used to determine the mismatch between the virtual source plane and the plane imaged by the magnet optics. However, there are multiple other effects that result in a similar shift in focused energy on screen, which can lead to an error in emittance measurement if the effects are not distinguishable.

Beam Size and Divergence Ratio. For instance, the minimum beam size position, respectively the focused energy can be detected wrongly in case of a large initial beam size and a comparably small beam divergence imaged onto the spectrometer screen. If the ratio between initial beam size and divergence is too large, the influence on the change in beam size on screen by the optics M_{11} element causes the detected minimum beam size to be located towards higher energies, see subfigure 4.7d. In this case, the increase in beam size on screen by the beam divergence is less than the decrease in beam size by the M_{11} element. The shift in detected focused energy by this effect was simulated to be negligible for a ratio of initial beam size and divergence $x_{\mathrm{rms}}[\mu\mathrm{m}]/x'_{\mathrm{rms}}[\mathrm{mrad}] < 5$. The presence of such a shift can further be experimentally determined by reducing the influence of the M_{11} element in the fit of equation 4.11 by quadratically subtracting a term $s_{\mathrm{red}} M_{11}$, such that

$$\left\langle x^2 \right\rangle_s - \left(s_{\mathrm{red}} M_{11}\right)^2 = M_{11}^2 (\left\langle x^2 \right\rangle_0 - s_{\mathrm{red}}^2) + 2\, M_{11} M_{12} \left\langle x\, x' \right\rangle_0 + M_{12}^2 \left\langle x'^2 \right\rangle_0. \tag{4.17}$$

Here, the measured rms width on screen is globally reduced by the correct energy dependent matrix element. The value s_{red} can be interpreted as an estimated beam-size that is smaller than the measured initial beam size. Accordingly, the condition $\sqrt{\left(x_{\mathrm{rms}}^2 - s_{\mathrm{red}}^2\right)}\,[\mu\mathrm{m}]/x'_{\mathrm{rms}}[\mathrm{mrad}] < 5$ is relaxed and the focused energy is detected correctly. Fitting equation 4.17 to the reduced beam width will result the correct initial phase-space properties again.

4.3.2. Imaging Effects

The deviations introduced by inaccurate focusing of the beam by the doublet are plotted in figure 4.8. Subfigures a and c show the influence of a deviation in field gradient of the first and second quadrupole magnet onto the beam profile on the spectrometer screen.

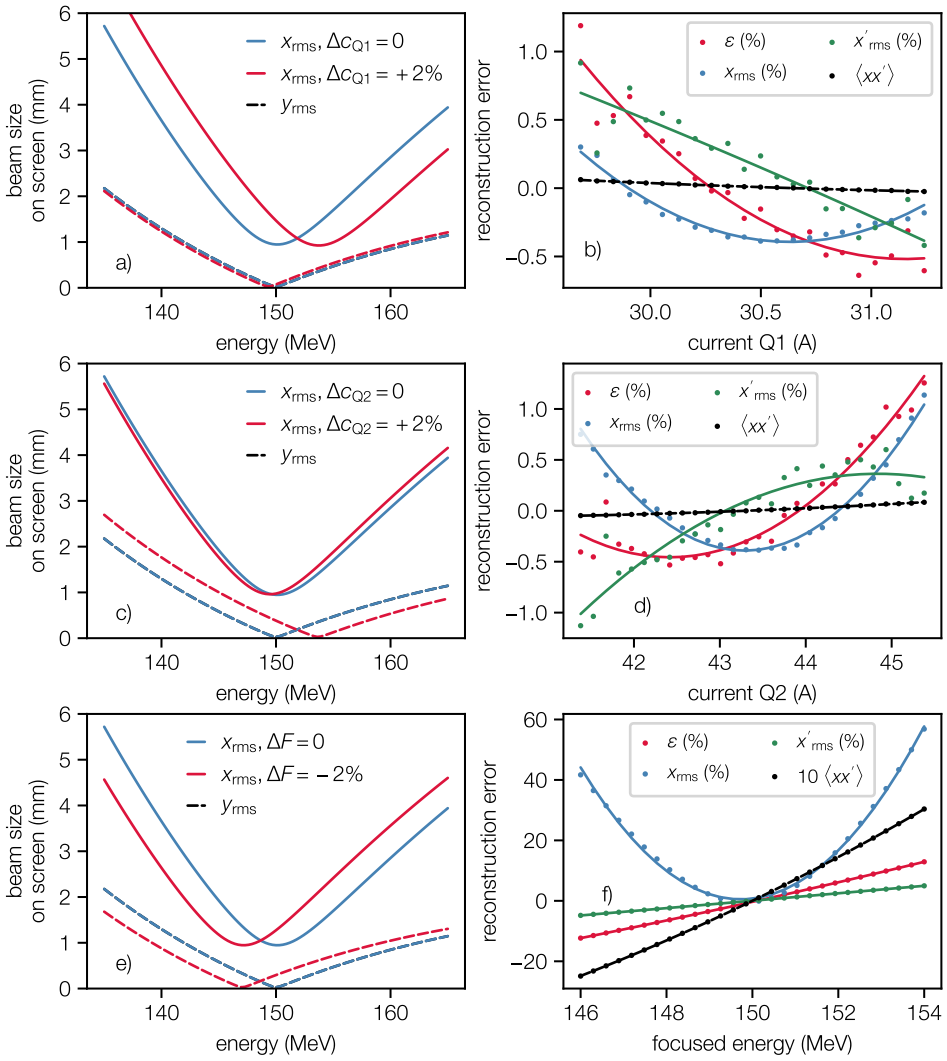

Figure 4.8. – Influence on horizontal and vertical focus position on the spectrometer screen by a calibration error in the quadrupole field gradients (left column). The error in electron beam imaging causes an error on the reconstructed source beam properties (right column).

The error on the reconstruction of the initital beam properties by these deviations is plotted in subfigures b and d. The error is plotted in dependence of a change in exciting coil current. However, this is equal to an error by the field gradient to coil current calibration, an error in effective field length or field integral, or an inaccurate modeling of the quadrupoles effective fringe field length [98].

First Magnet Field Error. A mismatch in the first quadrupole field gradient by 2 % mainly causes a shift of the horizontally focused energy. The resulting error in reconstructed emittance, beam size, beam divergence and correlation are within 1 %.

Second Magnet Field Error. A similar deviation is observed for the second quadrupole magnets field gradient. Here, mainly the vertically focused energy is shifted in the dispersive axis. In the experiment such a shift is not directly detectable and worsens the energy resolution, since horizontally and vertically focused energy mismatch.

Doublet Field Error. Subfigures 4.8e and f show the errors introduced by a deviation in focused beam energy. A mismatch in focused beam energy can be caused by multiple (allmost all) effects discussed before: A systematic error in both quadrupoles field gradient calibrations, an error in the spectrometer calibration, a mismatch in imaged and virtual source plane or a shift in detected focus position on screen by large ratio in source beam size and divergence. The error in reconstructed beam size grows quadratically with the error in focused beam energy on screen, such that a focused energy shift by only ±4 MeV causes an error in reconstructed beam size by already 40 %. Reconstructed emittance and beam divergence are increasing linearly up to errors of 10 % and 3 %, respectively. The reconstructed correlation in source phase-space can deviate by ±2 µm mrad.

Hence, setting as well as detecting the focused beam energy on screen with an accuracy better than ±1 MeV *is crucial for the measurement of the initial beam phase-space properties.*

4.3.3. Alignment Effects

Figure 4.9 summarizes the errors onto the inital beam properties by transverse misalignment between the quadrupole magnets and the electron source position. In case of the electron beam being imaged correctly, a transverse position in the virtual source plane is linearly translated into a position on the spectrometer screen. Due to the polarization of the doublet and the magnification by the beam optics a positional source offset in the horizontal axis results in a much larger offset in the spectrometer screen plane than in the vertical, i.e. the dispersive, axis. The design electron axis at LUX is defined by the two cavity BPM.

Subfigure 4.9a shows a simulated beam profile at the spectrometer screen with perfect alignment of the electron beam and the quadrupole magnets. Subfigure 4.9b shows a

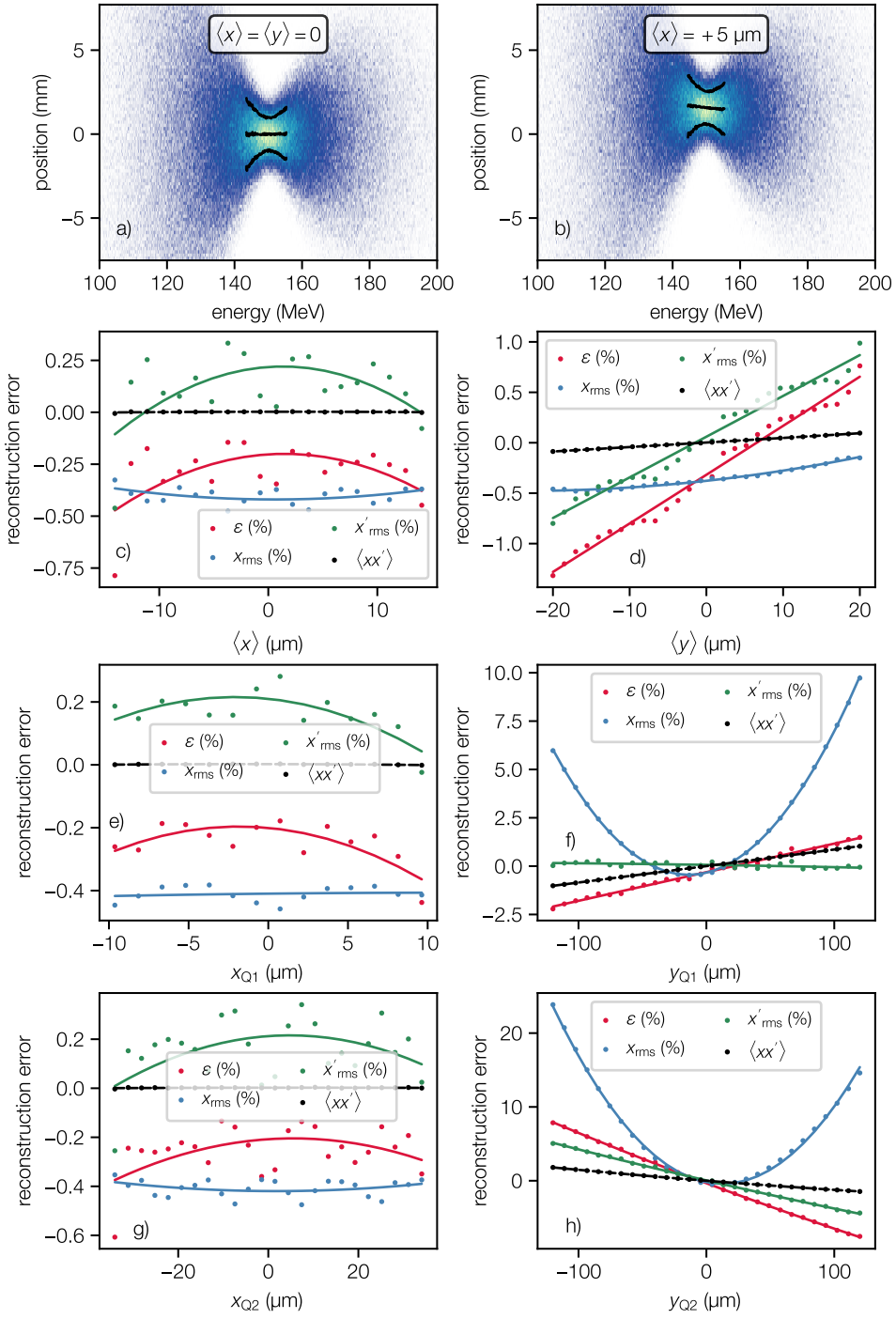

Figure 4.9. – Influence of source offsets $\langle x \rangle$, $\langle y \rangle$, and both quadrupole magnet offsets x_{Q1}, y_{Q1}, x_{Q2}, y_{Q2} in the horizontal axis, respectively the vertical axis, onto the electron beam and the reconstructed initial beam parameters. Due to the large magnification by the beam optics in the horizontal axis x, the beam is easily steered off-screen in case of a too large offset.

simulated beam profile for an electron beam with an initial offset of +5 µm at the source in the horizonal x-axis. Due to the horizontal magnification factor of 315 the focus position on screen is shifted by 1.6 mm in the non-dispersive axis. For camparison, an equal shift of the electron beam at the source in the vertical axis would only result in a shift of 50 µm in the dispersive axis of the spectrometer screen, which is below the single pixel limit.

The same behaviour occures in case of a misalignment of the quadrupole doublet relative to the electron beam source position, since the difference is mathematically only a translation of the coordinate system (with reversed sign). However, a displacement of a single quadrupole magnet, respectively a misalignment between the quadrupoles is considered separately.

Horizontal Misalignment. The plots in the left column of figure 4.9 show the error in reconstructed beam properties for a source offset (c), a misalignment of the first (e) and second quadrupole magnet (g). The plotted errors by horizontal misalignment are within ±0.5 %. However, the plotted offsets are only between 10 µm to 30 µm. Outside this intervals, the electron focus position on screen is already displaced by an amount such that the beam focus is only partially inside the screen area and the rms beam width can not be detected correctly anymore. This condition therefore displays a hard limit in horizontal alignment of the electron source and the optical elements.

Vertical Misalignment. The plots in the right column (d, f and h) show the corresponding errors by alignment for the vertical beam axis. Here, due to the smaller magnification factor in the dispersive axis, the beam can still be transported to the spectrometer screen in case of a misalignment between electron source and quadrupole magnets of a few 100 µm. A positional shift of the focused electron beam along the dispersive axis can experimentally not be distinguished from a change in focused beam energy. The resulting errors are therefore similar to the errors plotted in figure 4.8f. The error in reconstructed beam size increases quadratically with the quadrupole misalignment. Beam emittance, divergence, and phase-space correlation show a linear increase.

Hence a quadrupole alignment with a precision better than ±50 µm *is required in order to keep the systematic errors at the* 1 % *level.*

4.3.4. Pointing Effects

Another source parameter that can introduce an error in the measurement of the initial beam properties is the direction of propagation of the electron beam from the source, namely horizontal and vertical beam pointing $\langle x' \rangle_0$ and $\langle y' \rangle_0$. In case of correct imaging the focus position on screen is independent from the initial beam direction, respectively $M_{12}(E = F) = 0$. All other beam energies will be offset on screen according to equation 4.10.

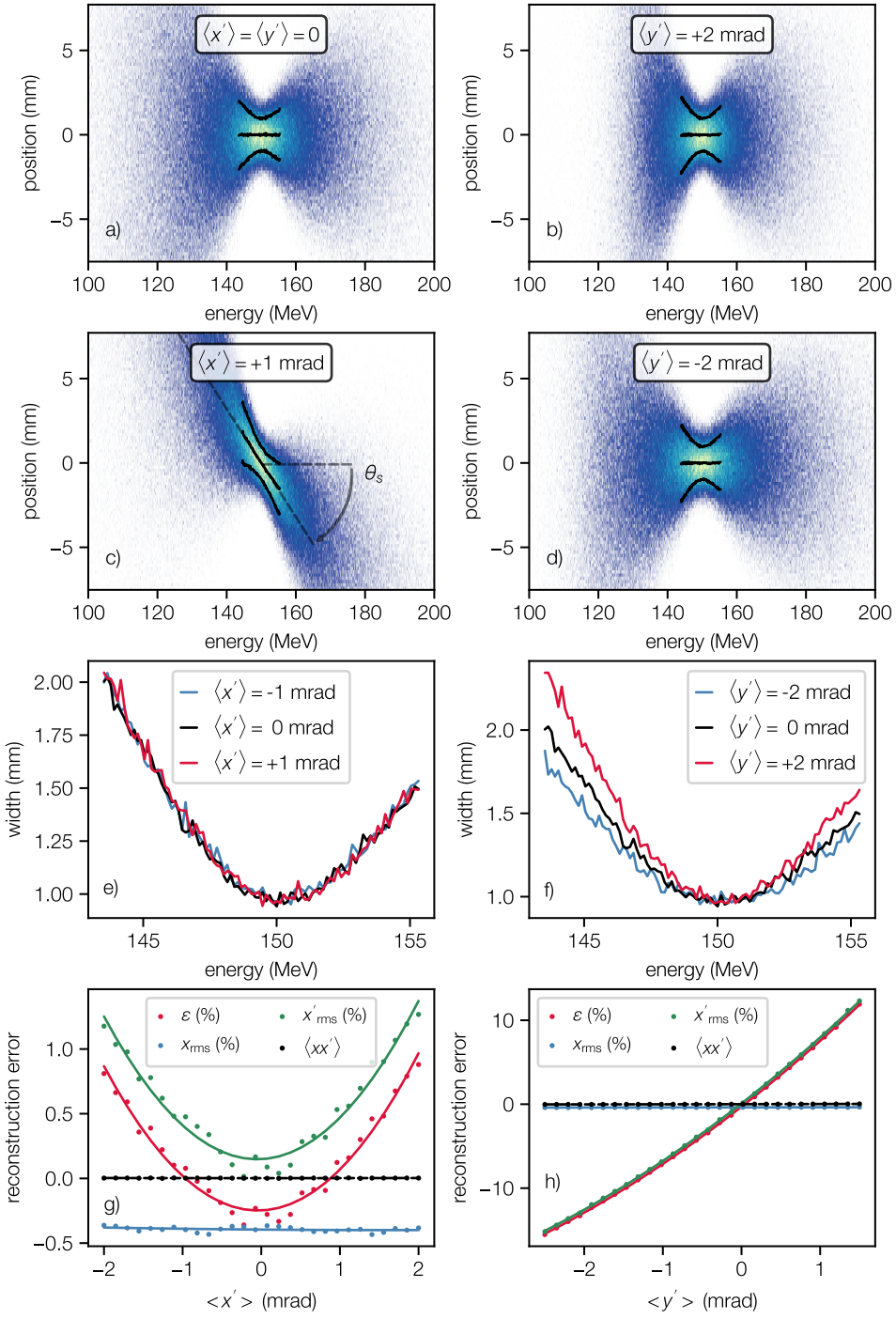

Figure 4.10. – Influence of an intital beam pointing from the plasma onto the detected beam profile on screen. The electron beam is additionally dispersed in the doublet, which causes the effective dispersion axis on screen to be sheared (left column) in case of horizontal pointing. Initial pointing in the dispersive axis of the spectromter causes the detected beam profile to be squeezed or stretched in the energy axis (right colum).

Horizontal Pointing. Figures 4.10a and b show a simulated beam profile on the spectrometer screen in case of an on-axis beam and a beam with an initial horizontal beam pointing of 1 mrad. If the beam exits the plasma with a mean angle, it will enter the quadrupole magnets with an offset to the magnetic axis and is steered and dispersed by the effective dipole component in the quadrupole field. The electrons thus have an energy dependent offset before the spectrometer dipole. After being additionally dispersed inside the spectrometer the effective dispersion axis on the spectrometer screen is sheared by the angle θ_s. The shearing anlge θ_s can be experimentally determined and can be used to measure the single-shot horizontal beam pointing. Subfigure 4.10b shows the simulated rms width on screen for beams with different initial beam pointing in the horizontal axis. The simulated beam widths for energies off the focused energy overlap, but the detected focus size on screen increases with the shearing angle of the beam profile. The error in reconstructed source size and therefore beam emittance grows quadratically with the horizontal beam pointing, as depicted in subfigure g.

Vertical Pointing. Equivalently, initial beam pointing in the vertical axis also causes the beam to be dispersed before the doublet. However, here the dispersion axis is the same as the dispersive axis of the spectrometer dipole. Hence, the additional dispersion in the vertical axis by the beam optics can not be detected experimentaly. Depending of the sign of the initial vertical beam direction, the beam is either positively or negatively dispersed before the spectromter dipole. Consequently, the total vertical dispersion either adds up or partially cancels out. The electron spectrum is therefore squeezed or stretched around the focused energy, as shown in figure 4.10f. The focus size on screen is not effected. Initial beam pointing therefore directly translates into an error in reconstruction of the source beam divergence (see subfigure h). The error in beam divergence is 6.6 %/mrad, which is one of the most dominant error sources for the emittance measurement. In particular, this introduces a systematic error in case of a mean beam pointing from the source as well as a shot-to-shot fluctuating uncertainty.

The systematic and statistical error from initital vertical beam pointing by 6.6 %/mrad *is the largest error source present in the experiments discussed in chapter 6.*

4.3.5. Beam Charge Effects

Space Charge. Space charge effects can in principle also introduce an error to the emittance measurement, since the additional defocusing force is not covered by the linear beam dynamic model [20]. However, as described in chapter 6, the electron energies considered in the experiment were well above 100 MeV and the measured charges comparibly low with 5 pC. Particle tracking simulations with *ASTRA* [95] did not show any observable effect by space charge.

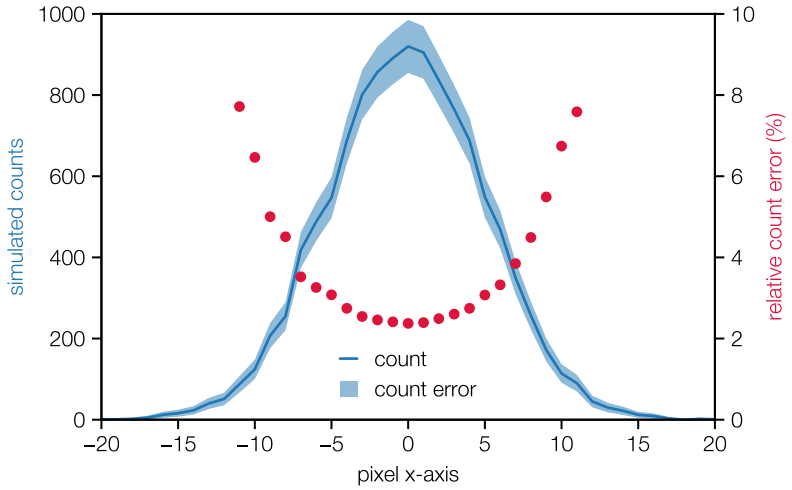

Figure 4.11. – Mono-energetic lineout of a simulated beam profile at the focused energy. The intesity profile statistically fluctuates by 3 % or more due to the finite number of electrons per camera pixel count.

Number of Electrons. Another error on the emittance measurement is the finite number of electrons per camera pixel to measure the rms beam width on the spectrometer screen. A simple calculus can be done to estimate the statistical error introduced by the finite electron number. A beam charge of 5 pC corresonds to a total number of 30×10^6 electrons. For the emittance retrieval only a fraction of 3 % of the full spectrum is considered, which corresponds to only 1×10^6 electrons. The fraction of the camera images that is extracted to measure the rms beam width is on the order of 50×100 pixels large. Thus only 200 electrons per pixel on avarage are detected by the spectrometer cameras. However, the electron distribution in the spectrometer screen plane is not homogeniously distributed as shown earlier. A better estimation of the statistical error per camera pixel count is the formula

$$s_c = \sqrt{\frac{c \sum c}{N_e}}, \tag{4.18}$$

where c is the single pixel count, $\sum c$ is the sum of all pixel counts, and N_e is the number of electrons that where detected on the spectrometer screen, which can roughly be approximated to be half of the number of electrons detected in the second cavity BPM.

Figure 4.11 shows the counts per pixel for a lineout in the non-dispersive axis of a simulated 5 pC beam. The relative statistical error in pixel counts by equation 4.18 due to the finite number of electrons per pixel is in the order of 3 % at the beam center and increasing rapidly towards the wings of the beam profile. The statistical error per pixel is considered in the emittance retrieval algorithm and Gaussian error propagated to the

rms width calculation and also considered for the emittance fit. An error of 1 % by the finite electron number onto the reconstructed emittance was found via simulations.

Camera Noise. Similar to the statistical error in pixel counts also the camera noise introduces an error in rms width detection. In particular random count noise far away from the beam profile center increases the calculated rms width. In order to reduce the influence of camera noise onto the rms width detection the rms width is calculated 3 times iteratively and the signal outside 99.9 % of the core distribution (approx. 3.29 rms) is cropped to zero after each iteration. The signal to noise ratio of the spectrometer cameras observed in the experiment is in the order of 600. Simulations show a statistical error on the reconstructed emittance by 1 %.

4.3.6. Conclusion on Accuracy Study

The statistical and systemeatic error discused above are summarized in table 4.1. The parameter values are either estimated (see chapter 3) or experimentally determined (see chapter 6). For some of the listed parameters the resulting relative error in reconstructed beam properties is stated to be negligible. This means that the influence of the particular parameter is on the single-permille-level and too small to be covered by simulations. The list of error sources in table 4.1 is far from being complete in terms of accuracy studies performed for the emittance resolution estimation. Note that the errors introduced by the quadrupole focusing can be understood as systematical errors, since the accuracy of the beam optics model is the same for each quadrupole setting and in particular for every shot.

The errors introduced by the source beam properties and the camera noise represent both, a systematic and a statistical contribution to the emittance measurement accuracy. The greatest impact on the emittance retrieval is given by the initial beam pointing in the vertical axis. Here the average pointing detected during the data acquisition is a constant, thus systematic error in measurement of the average emittance. The shot-to-shot fluctuation in vertical beam pointing on the other hand results an inaccuracy in emittance on a single-shot bases. Further, the beam pointing averaged of a finite amount of time, e.g. averaged over 300 consequtive shots, can drift during the experiment, thus introducing an error on the rolling average emittance measured.

In order to estimate the total error in emittance measurement a series of 1000 Gaussian random distributed electron beams were simulated and the initial beam source properties were reconstructed from the generic spectrometer images. The simulated beam source properties were sampled from a normal distribution in order to simulate the observed parameter jitters in the experiment. The plasma target and quadrupole magnets were assumed to be on-axis. The total error in the reconstructed source beam properties is listed in table 4.2. The systematic error of -7 % and the single-shot error of ± 3.5 % in

Table 4.1. – Table of errors in reconstructed source beam properties. The values of the parameters were obtained from experiments or were estimated. Reconstruction errors on the single permille-level are considered negligible.

parameter	value	rel. reconstruction error (%)			
		$x_{\mathrm{rms},0}$	$x'_{\mathrm{rms},0}$	$\langle x\,x'\rangle_0$	ε_0
source beam properties					
$\langle x\rangle_0$	$(0 \pm 5)\,\mu\mathrm{m}$	negligible			
$\langle y\rangle_0$	$(0 \pm 5)\,\mu\mathrm{m}$	negligible			
$\langle x'\rangle_0$	$(0.0 \pm 0.5)\,\mathrm{mrad}$	0	$0^{+0.2}_{-0}$	0	$0^{+0.2}_{-0}$
$\langle y'\rangle_0$	$(-1.0 \pm 0.5)\,\mathrm{mrad}$	0	-6.6 ± 3.3	0	-6.6 ± 3.3
$y_{\mathrm{rms},0}$	$(0.8 \pm 0.4)\,\mathrm{mrad}$	0	0 ± 1	0	0 ± 1
$\Delta\langle z\rangle_0$	$(0 \pm 1)\,\mathrm{mm}$	negligible			
N_e	1×10^6	0 ± 1	0.0 ± 0.1	0	0 ± 1
quadrupole calibration and alignment					
g_{Q1} , g_{Q2}	$(0 \pm 30)\,\mathrm{mT/m}$	negligible			
x_{Q1}	$(0 \pm 5)\,\mu\mathrm{m}$	negligible			
x_{Q2}	$(0 \pm 10)\,\mu\mathrm{m}$	negligible			
y_{Q1}	$(0 \pm 10)\,\mu\mathrm{m}$	$0^{+0.5}_{-0}$	0	0.0 ± 0.2	0.0 ± 0.2
y_{Q2}	$(0 \pm 30)\,\mu\mathrm{m}$	$0^{+1.5}_{-0}$	0	0.0 ± 0.5	0.0 ± 0.5
analysis					
cam noise	0 ± 3 counts	negligible			
F	$(0 \pm 1)\,\mathrm{MeV}$	0^{+3}_{-0}	0.0 ± 0.5	0 ± 1	0 ± 2
E	$(0.0 \pm 0.3)\,\mathrm{MeV}$	0^{+1}_{-0}	0.0 ± 0.1	0.0 ± 0.3	0.0 ± 0.5

Table 4.2. – Total error in emittance, beam size, divergence and correlation measurement. The error does not include transverse misalignments between electron source and the quadrupole magnets.

	systematic	statistical
emittance	−7 %	±3.5 %
divergence	−7 %	±3.5 %
beam size	0 %	1.1 %
correlation	0 µm mrad	0.3 µm mrad

emittance and divergence measurement are dominated by the inital beam pointing in the dispersive axis.

As shown in figure 4.9 and table 4.1, also the transverse alignment between electron beam source and quadrupole doublet must be accurate in order to keep the error in emittance measurement at a reasonable level. At LUX, it was possible to align the plasma target and the quadrupole magnets relative within a precision of ±30 µm using beam based alignment. The alignment procedure and the nessecary diagnostics calibrations are discussed in the following chapter.

5. Beam-Based Quadrupole and Target Alignment

The quadrupole magnets and the electron source are important to be aligned relative to each other in order to minimze the dispersion of the electron beam during the transport to the spectrometer. If the magnetic axes of the quadrupole magnets (the axes where the field inside the quadrupole magnet is zero) is offset to the beam, the electrons experience an additional dipole field ΔB inside the quadrupole and are steered and dispersed.

Prior to the installation of the quadrupole doublet into the electron beamline, the center of the geometric aperture was referenced to four alignment-marks attached to the magnet yoke using a laser tracking device [99]. The doublet was then mounted onto a specially designed alignment table, allowing to position the second quadrupole with respect to the first one. The alignment table and the doublet, together as a single device, are then installed behind the target chamber and alligned to the coordinate system of the accelerator tunnel. With the laser tracking device, it was possible to align the geometrical axis with a precision of approximately 100 µm. However, the magnetic axis must not neccessarly coincide with the geometric axis. A misalignment of the extra pole tips, for example, can lead to a small but relevant shift of the magnetic axis. Further, the electron design axis, defined by the two BPMs, is referenced to the tunnel coordinate system with the same precision.

Thus, in total, the magnetic axes of the modified quadrupole magnets can deviate by a few hundred micrometers from the design axis. As derived in the previous chapter, a relative positioning of the quadrupole magnets with respect to the electron beam axis to a few ten micrometers is required to keep the error on the emittance introduced by beam dispersion at an acceptable level.

The alignment of the quadrupole magnet to the electron axis can be measured by detecting the offset of the electron beam on a profile screen caused by the dipole kick inside the quadrupole field. There are in general two different methods available at LUX for the beam based alignment. Either the beam is focused by both quadrupole magnets onto the profile screen, therefore resulting in a focus spot. Or, only a single quadrupole magnet is used at a time, thus focusing the beam in one plane and defocusing it in the other, resulting in a line focus on screen. Both methods are in principle equivalent and have both been tested and delivered similar results. However, only the line foci

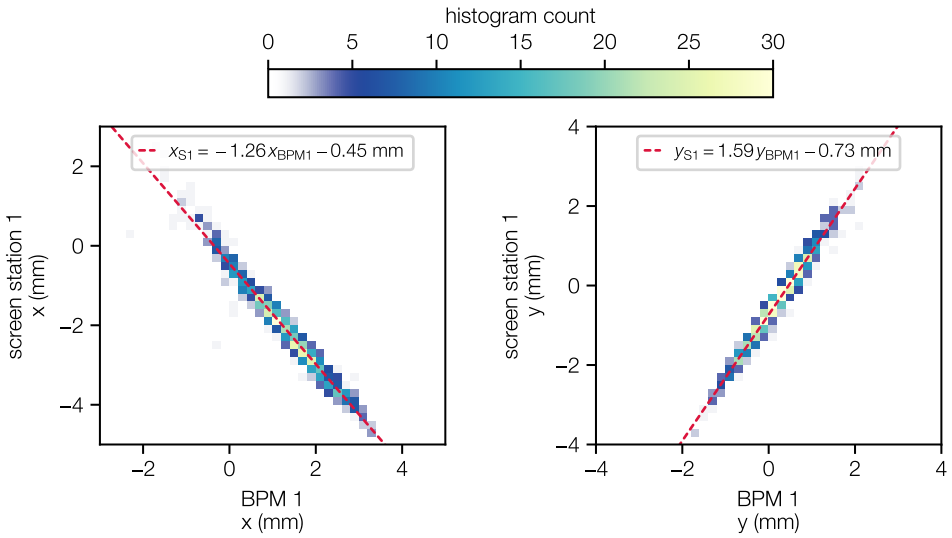

Figure 5.1. – Comparison between beam position measurement of first cavity beam position monitor (BPM1) and first profile screen station (S1). The electron beams were freely drifting over 3 m into the diagnostics.

measurements are discussed in the following, since the line foci were found to deliver more robust results and are less complex to be analysed, since the offsets can be identified to a single quadrupole magnet. The line foci measurements and the analysis were done together with B. Hubert [100].

5.1. BPM - Profile Screen - Calibration

Before a beam-based alignment of the quadrupole magnets, the position on the profile screen was calibrated to the electron design axis, respectively to the cavity beam position monitor (BPM1) zero-reading. 1000 consecutive shots of unfocused electron beams freely diverging to the scintillator were recorded, therefore also passing the upstream BPM1. The raw images of the screen were post-processed and the beams center of charge was calculated and compared to the BPM1 position reading. The correlations in x and y position measured by both detectors are plotted in figure 5.1. The plot shows the mm-calibrated beam position on the scintillator screen and the raw data of the BPM read out electronic. The BPM read-out electronic was pre-calibrated by the manufacturer and re-calibrated after the installation in the tunnel including an impedance measurement of the RF-cabling between the resonator and the read-out electronics. The BPM position reading is zero if the beam passes the BPM on the center axis, which is independent of any calibration. Therefore, the BPM zero-reading is used to reference the absolute screen position to the electron-design axis, respectively the tunnel-coordinate system. Note that

only the chamber of the profile screen stations were positioned in the tunnel-coordinate system and not the screen itself. The screen can therefore be displaced in the tunnel coordinate system by ±1 mm. The mm-per-pixel calibration of the profile screen can be determined accurately with a calibration target. Therefore, the slope of the correlation in position reading in figure 5.1 is used to post-calibrate the BPM reading to an actual mm-scale.

The calibration factors of −1.26 for the horizontal and 1.59 for the vertical axis for the first BPM have to be multiplied to the raw read-out electronic values. The profile screen mm-scales have to be shifted accordingly by −0.45 mm and −0.73 mm from the screen center in the horizontal and vertical axis, respectively.

These numbers were used for the subsequent beam-based alignement of the quadrupole magnets and the plasma target. However, the beam position detection on the scintillator screen is limited by the signal-to-noise ratio as discussed in section 5.4.

5.2. Line Foci and Quadrupole Offsets

With the profile screens being referenced to the tunnel design axis, the absolute beam position on screen can be detected. In order to measure the relative transverse alignment of the quadrupole magnets and the electron source, the electron beams are focused by each quadrupole individually and with both possible quadrupole field polarizations each. The resulting line foci on the profile screen are depicted in figure 5.2. The images in the upper row show the line foci generated by focusing the beam with the first quadrupole magnet Q_1. The bottom row shows the line foci focused by the second magnet Q_2. In the left column, the electron beam was focused in the vertical y-axis. By focusing the beam with the first quadrupole Q_1, the beam had to be steered back on screen with the second corrector dipole C_2. This hints for a larger offset of the first quadrupole magnet to the electron beam in the vertical axis. The right column shows the line foci obtained from focusing the beam in the horizontal axis. Here, both magnets do not seem to be diplaced by large amount from the electron axis.

The images in figure 5.2 were summed over 100 consecutive shots. The recorded line foci are projected onto the non-focused axis and the peak-position of the projection is determined. The measured line-foci peak-positions for both magnets and both field polarizations enable to reconstruct the horizontal and vertical offset of both magnets from the electron axis.

The transverse displacement between the quadrupole magnet and the electron beam can theoretically be expressed by an operator $\mathcal{T}$ that simply switches the coordinate system between the electron beam design axis and the quadrupole system.

$$\mathcal{T}_i : x \longmapsto x - x_{\mathrm{Qi}}, \qquad \mathcal{T}_i^{-1} : x \longmapsto x + x_{\mathrm{Qi}} \quad , \tag{5.1}$$

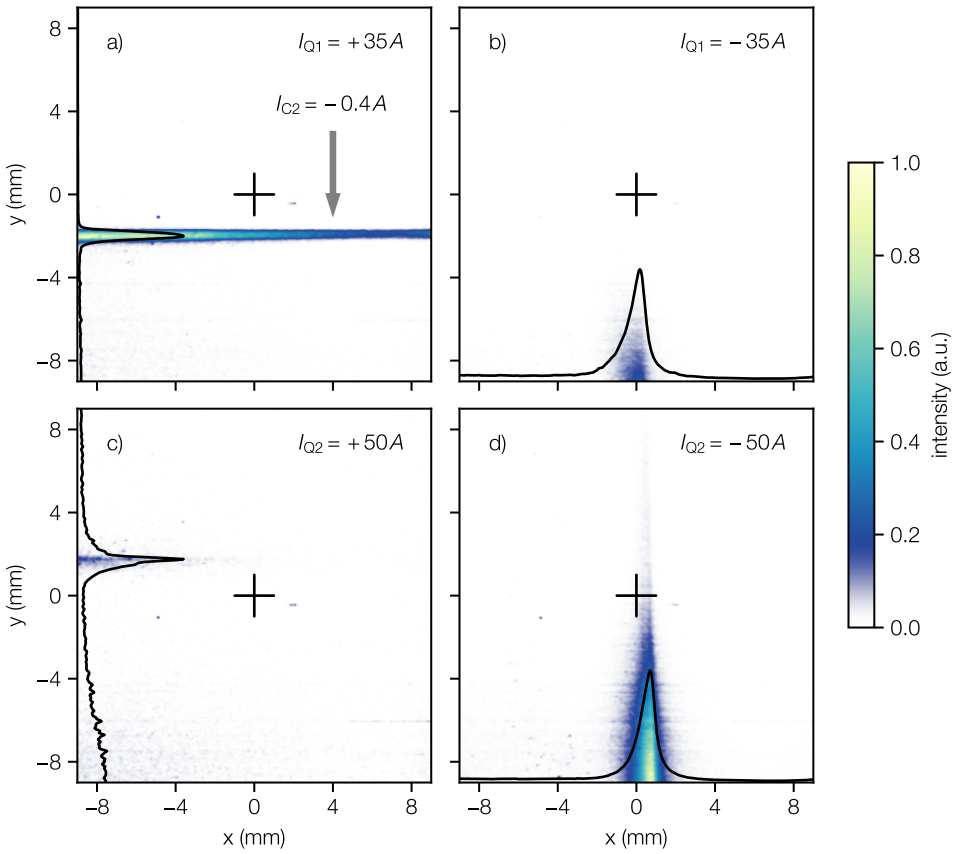

Figure 5.2. – Line foci at screen station 1 before quadrupole alignment. a) Focusing with only Q_1 in positive polarization. Corrector C_2 was used to steer the beam back on screen. b) Focusing with Q_1 in negative polarization. c) and d) Focusing with only Q_2 accordingly.

where x_{Qi} is the horizontal offset of the ith quadrupole magnet and the initial electron axis, i being either 1 or 2. The equation system that needs to be solved for each quadrupole individually is

$$\begin{pmatrix} x \\ x' \end{pmatrix} = M_{\mathrm{d1}}\, \mathcal{T}^{-1}\, M_{\mathrm{Qi}}^{\pm}\, \mathcal{T}\, M_{\mathrm{d0}} \begin{pmatrix} x_0 \\ x'_0 \end{pmatrix}. \tag{5.2}$$

Here, $M_{Qi}^{\pm}$ is the transport matrix for the ith quadrupole magnet for positive (+) or negative (−) field polarization. M_{d0} is the matrix expressing the free drift from the electron source to the ith magnet. M_{d1} is the matrix expressing the drift from the ith magnet to the scintillator screen. The same equation and operator $\mathcal{T}$ can be defined equivalently for the vertical y-axis. In case of the first quadrupole Q_1 focusing the beam in the vertical axis (see figure 5.2a), the matrix M_{d1} in the product in equation 5.2 has to be replaced by a sequence $M_{d2}\, M_{C2}\, M_{d1}$, where M_{d1} and M_{d2} again are drift matrices and M_{C2} is the transprot matrix for the second corrector dipole C_2.

The initial average beam pointing x'_0 and y'_0 are measured from unfocused electron beams on the profile screen as shown in figure 5.1. Only the first row in equation system 5.2 expressing the beam position on screen in the horizontal x, respectively in the vertical y-axis, is of interest. The remaining set of four equations is used to numerically calculate both quadrupole magents' offsets to the electron axis in both transverse axis. The results are listed in table 5.1.

The measured data does not allow for an absolute position determination of the electron source and quadrupole magnets in the tunnel coordinate system. Only relative transverse displacements of the quadrupole magnets from the electron source can be measured. The largest measured offset is a displacement of the first quadrupole magnet of 370 µm in the vertical axis.

A manual repositioning of the first quadrupole magnet is challenging, since the first quadrupole magnet is mounted directly to the adapter plate with no adjustment possibility. Therefore only the doublet as a whole can be translated and the second magnet then be aligned relative to the first magnet in a second step. However, loosening the locking screws of any of the adjustment tables comes with a risk of translating or rotating the magnet in an unintended way. Therefore, it was decided to only lift the second magnet such that both magnets are at the same height.

The second quadrupole magnet was translated manually. The initial position was referenced with three digital micrometer screws (two touching the magnet at the top and one at the side). This at least allowed to measure the magnets translation in the transverse axis as well as a possible rotation around the beam axis (skew angle). Other possible rotations or translation of the magnet were not monitored during alignment. Figure 5.3 shows a picture of the setup. The magnet was shifted as carefully as possible in order to not worsen the alignment. After shifting the magnet by $\sim$ 200 µm in the vertical

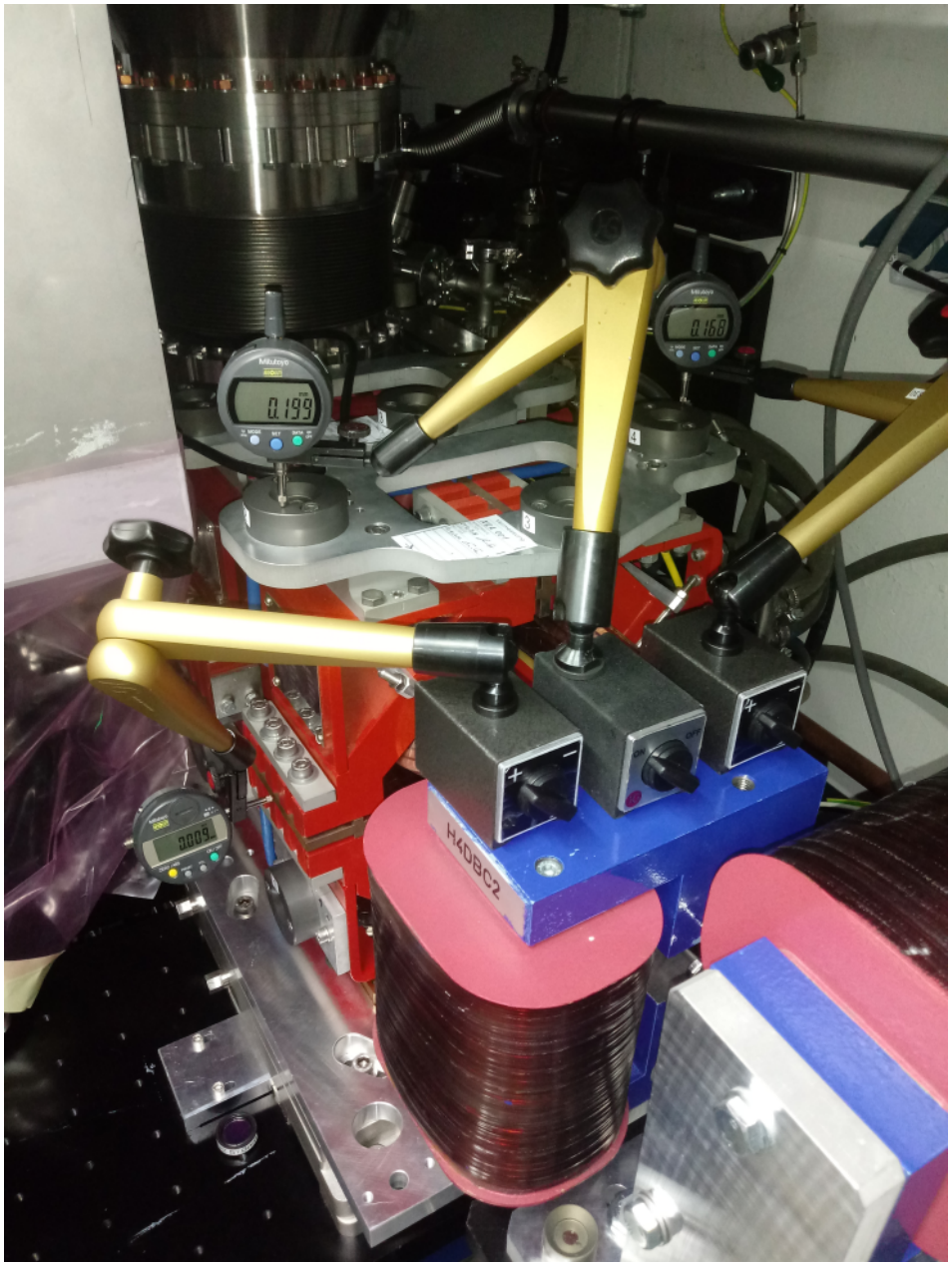

Figure 5.3. – Manual positioning of the second quadrupole magnet relative to the first. Three digital micrometer screws were used to monitore the quadrupole translation.

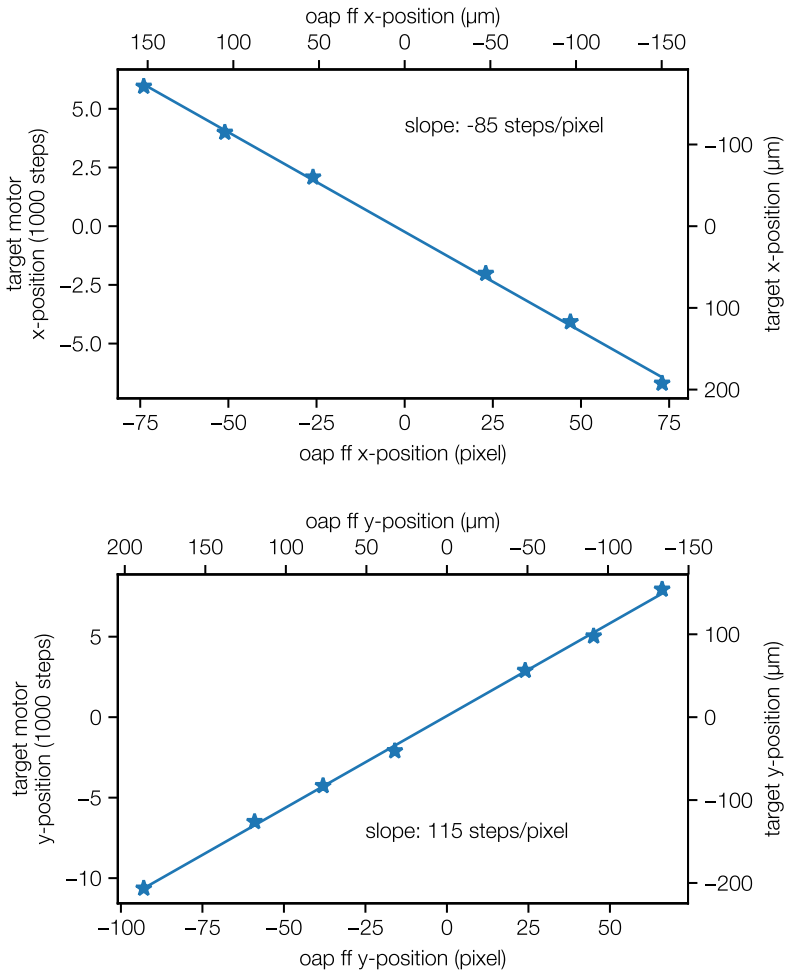

Figure 5.4. – Target position versus in-vacuum laser focus position, respectively incoupling laser far field calibration.

axis with an accuracy of 30 µm, which is also the precision in the beam-based alignment measurement, the magnet was considered to be aligned. Only a translation of the magnet in the vertical axis was possible. In the horizontal axis, the adjustment mechanism was already at its limit.

5.3. Beam-Based Target Alignment

After alignment of the second quadrupole magnet relative to the first, the electron source and thus the plasma target and the laser focus had to be aligned to the quadrupole doublet. The target mover motor positions were calibrated to the in-vacuum laser focus position, which was referenced to the laser near- and far-field on the incoupling parabolic

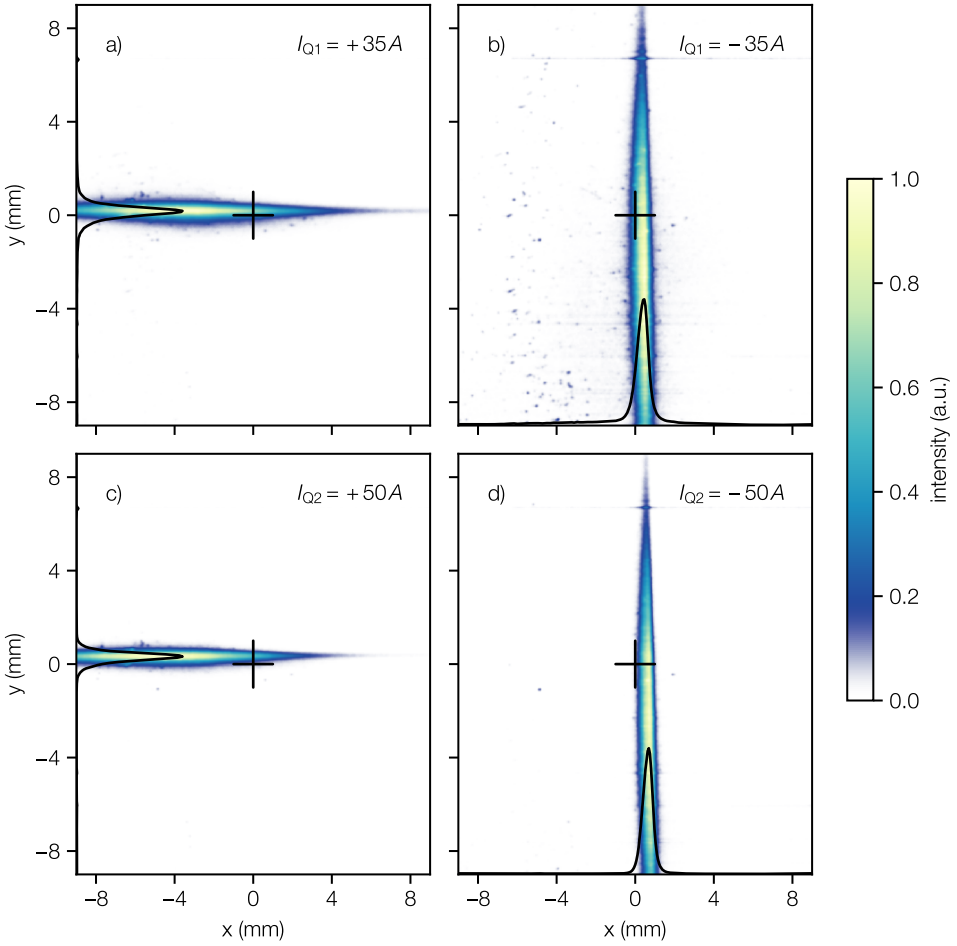

Figure 5.5. – Line foci of the electron beam on profile screen 1 after the alignement of the quadrupole magnets and the electron source. All corrector dipoles were off.

mirror. The calibration data is plotted in figure 5.4. The laser focus and plasma target were simultaniously translated online in order to directly see the electron beam shifting on the scintillator screen. Herefore, the electron beam was focused by both quadrupole magnets such that the plasma target position was optimized effectively relative to both quadrupole magnets.

Afterwards, line foci with both field polarizations and each magnet were taken again in order to quantify the relative alignment between quadrupole magnets and the new target position. The respective profile screen images are shown in figure 5.5. All line foci are close to the calibrated screen center (indicated by the black cross). No corrector dipoles had to be used. The remaining offsets of the line foci in the focused axis are due to a remaining misalignment between the two quadrupole magnets on the 30 µm level. The offsets in the defocused axis are due to an electron mean pointing from the source into

Table 5.1. – Measured quadrupole magnet displacements from the electron source before and after alignment.

measurement	x_{Q1} [µm]	x_{Q2} [µm]	y_{Q1} [µm]	y_{Q2} [µm]
before alignment	−7	42	371	165
	$\Delta x_{12} = 49$		$\Delta y_{12} = 206$	
	precision ±30			
after alignment	3	38	6	32
	$\Delta x_{12} = 32$		$\Delta y_{12} = 28$	
	precision ±30			

the quadrupole magnets. The measured relative offsets between the quadrupole magnets and the electron source after alignment are listed in table 5.1.

Finally the new laser focus position was referenced to the laser far-field position on the incoupling parabola and saved for subsequent beam times. The remaining offset between the quadrupole magnets was considered to be acceptable. Further improvement of the alignment would only be possible with a more reliable diagnostics and alignment procedure.

5.4. Profile Screen Detection Limits

As mentioned above, the detection of the beam position on the profile screen is limited in accuracy. In particular, the position reading of the BPM and from the profile screen can deviate between experiments. The main reason is a too small signal to noise ratio in the profile screen images. The scintillator screen was specially shielded against laser light and white light emitted from the plasma. However, an increase in background light is clearly seen when the laser is send to the experiment. Additionally, the camera optic was designed to have a high spatial resolution of a few µm, which comes with the expense of a reduced photon yield per pixel.

In order to detect the beam profile on screen, the camera signal below a certain value above the camera noise is croped to zero. This can also lead to a loss in beam signal, in particular in the wings of the electron profile. The correlation between total signal on the profile screen and total charge measured by the BPM1 is plotted in figure 5.6. The data was taken in a dedicated run. Two times 1000 consecutive shots were detected. In order to study the influence of the laser onto the electron pointing, the laser wavefront into the compressor was changed inbetween with a deformable mirror [64]. Only the 0°-astigmatism and the 45°-astigmatism of the laser wavefront were changed by $-0.05\,\mu m$

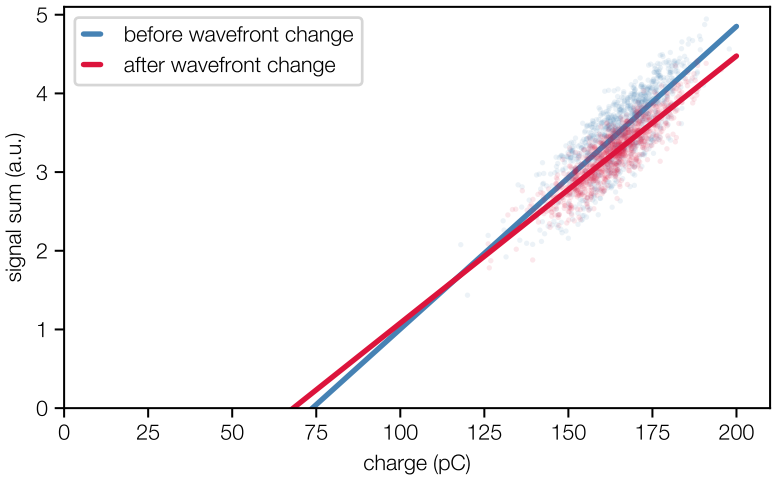

Figure 5.6. – Correlation of total profile screen count and BPM1 charge and linear fit before and after changing the laser wavefront into the compressor. Only half of the total charge is detected by the profile screen station.

and 0.03 µm, respectively. The amount in wavefront change is within the fluctuation of the daily laser optimization procedure. The total count and charge for each single shot is plotted in dots in figure 5.6. A linear fit was applied to each data set and extrapolated towards the zero count reading of the profile screen (line). The wavefront change influences the slope of the fit. For this dedicated run the electron charge was 150 pC to 175 pC. The fit lines are crossing zero at around 70 pC to 75 pC. Therefore, almost only half of the beam charge is detected by the profile screen station.

Figure 5.7 shows the correlation in beam position detected by the BPM1 and by the first screen station. Figure 5.7a exemplary shows a single shot transverse beam profile as seen on the screen station prior to changing the wavefront. The recorded beam profile is elliptically symmetric. An arbitrary 2d-Gauss is fit to the image. Contours at 1 sigma (solid ellipse) and 2 sigma (dashed ellipse) of the 2d-Gauss are superimposed to the beam profile. The projection onto the tunnel axis of the measured beam profile (blue) and the 2d-Gaussian fit (black) are added to the plot axes. The weighted mean positions of the measured and fitted projection are plotted as a cross. For comparison, the beam position detected by the BPM1 is indicated with a red dot. Figure 5.7b shows an example image of an electron beam after changing the wavefront. A halo in the electron profile pointing in the positive x-direction can be seen. The weighted mean of the measured and fit projection still detect the core beam profile. The position by the BPM deviates and is pointed towards greater x-values. The rolling average over 20 shots of the horizontal beam pointing detected by the screen station and the BPM is plotted in figure 5.7c. Before changing the wavefront the average beam position by both diagnostics coincide. After changing the wavefront the rolling averages deviate by around 300 µm.

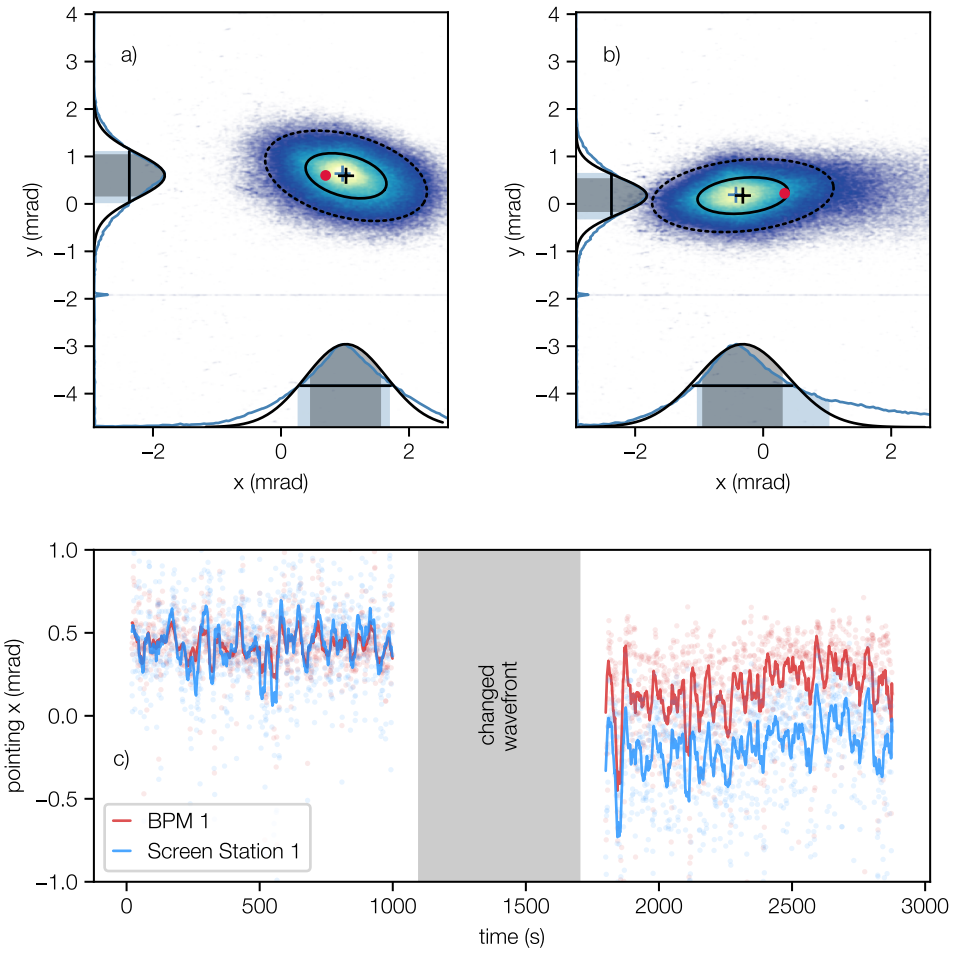

Figure 5.7. – Correlation in beam position detection by the profile screen station and the BPM before and after a wavefront change. The beam profile on screen is symmetric before (a) and asymmetric after (b). changing the wavefront. Also the average horizontal beam position deviates after the wavefront change (c).

This shows that due to small changes in the laser properties and due to the poor signal-to-noise ratio of the profile screen diagnostics the position calibration between the profile screen and the BPM can deviate on a daily basis. Further improvement of the alignment between electron source and the quadrupole magnets therefore also requires an improvement in the electron profile screen diagnostics. An upgraded profile screen at LUX is currently designed but will only be available for future experiments.

In summary, the beam-based alignment between the beam optics and the electron source at the current LUX setup is limited in precision. However, an alignment between electron source and both quadrupole magnets on the 30 µm level has been achieved. The remaining error on the measurement of the emittance is below 1 % (see chapter 4.3.3).

6. Imaging and Emittance Measurements

The experimental results from the emittance measurement campaign in March 2019 at LUX are presented in this chapter. A short summary on the laser and plasma parameters as well as a description of the data acquisition during the scans is given in section 6.1. The detected electron beam properties from single shots and the beam stability are discussed in section 6.2. Before the quadrupole scan, the imaging quality by the beam optics was experimentally determined, which is presented in section 6.3. After a comparison between single-shot and quadrupole-scan emittance measurements in a narrow energy interval, presented in section 6.5, the phase-space properties at different energies in the spectrum are discussed in section 6.6. With the quadrupole-scan data a first direct measurement of the chromatic effects imprinted by the transport optics is shown in section 6.7.

6.1. Experimental Parameters and Data Acquisition

As described in chapter 2.2 the last amplifier stage of the driver laser was not available during experiments presented in this chapter. The laser power was therefore limited to 1.4 J into the in-vacuum compressor and the remaining laser power on target was limited to 0.88 J.

The target inlet pressure was increased to a comparably high value of 81.4 mbar in order to reach the high plasma density of $4.8 \times 10^{18}\,\mathrm{cm}^{-3}$. Together with the self-focusing [101] of the laser in the plasma, the laser intensity was still high enough to inject and accelerate electrons. The pressure and the corresponding gas flow rate were close to the limit of the evacuation capacity of the differential pumping system. Though electron beam generation was possible, only little margin in laser and gas density parameters was left for optimization, respectively for online compensation of e.g. a laser wavefront degradation [65].

In fact, a continous electron beam quality degradation in terms of a reduction in beam energy and pointing stability was observed after 10 min to 15 min after unblocking the laser beam. The degradation was identified to be caused by heating of the laser optics. After blocking the laser for 1 min to 2 min, the original electron beam quality was recovered. Therefore, it was decided to limit the consecutive data acquisition to time windows of 5 min and to attenuate the laser intermediately for 90 s to the 1 mJ-level

before the compressor. While the laser was attenuated, the quadrupole magnet currents were ramped and fine adjusted for the next scan step. With this procedure, stable electron acceleration over many hours was achieved. Due to the low laser energy, electron generation with 5 Hz repititon rate was possible and thus a significant amount of data could still be acquired at each scan step, i.e. 300 consecutive shots.

In order to exclude drifts in the experiment during the focusing scans, the scan ranges were always scanned twice. The scans were performed such that the quadrupole field gradients were always increased for the next scan point, in order to account for the hysteresis [102] of the magnets. After the first half scan, the quadrupole magnets were demagnetized and again ramped from smaller to larger field gradients for the second half of the scan, filling the intermediate steps of the first. With this, it was ensured that the changes observed in the experiment were caused by varying the quadrupole focusing and not another parameter drifting.

6.2. Electron Beam Characterization

In the following, the electron beam properties measured from single shots and the beam stability are discussed. In particular, for a multi-shot quadrupole-scan reproducable electron beams are required. In order to characterize the electron beams properties out of the plasma as well as after the beamline transmission both unfocused and focused electron beams were recorded.

For example, the beam charge, pointing, and energy spectrum out of the plasma can not be measured directly when the electron beam is focused by the doublet. Due to the chromatic focusing, the low energy electrons are lost and only a fraction of the total charge is transmitted through the beamline. The pointing of the electron beam will mainly be translated into an offset from the design axis by the doublet. Due to additional dispersion in the quadrupole magnets, the BPM position reading is also influenced by the energy spectrum. Since charge is also lost between the BPMs, the original electron beam direction can not be reconstructed reliably. In particular, the vertical beam pointing can not be measured online in case of focused electron beams.

6.2.1. Unfocused Electron Beams

A series of 6×300 consecutive shots of unfocused electron beams has been recorded in order to measure the electron spectrum, beam charge and beam pointing out of the target. The laser was attenuated intermediately for the unfocussed beams in order to model the electron beam energy and pointing stability during the scans.

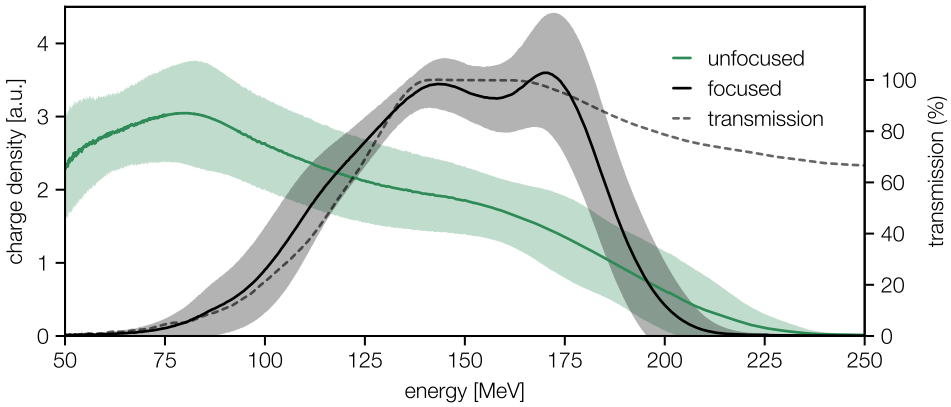

Figure 6.1. – Average energy spectrum of unfocused and focused electron beams. The filled area denotes 1 standard deviation of the observed spectral jitter. Low energy electrons are lost when focusing the beam due to the transmission function of the beamline.

Energy Spectrum and Charge. Figure 6.1 shows the average electron spectrum observed from unfocused shots on the spectrometer screen. The filled area denotes one standard deviation of the observed charge density jitter. Due to the low laser energy, the maximum generated electron energy was 200 MeV. The generated electron spectra were broadband. The broad energy spectra qualitively fit the PIC simulated longitudinal phase-space as described in chapter 2.4 and plotted in figure 2.7. In contrast to other experiments with higher laser energy, no significant peak is observable in the unfocused energy spectra. The beam charge measured in the first BPM was 20 pC (see figure 6.2).

Beam Pointing. The single-shot electron beam pointing was measured with the BPM during the same run and is plotted in figure 6.2b. The electron beams from the plasma were pointing on average by -0.7 mrad in the horizontal and -1 mrad in the vertical direction. The shot-to-shot fluctuation in beam direction was ± 0.4 mrad and ± 0.5 mrad, respectively.

The average pointing and pointing jitter in the vertical axis introduce a systematical and statistical error of $-7\,\%$ and $\pm 3\,\%$ in the emittance reconstruction as described in section 4.3.4.

6.2.2. Focused Electron Beams

In the following the electron beam properties observed from focused beams are discussed. The analysed data shown in this section is the data measured during the quadrupole scan presented in section 6.5. The single shot properties are analysed in order to quantify the beam stability.

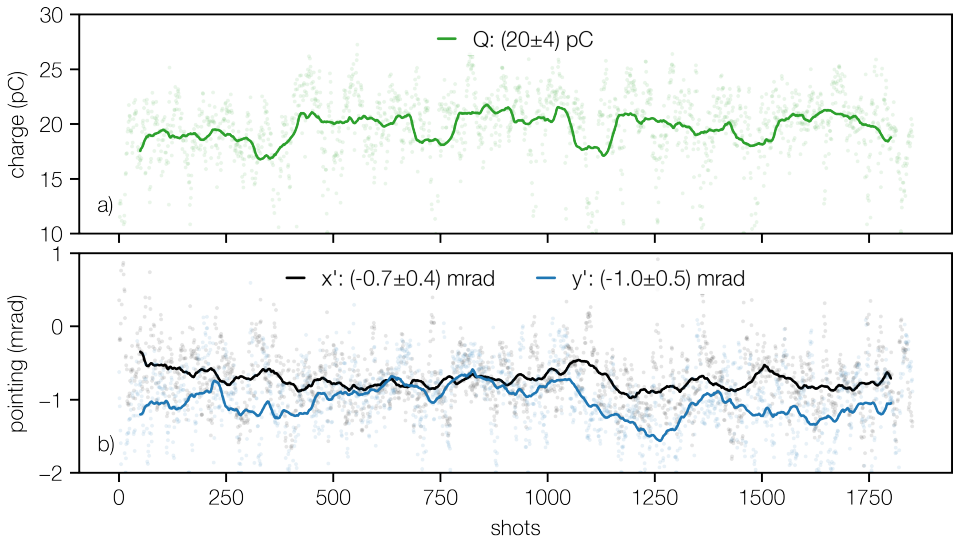

Figure 6.2. – Electron beam charge and pointing from the plasma target. The single shot beam charge (a) and position (b) is detected by the first BPM and plotted as single dots. The lines show the rolling average over 100 shots.

Transmitted Energy Spectrum. The average transmitted electron spectrum of focused electron beams is plotted in figure 6.1. The quadrupole magnets were set to focus a beam energy of 150 MeV onto the spectrometer screen in both axes. The measured peak charge density exceeds the charge density of unfocused electron beams at the focused energy, since the unfocused beam profiles are croped in the non-dispersive axis due to the finite screen width and diverged beam size. The beamline transmission is 100 % for beam energies close to the focused energy by the quadrupole doublet. Due to the chromatic focusing by the quadrupole magnets, the low energy electron beams are lost during beam transport. Electron energies below 75 MeV cannot be detected. In contrast to the unfocused spectra, the average focused energy spectrum shows a small peak at 175 MeV.

Beam Profiles. Figure 6.3 exemplarily shows the beam profile of six consecutive electron beams focused onto the spectrometer screen. The transmitted charge per energy is rather constant for the plotted shots. The shearing angle θ_s (see figure 4.5) of the beam profiles fluctuates from shot-to-shot indicating a fluctuation in initial horizontal beam pointing. The rms beam size is calculated for each energy slice in an interval of ± 5 MeV around the focused energy of 153 MeV and plotted separately in the right column of figure 6.3 for each single shot. The detected focused energy - the minimum beam size position in the energy axis - is also varying between consecutive shots. This is due to a change of the virtual source position, respectively a change in the beams phase-space correlation after the plasma, on a single shot basis.

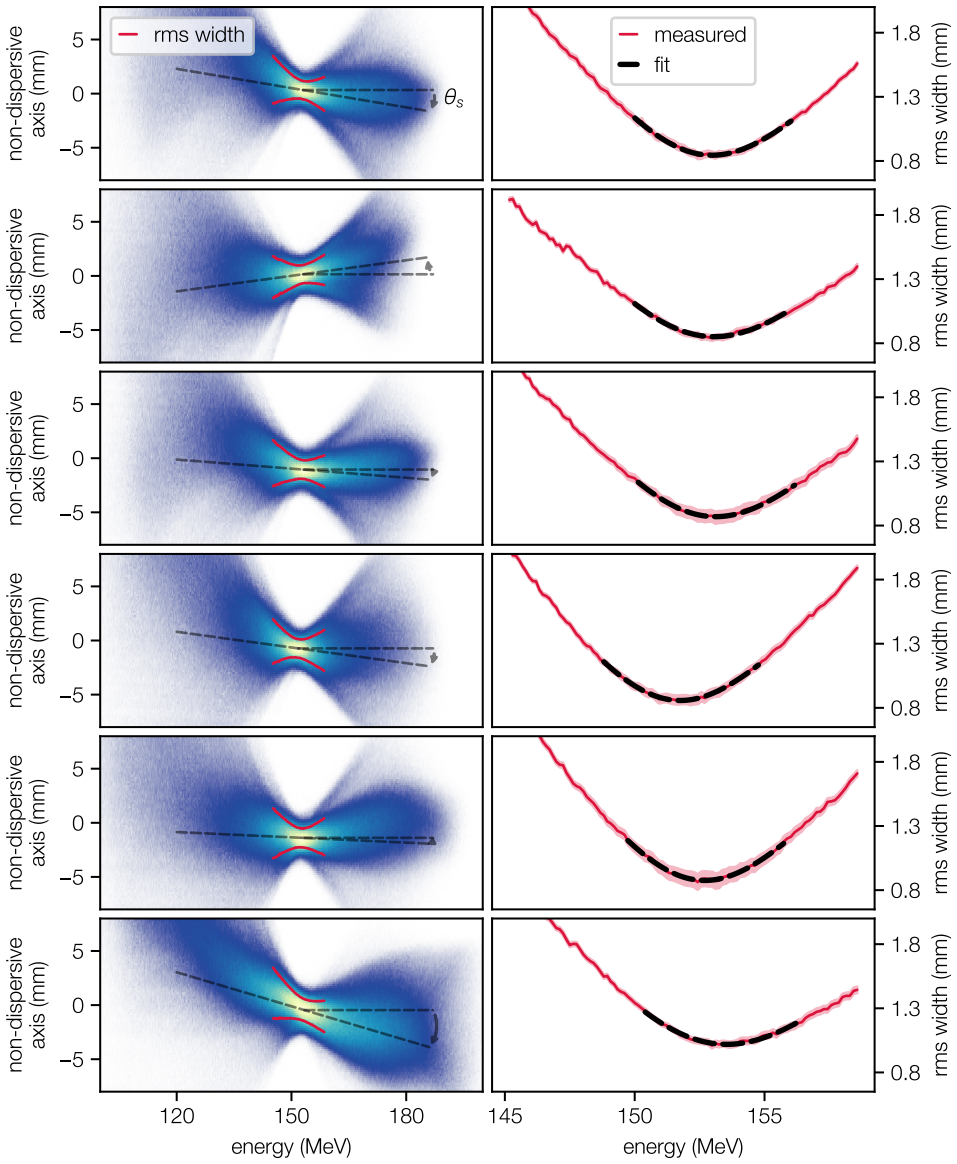

Figure 6.3. – Beam profiles of focused electron beams on the spectrometer screen from six consecutive shots.

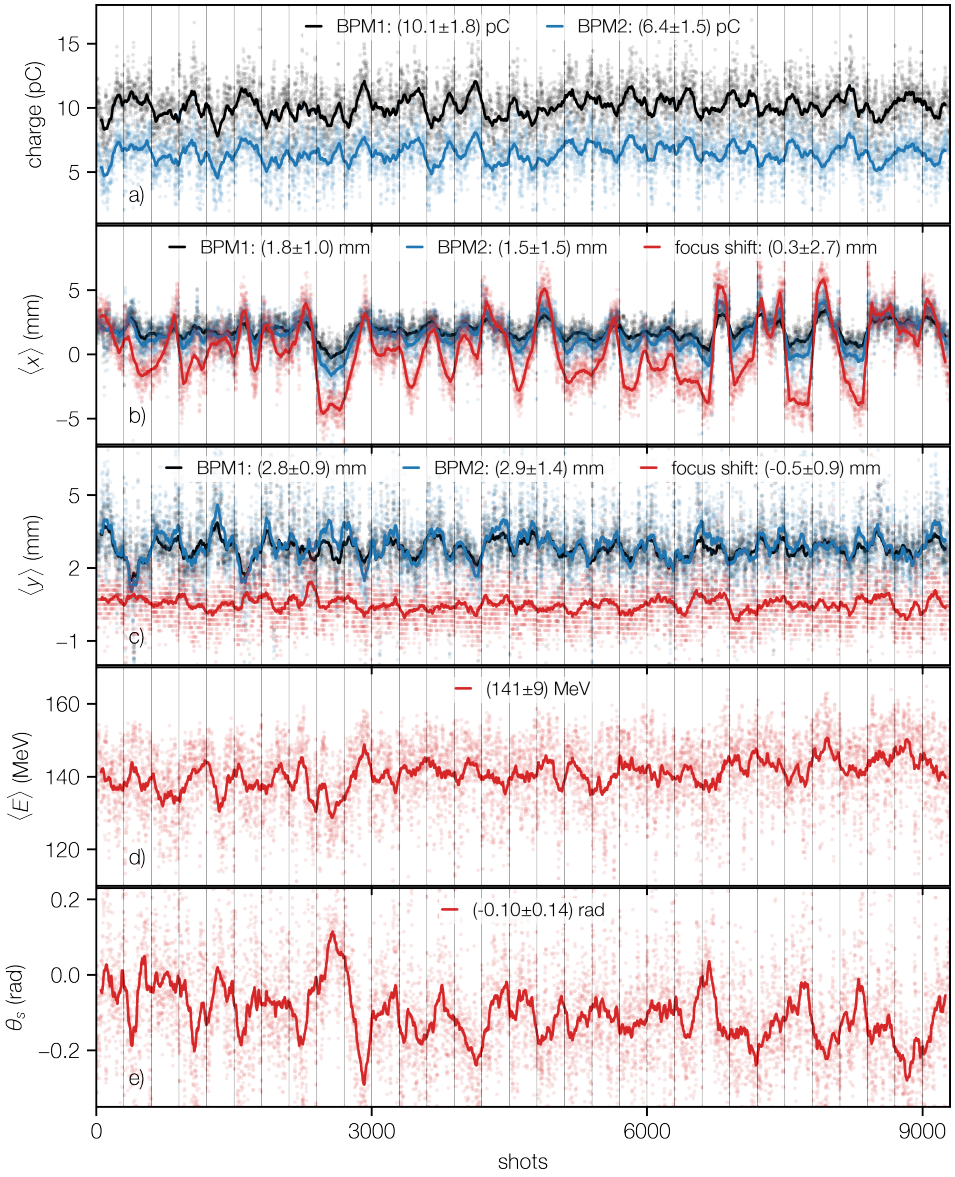

Figure 6.4. – Beam charge, position and pointing stability of focused beams. The single shot data is plotted as dots. The curves denote the rolling average over 100 shots. a) BPM Charge. Horizontal (b) and vertical (c) beam position in BPM and electron focus shift on the spectromter screen. d) Mean energy of the transmitted electron spectra. e) Shearing angle of the electron beam profiles on the spectrometer screen.

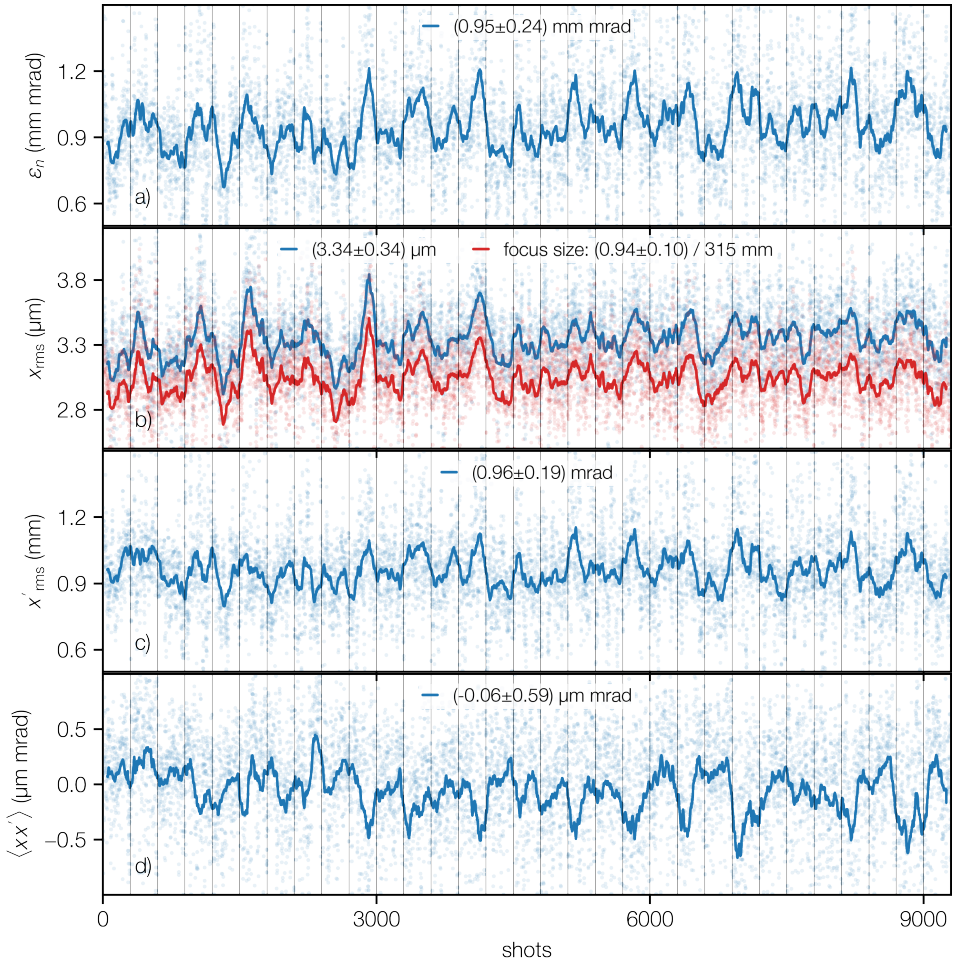

Figure 6.5. – Reconstructed horizontal electron beam phase-space at the virtual source from single shots. The single shot data is plotted as dots. The curves denote the rolling average over 100 shots. a) Reconstructed normalized emittance. b) Reconstructed source beam size and measured electron focus size on the spectrometer screen. Reconstructed beam divergence (c) and phase-space correlation at the source (d).

The single shot beam properties of a series of 31×300 consecutive shots is plotted in figures 6.4 and 6.5. Figure 6.4 summarizes the observed stability in electron beam position and beam pointing. Figure 6.5 summarizes the measured single-shot transverse phase-space properties. The vertical lines in the plots of both figures mark the moments where the data acquisition was interrupted and the laser attenuated. Note that the data plotted in figures 6.4 and 6.5 has not been filtered.

Transmitted Charge. The transmitted charge to the first BPM, with 10 pC on average, is plotted in figure 6.4a (black). Only half of the charge detected for unfocused electron beams is thus detected after focusing the electron beams. The measured charge in the second BPM with 6.4 pC on average is even less. The charge measured by both BPM is strongly correlated. This indicates that the generated spectral charge density is stable but only the low energy electrons are lost during beam transport.

Horizontal Beam Position. The horizontal position detected by both BPMs is plotted in figure 6.4b. In addition, the detected focus position in the horizontal axis, i.e. the non-dispersive axis, is plotted in red. All three curves show a similar trend and are correlated, too. The position reading by both BPMs almost coincides. The displacement of the electron beam from the mean axis is more pronounced in the BPM2 position reading. This is due to the BPM2 being located further behind the quadrupole magnets and the spectral transmission being more narrow. Therefore, the amount of low energy background electrons smearing out the position reading is less. The change in horizontal focus position is even stronger. This, on the one hand, is explained by the focus position on screen being detected for a single energy and, on the other hand, by the electron dipole defocusing the beam in the horizontal axis and thus magnifying the horizontal offset by a factor of ~ 2.

As can be seen, the horizontal focus position on the spectrometer screen is drifting strongly within a range of ± 3 mm. With the total magnification by the beam optics by a factor 315 this corresponds to a change in transverse electron source position on the ± 10 µm level, which is caused by the laser focus position in the plasma to drift by the same amount.

Vertical Beam Position. The vertical position detected by the two BPMs is plotted in figure 6.4c. The electron focus position in the vertical axis, i.e. the dispersive axis of the spectrometer, is added to the plot in red. The vertical beam position in the BPMs is drifting by a similar amount as the horizontal beam position, which is again attributed to a drift in the laser focus position into the plasma. The focus position on the spectrometer screen however is drifting significantly less. This is due to the spectrometer dipole focusing the beam in the dispersive axis and the total magnification factor by the beam optics being only 9.5.

Mean Transmitted Energy. Figure 6.4d shows the measured mean energy of the transmitted electron spectrum. The relative stability is 5 %. As described earlier, the

electron spectrum from the target is cropped by the energy dependent transmission function introduced by the focusing optics. The mean energy of the transmitted spectrum is partially correlating with the transmitted beam charge. The charge density of the transmitted spectrum is therefore reproducable.

Horizontal Pointing. The last row in figure 6.4 shows the measured shearing angle of the electron beam profile on the spectrometer screen. The observed mean shearing angle and jitter of (-0.10 ± 0.14) rad correspond to an initial horizontal electron beam pointing of (-0.5 ± 0.7) mrad. The average horizontal beam pointing measured from unfocused shots after the quadrupole scan and plotted in figure 6.2b was measured to be (-1.0 ± 0.7) mrad. The average beam pointing in the horizontal axis therfore worsened during the quadrupole scan, which can also be seen by the shearing angle θ_s decreasing towards negative values. The increase in electron pointing could be related to a residual heating of the laser optics.

The plots in figures 6.4 and 6.5 show the unfiltered single shot beam properties. For the quadrupole scan in section 6.5 only electron beams with a shearing angle $\theta_s < 0.1$ rad are considered, to keep the error onto the emittance measurement small (see section 4.3.4). Consequently only around half of the 300 detected electron beams per scan step are used for the comparison of the quadrupole-scan and the single-shot method.

The unfiltered reconstructed initial phase-space properties of the single shots are summarized in figure 6.5. The plotted values were obtained via the single-shot method as described in section 4.2.4.

Normalized Emittance. The retrieved normalized emittance is plotted in figure 6.5a. It is observed to be constant over the full dataset. Only a very small increase towards the end of the run is present in the data, which could be caused by either the increasing shearing angle of the electron beams or by a constant degredation of the laser wavefront.

Beam Size. The initial electron beam size reconstructed in the virtual plane imaged by the electron beam optics is plotted in figure 6.5b. In addition, the observed electron focus size on the spectrometer screen is plotted in red. Both curves follow the same trend and are correlated. This is expected since the focus of the electron beam on the spectrometer screen is a direct image of the initial spatial electron distribution. The remaining difference could be due to a remaining mismatch of the virtual electron source plane and the plane imaged by the quadrupole doublet. The plotted focus size is normalized by the horizontal magnifiaction factor of 315 by the beam optics. It does therefore not consider an initial phase-space correlation and is meant to illustrate a qualitative correlation of both plotted parameters.

Beam Divergence. The reconstructed beam divergence from the source is plotted in figure 6.5c. No long term change in reconstructed beam divergence and beam size were observed during the run. Note that the shot-to-shot fluctuation in measured beam

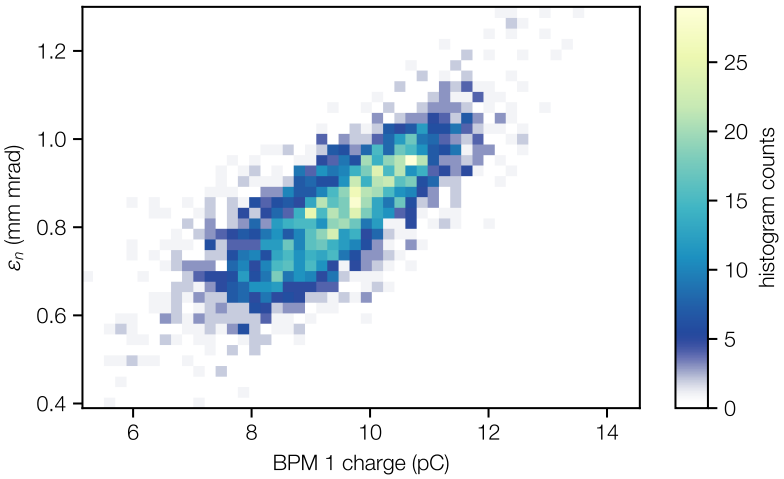

Figure 6.6. – Correlation between electron beam charge and normalized emittance. The data is displaced in a 2d-histogramm.

divergence is also influenced by the initial beam pointing in the vertical axis (see section 4.3.4).

Phase-Space Correlation. Figure 6.5d shows the reconstructed initial phase-space correlation at the virtual source plane imaged by the quadrupole doublet. The average phase-space correlation is close to 0. The residual correlation of $-0.06\,\mu\text{m}\,\text{mrad}$ indicates a mismatch between imaged and virtual source plane by a few $100\,\mu\text{m}$. Assuming that the measured phase-space correlation is a pure consequence of an electron source shift, the measured jitter corresponds to a shot-to-shot fluctuation of the virtual source plane of $\pm 1\,\text{mm}$. Note that a change in the virtual source position does not have to originate from a change of the real electron source position. It could also originate from a change or fluctuation of the phase-space modulation of the beam, for example by the plasma-to-vacuum transition.

In summary, the electron beam properties measured from single shots are observed to be stable within $\pm 20\,\%$ over the full run. The reproducability of the electron beams therefore supports the application of a multi-shot quadrupole-scan.

Lastly, the correlation between measured beam charge and normalized emittance is plotted in figure 6.6. A clear linear positive correlation is observed. The influence of space-charge effects [20] during the beam transport was excluded from simulations. The two quantities do not have to be directly correlated in terms of causality. It could also be a third quantity correlating with both quantities. It was observed that the total beam charge as well as the beam emittance both are dependent on the laser energy. Therefore, the change in both quantities could be caused by the change in laser intensity into the target. On the one hand, the higher the laser energy, the more charge is injected into

the beam. On the other hand, the more intense the laser, the larger the phase-space volume into which charge can be injected [103, 44]. This would also cause a larger beam emittance.

Note that the single-shot emittance was only measured from a small fraction of the spectrum, respectively from a small fraction of the full charge. The BPMs however measure the total beam charge ejected from the plasma and transmitted through the beamline. A final explanation of the observed mechanism cannot be given. Parameter studies with scans of the emittance dependence on the laser and plasma properties are required. Nevertheless, the high statistic taken during the experiment together with the long term stability of the generated electron beams at LUX allows for a complex analysis of the measured parameter space in the future [43].

6.3. Virtual Source Position Scan

The quadrupole magnet field gradients are set to image a virtual source in the target area onto the spectrometer screen. Idealy, the imaged plane coincides with the virtual source plane which denotes the electron source position in terms of free drift (see figure 4.3). As discussed in chapter 4.3.2, accurate imaging of the electron beam from the source to the spectrometer screen in both axes is crucial for the accuracy in initial phase-space reconstruction.

The virtual source plane of the electron beams can vary with respect to the plasma target position. The geometrically calibrated distance of the second gas inlet to the first quadrupole magnet is 110.8 mm. As shown in figure 2.5 the plasma density plateau region is well defined by the two inlets and the plasma density decreases rapidly from the second gas inlet to the end of the sapphire capillary. However, the electron phase-space can further be modulated by the tail of the density downramp at the target exit [40, 39]. Although the target position is referenced in the tunnel coordinate system, the virtual electron source plane can nevertheless vary on a daily basis and needs to be experimentally determined.

The phase-space correlation at the virtual source is 0 as per definition. Thus reconstructing a phase-space correlation at the imaged plane corresponds to an offset from the virtual source by a drift distance Δz. Using equation 4.4 the distance Δz can be calculated with

$$\Delta z = \frac{\langle x\, x' \rangle_s}{\langle x'^2 \rangle_s}, \tag{6.1}$$

where index s denotes the properties at the imaged plane where the phase-space has been reconstructed. This however only considers a mismatch in the horizontally focused energy on the spectrometer screen and cannot reveal potential systematic errors in e.g. the magnet calibrations.

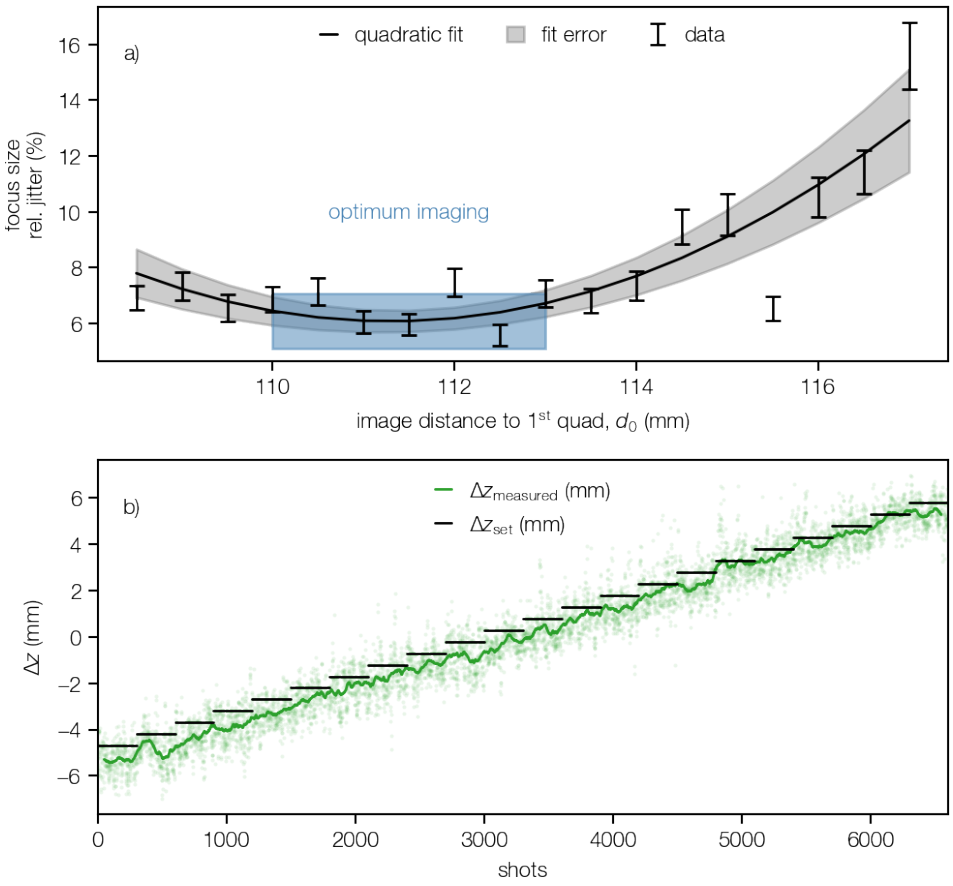

Figure 6.7. – Imaging Scan. The image plane distance from the first quadrupole is scanned. The relative jitter in horizontal focus size on screen is measured to find the optimum imaging in both planes. a) The relative jitter is smallest at an imaging plane 110 mm to 113 mm before the first quadrupole magnet. b) The offset of the imaged plane from the virtual source plane is correctly measured from the reconstructed phase-space correlation.

Therefore, another technique was developed to experminentally verify the imaging quality. In case of a mismatch between the imaged and the virtual source plane the horizontally and vertically focused energy on the spectrometer screen differ. As a consequence, the influence of the jitter of the electron beam position and beam angle from the source onto the electron focus on the spectrometer screen increases with the mismatch in horizontally and vertically focused energy. In particular, the influence of the vertical beam component increases in case of a shearing angle θ_s of the beam profile on the spectrometer screen.

The quadrupole field gradients are scanned accordingly such that different planes in the target area are imaged to the spectromter screen. The target position is not changed. The relative jitter in focus size is measured in the non-dispersive axis for different image planes. The image plane is scanned from 108 mm to 117 mm before the first quadrupole magnet. The result is plotted in figure 6.7. The full range was scanned twice with the second scan filling the intermediate steps of the first. Therefore, temporal drifts during the scan can be excluded. For each imaged plane 300 consecutive shots were detected. The relative jitter is calculated as 1 standard deviation of the measured absolute jitter in focus size devided by the mean value. The relative jitter strongly increases towards greater image distances and slightly increases towards smaller image distances below 110 mm. A quadratic fit is added to figure 6.7a to guide the eye. A minimum relative jitter in horizontal focus size is found for an image distance of 110 mm to 113 mm. This corresponds to an image plane distance with best match in horizontally and vertically focused energy. Accordingly, the result from the imaging scan is a virtual electron source position (111.5 ± 1.5) mm before the first quadrupole magnet.

However, the accuracy of the image plane scan is limited. It is used to find the smallest influence of initial beam pointing onto the detected electron focus size. The beam size on screen however is affected by multiple variables. For example a shot-to-shot jitter in initial beam size is not taken into account. The virtual electron source plane can typically only be determined with a precision of 1 mm to 2 mm. Nonetheless, a determination of the virtual electron source by ± 2 mm still ensures the horizontal and vertical focused energy to be mismatched by less than ± 2 MeV, see chapter 4.3.1. This still ensures the vertical beam size to be small at the horizontally focused energy and the single energy slices not to overlap inside the energy range of interest.

From the single shot data a virtual source position of 112.8 mm before the first quadrupole magnet was measured using equation 6.1. At this plane, the phase-space correlation is reconstructed closest to zero on average. The reconstructed distance Δz from the virtual source for the different imaged planes is plotted in figure 6.7b. The green dots denote the source plane distance reconstructed from the single shots. The green curve shows the rolling average over 100 consecutive shots. The offset from the imaged plane $d_0 - 112.8$ mm is plotted for the different quadrupole settings in black lines. The reconstructed

offset of the imaged plane from the virtual source plane is correctly measured by the reconstructed phase-space correlation.

Note that the virtual source position is located 2 mm before the second inlet position of the target. The electron beams are therefore exiting the plasma with a mean phase-space correlation. This verifies the importance of imaging scans to determine the virtual source position, respectively to allow for a correlation of the beams phase-space at the reconstructed plane. Otherwise, the virtual electron source would not be assumed to be located before (upstream) the plasma target and the electron beam would thus be imaged wrongly to the spectrometer screen (as could be the case for example in [20]).

The virtual source plane position of 112.8 mm before the first quadrupole magnet is therefore used for the quadrupole scan presented in section 6.5.

6.4. Target z-Position Scan

In a next step, the target z-position was scanned in order to test whether the virtual electron source follows the plasma target. The shift of the target in the longitudinal direction from the reference position (black) and the reconstructed shift of the virtual source plane (green) are plotted in figure 6.8. The target was only translated by in total ± 1 mm. The longitudinal focus position of the laser was not actively changed during the scan. For upstream positions of the target ($\Delta z < 0$) the reconstructed virtual source position follows the target position. For downstream positions of the target ($\Delta z > 0$) the virtual source and target position differ. For the latter case, also the shot-to-shot jitter of the reconstructed source position increases, and the beam charge and beam energy were observed to fluctuate stronger.

As the longitudinal laser focus position was not changed, the laser size and thus the laser intensity at the entrance of the plasma capillary changes with the target position. This can strongly influence the injection and acceleration processes in the plasma, which can therefore change the generated electron beam properties.

This leads to the conclusion that the virtual electron source is not only determined by the target z-position but is influenced by multiple parameters and therefore needs to be experimentally determined on a daily basis, and especially before performing emittance measurements.

6.5. Quadrupole Emittance Scan

As described in chapter 4.2.4, measuring the emittance from a single shot requires the assumption that the inital phase-space, namely the initial beam size, divergence and

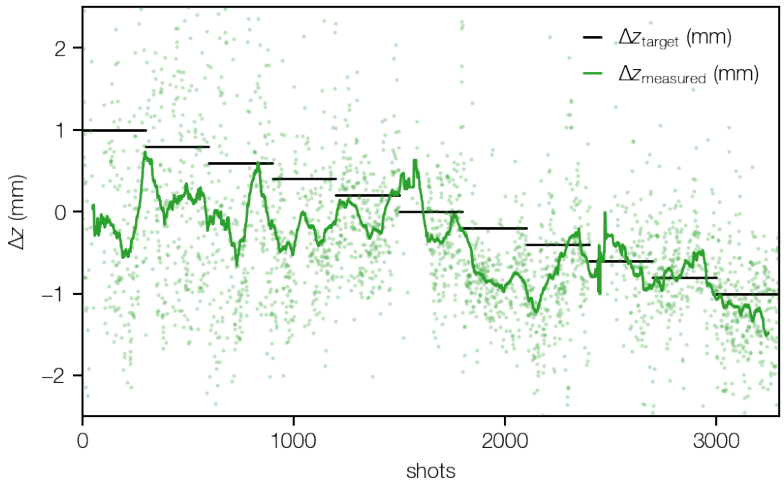

Figure 6.8. – Target z-position scan. The plasma target position is driven ±1 mm up- and downstream the beamline. The reconstructed virtual source position increases with the target position in general. However deviations are observed, in particular at downstream positions of the target.

emittance, are the same for each energy considered for the retrieval. In order to test this assumption a conventional quadrupole scan on the spectrometer screen is performed. The purpose is, for the first time, to measure the initial phase-space properties of all individual energy slices used for the single shot method.

The quadrupole field gradients are tuned such that different beam energies from the virtual source (112.8 mm before the first quadrupole) are imaged to the spectrometer screen. 31 quadrupole settings with a total scan range of ±3 % around a central energy of $E_c = 151.75\,\mathrm{MeV}$ in steps of 0.2 % were scanned. The scan range exceeds the ±2 % energy interval used for the single shot method in order to always have a clear minimum beamsize detected for each beam energy. Again, the scan range was scanned twice in order to exclude temporal drifts during the experiment. For each focused energy a series of 300 consecutive shots was acquired.

The rms beam size is measured from every single shot. Due to the broad energy spectrum of the generated electron beams, the beam size can be detected for multiple energy slices. The on average measured beam size in dependence of the focused energy and for the different energy slices is plotted in figure 6.9a. The detected "beam size map" therefore contains all information about the initial electron phase-space as well as the transport effects onto the electron phase-space. It can thus be used to compare the quadrupole-scan and the single-shot method.

The diagonal black curve shows the detected focused energy on screen. The dashed black line represents the set focused energy. The mismatch between both lines corresponds to

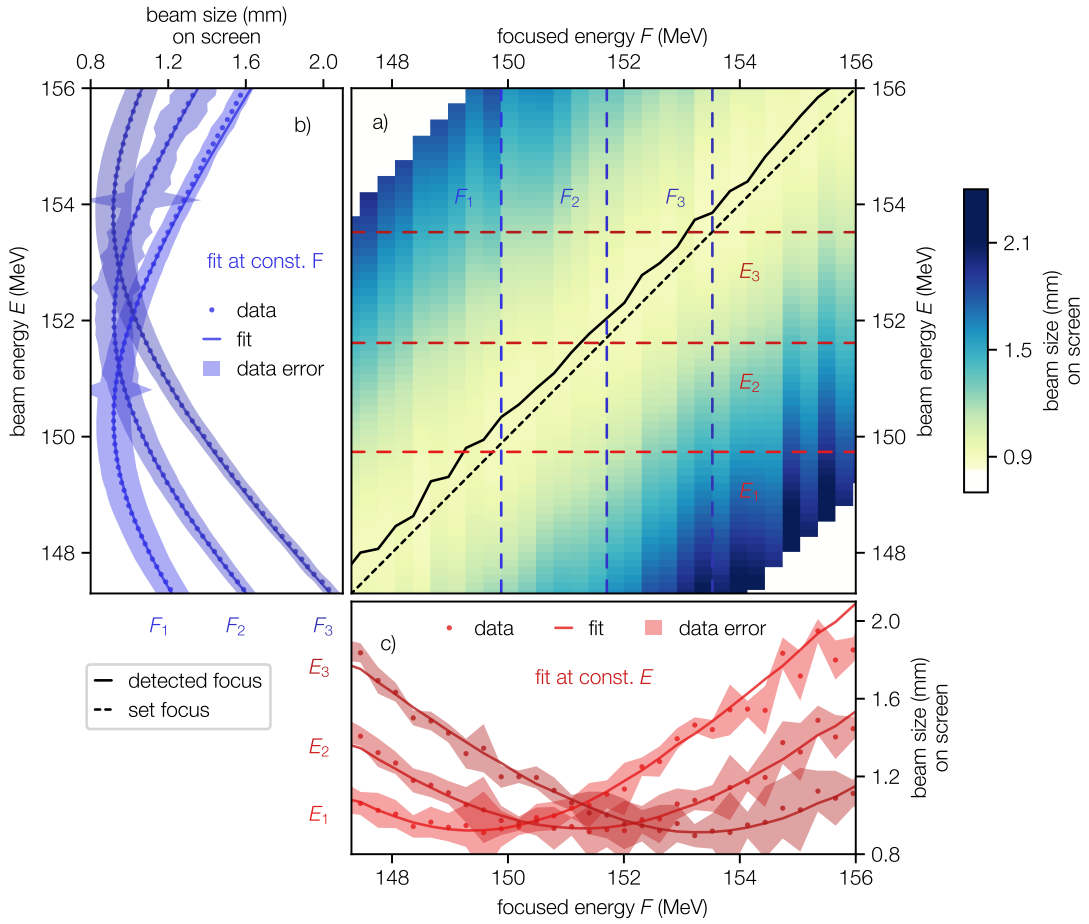

Figure 6.9. – Quadrupole scan on the spectrometer screen. a) The rms beam size on screen is detected for different focused energies F and for multiple energy slices E. The detected focused energy (black) follows the focused energy set by the quadrupole magnets (black dashed). Horizontal lineouts (red) at beam energies E_1, E_2, E_3 are used to measure the source phase-space properties with the quadruole-scan method (c). Vertical lineouts (blue) at focused energies F_1, F_2, F_3 are used to measure the phase-space with the single-shot method(a).

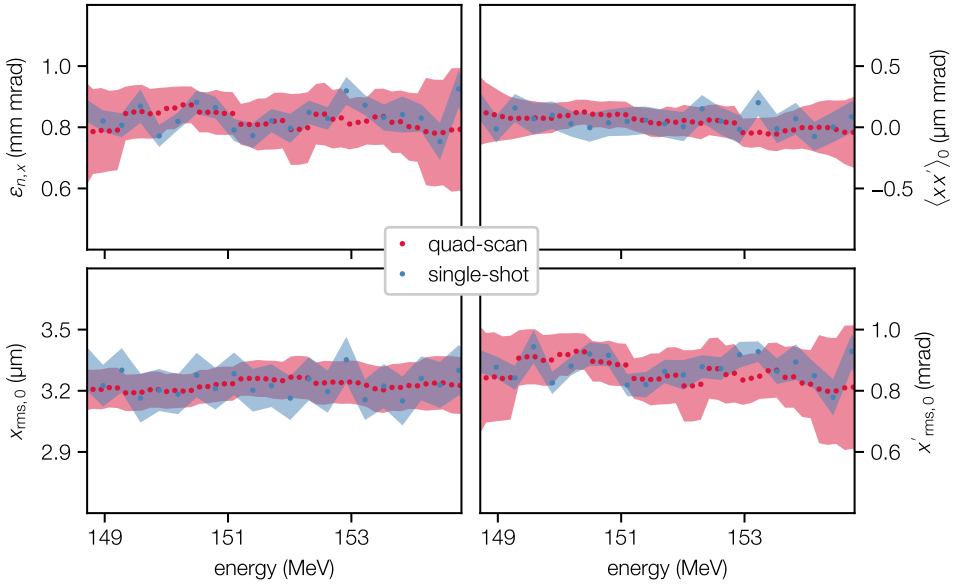

Figure 6.10. – Reconstructed phase-space properties at the source measured with a quadrupole-scan (red) and from single shots (blue). The dots denote the mean values measured for the energy-slices or the focused energy, respectively. The filled areas denote the 1 standard deviation error of the single measurements.

a residual mismatch between imaged and virtual source plane by a few 100 µm. The data from the first and second scan coincide.

In order to compare the quadrupole-scan and the single-shot method, the data from figure 6.9a is evaluated in two different ways. On the one hand, for the quadrupole-scan method, the average rms beam size on screen for a single slice energy E_i is used and equation 4.11 is fit as a function of the focused energy F. Three example energy slice lineouts E_1, E_2 and E_3 are highlighted in red, dashed horizontal lines in figure 6.9a. The rms beam size on screen for these three energy slices and the corresponding fits of equation 4.11 are plotted in figure 6.9c. However, the initial phase-space properties for all energy slices inside the plotted energy range are reconstructed with the quadrupole-scan method. Applying the quadrupole-scan method to a single energy-slice is equal to a conventional quadrupole scan of a 0.1 % full width, flat top energy spread beam.

On the other hand, for the single-shot method, the rms beam size at a single focused energy F_i can be used and equation 4.11 is fit as a function of the slice energy E. This is done for every focused energy and for each single shot. Three example lineouts at different focused energies F_1, F_2 and F_3 are highlighted in blue, dashed vertical lines in figure 6.9a. The rms beam size on screen at these three focused energies is plotted in figure 6.9b. The fit of equation 4.11 is added as a function of the slice-energy for these three focused energies.

Table 6.1. – Reconstructed average phase-space properties at the virtual source measured with the quadrupole-scan method and from single shots.

	quadrupole-scan	single-shot
$\varepsilon_{\mathrm{n,x}}$ (mm mrad)	0.82 ± 0.11	0.84 ± 0.07
x_{rms} (µm)	3.23 ± 0.10	3.22 ± 0.09
x'_{rms} (mrad)	0.86 ± 0.11	0.87 ± 0.07
$\langle x\, x' \rangle$ (µm mrad)	0.05 ± 0.15	0.05 ± 0.11

The fit results obtained from both methods as described above are plotted in figure 6.10. The phase-space properties for each energy-slice measured with the quadrupole-scan method are plotted in red and versus the slice energy. The average phase-space properties from the single-shot method measured at each focused energy are plotted in blue and versus the focused energy. The filled areas in the plots denote 1 standard deviation of the error of the reconstructed mean phase-space properties. Note, that the plotted energy range is ±2 % arround the central energy E_c which is the energy range considered for the single-shot method at the same focused energy $F = E_c$.

The plot shows the reconstructed normalized emittance (top left), the initial phase-space correlation (top right), the initial beam size (bottom left) and intital beam divergence (bottom right) at the virtual source. Inside this narrow energy interval, the energy slice phase-space properties reconstructed from the quadrupole scan are measured to be constant within the precision of the measurement[1]. The phase-space properties measured from the single shots overlap with the quadrupole-scan results.

The average beam properties over the considered energy range are listed in table 6.1 The results from both methods deviate by less than 3 %. Also the average reconstruction error from both methods is similar. As can be seen in figure 6.10, the errors in reconstructed beam size and phase-space correlation for both methods also agree on the energy-slice-level, respectively for the single focused energies. However, the error in beam divergence from the quadrupole-scan is larger than compared to the error from the single-shot measurement. At the same time, the mean beam divergence from the single-shot method is varying stronger for different focused energies than the mean divergence reconstructed for the different energy slices.

This discrepancy can be fully explained by the initial pointing of the electron beam from the plasma in the vertical axis. As discussed in chapter 4.3.4, the vertical beam pointing from the source causes an error in the reconstructed beam divergence. With the vertical pointing jitter on the ±0.5 mrad-level measured from unfocused shots, this

[1] Note that the normalized emittance, beam size, beam divergence and phase-space correlation cannot be constant with the energy at the same time. For example a 2 %-slope would be expected for at last one of the quantities inside the ±2 % energy interval. However, no *significant* change of the measured quantities is observed inside the analyzed energy range.

represents the largest error source during the experiments. The single-shot data in figure 6.10 is averaged over 300 consecutive shots for each scanned focused energy. It is thus sub-sampling the electron properties over a 5 min window and therefore also sub-samples a slow drift in vertical beam pointing. For the quadrupole-scan the average beam size from all focused energies is considered. Thus the change in electron properties over the full scan over three hours is contributing to the quadrupole-scan error.

The error in the emittance measurement is therefore 5 % to 10 % due to the vertical pointing jitter. However, the average phase-space properties measured with both the quadrupole-scan and the single-shot method agree within 3 %. This justifies the applicability of the single-shot method to measure the electron phase-space, in particular for statistical measurements, such as the average emittance and emittance stability.

Nonetheless, with the observed accuracy of the measurement, it is thus not possible to differentiate whether, for example, either the normalized or the geometric emittance from the source is constant inside this narrow energy interval. A residual energy dependence of the phase-space parameters within the error of the measurement could thus be present in the data, which, however, does not lead to a significant error in the single-shot reconstructed phase-space.

With the achieved accuracy in phase-space detection the implemented diagnostics allow for an online emittance optimization on a single-shot basis and will constitute a key tool for future laser-plasma experiements at LUX.

6.6. Phase-Space Along Energy Spectrum

In order to measure the phase-space properties from the source in a larger energy range the quadrupole magnets are tuned to scan the focused energy from 90 MeV to 190 MeV in steps of 5 MeV. As in the previous scans, the range was scanned twice and 300 consecutive shots were taken at each focused energy. The phase-space properties within a ± 2 % energy interval around the focused energy are measured with the single-shot method. The separation between the focused energies is too large to be evaluated with the quadrupole-scan method.

The retrieved phase-space properties at the focused energies are plotted in figure 6.11. The plot is organized the same as figure 6.10. The average transmitted spectrum when focusing an energy of 150 MeV from figure 6.1 is added to the plots in grey. The beam size, the beam divergence, and the normalized emittance are increasing towards lower energies. The phase-space correlation is increasing with the beam energy. This corresponds to the virtual electron source shifting downstream the beamline for higher beam energies and partially explaines the increasing beam size at the imaged plane towards lower energies. The measured emittance and divergence are not effected by a virtual source plane shift.

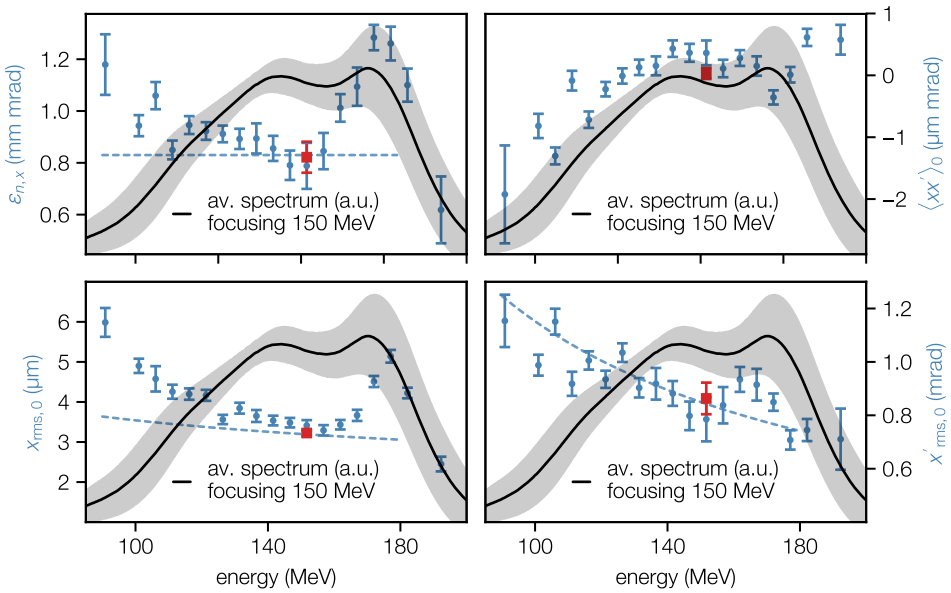

Figure 6.11. – Average single-shot phase-space properties for different focused energies (blue errorbars). The single-shot results from figure 6.10 are plotted for comparison (red errorbar). The average focused spectrum is added to the plot in grey, see figure 6.1. The phase-space properties differ at the energy-peak at $\sim 175\,\mathrm{MeV}$. The dashed lines show the energy dependences predicted by linear theory [74], compare to figure 2.8.

The single shot results from the quadrupole scan at 150 MeV discussed in the previous chapter are added to the plots in red and coincide with the data.

The beam size, the beam divergence and the normalized emittance show an increase at the peak of the energy spectrum. According to the PIC simulations in chapter 2.4, the longitudinal phase-space of the generated electron beams is positively chirped. Higher energies are therefore located at the head of the bunch, lower energies at the tail. As shown in figure 2.2, the electron beam inside the plasma is driving its own wakefield. The additional focusing forces by the beam-driven wake are acting on the tail of the electron beam, but not on the head. As a consequence, the transverse phase-space properties of the head and the tail of the electron beam can differ. The dashed lines indicate the energy dependence of the phase-space properties predicted by the theory [74] (compare to figure 2.8). Except for at the energy peak, the measured beam divergence recovers the $\gamma^{-3/4}$ energy dependence of the theory. The measured beam size out of the plasma shows a stronger dependence with the beam energy. Consequently, also the normalized emittance is measured to not be independent with the beam energy.

Further experiments are required to proof that beam-loading is the reason for the observed spectral phase-space behaviour. Additional time-resolved diagnostics, such as transition radiation spectrometers [104, 105] or transverse deflecting structures [106, 107],

could be used to further understand the mechanisms acting on the electron phase-space during acceleration.

However, the data shows that the initial phase-space emitted from the plasma does not have to be constant on a larger energy scale. It further shows, that the initial phase-space can vary with the energy and that the applicability of the single-shot method to measure the emittance must be verified for the particular experiment, the considered energy interval, and the particular injection method that is used.

6.7. Chromatic Emittance Measurements

As descibed in section 6.5 the measured "beam size map" in figure 6.9 contains the full information of the initial beam phase-space as well as the influence onto the beams phase-space by the transport optics. It can therefore be used to measure the chromatic effects on the electron beam phase-space.

A consequence of the chromatic focusing by the quadrupole doublet is that different beam energies are focused at different positions along the beamline. The distance from the longitudinal focus position to the spectrometer screen for a certain focused energy corresponds to a drift length and thus a correlation of the energy-slice phase-space at the screen. Accordingly, the beam size in the spectrometer screen plane at a certain focused energy varies with the beam energy, as has been discussed. The longitudinal spread of the electron foci in the beamline can indirectly be seen from the linear slope of the detected focused energy curve in figure 6.9 with the beam energy, respectively the focused energy.

The chromatic shearing of the energy-slice phase-spaces on the spectrometer screen is simulated using the matrix formalism. The initially uncorrelated phase-space ellipses at the source of the different energy-slices measured with the quadrupole-scan are tracked through the quadrupole doublet and into the spectrometer screen plane. The doublet is set to focus the central energy slice in the simulation. Consequently, the electron phase-space ellipses are sheared differently at the spectrometer. The simulated phase-space ellipses at the spectrometer of the central energy focused by the doublet and two slice energies with a relative energy deviation of $\pm 2\,\%$ are plotted in figure 6.12a with dashed lines. The difference in phase-space correlation $\Delta\langle x\, x'\rangle$ of the different energy-slices is plotted in figure 6.12b. The phase-space correlations are plotted relative to the correlation of the central energy that is focused by the quadrupole doublet. The chromatic correlation of the simulated phase-space ellipses linearly scales with the slice-energy.

In order to find the longitudinal focus position of a certain energy, the spectrometer screen could be shifted along the beamline until the particular energy is smallest on

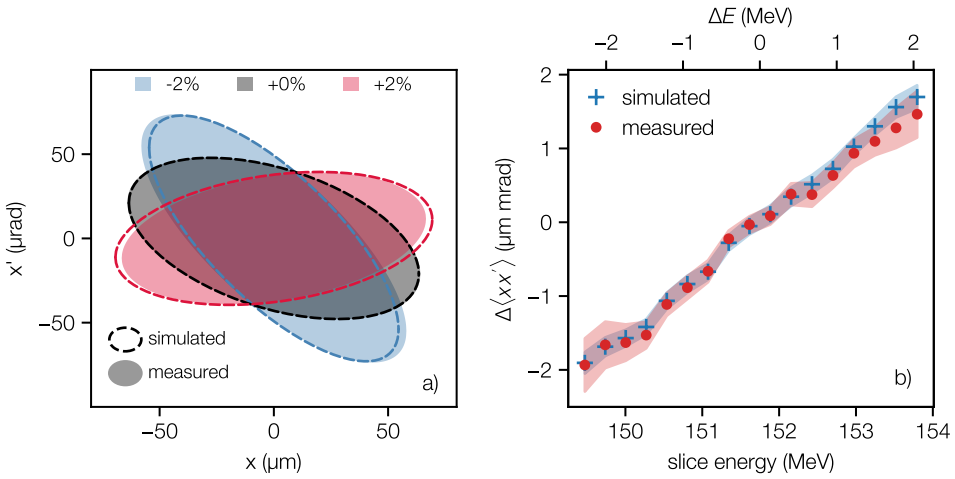

Figure 6.12. – Chromatic shearing of the energy-slice ellipses. a) Phase-space behind the quadrupole doublet. The phase-space ellipses simulated from the source to after the doublet overlap and directly measured from an energy shift ΔE of $-2\,\%$, $0\,\%$ and $2\,\%$ on the spectrometer overlap. b) Measured and simulated correlation behind the doublet for different energy-slices.

screen. Shifting the spectrometer screen is however not possible in the experiment. What is possible is a shift of the plane that is imaged by the quadrupole magnets, which is equivalent. At the same time, a shift of the image plane corresponds to a different energy being focused on the spectrometer screen. A shift of the spectrometer screen plane is thus also equivalent to considering a different energy on the spectrometer screen.

Accordingly, the quadrupole-scan method is applied while computing equation 4.11 as a function of the central energy E_c but fitting it to the data of another energy slice with energy E_i (for example an energy slice E_1 or E_3 in figure 6.9), therefore introducing an energy shift $\Delta E = E_c - E_i$.

The retrieved phase-space ellipses for a relative energy shift $\Delta E/E$ of $-2\,\%$, $0\,\%$ and $2\,\%$ are plotted additionally to figure 6.12a with filled areas. Note that figure 6.12a shows the phase-space behind the quadrupole doublet, thus the retrieved phase-space ellipses from the quadrupole-scan method have been rotated uniformly in order to match the coordinate system. The phase-space ellipses reconstructed with an energy shift on the spectrometer coincide with the simulated phase-space ellipses behind the doublet. When introducing an energy shift on the spectrometer screen, an additional phase-space correlation is reconstructed, as expected. The additional reconstructed phase-space correlation $\Delta\langle x\, x'\rangle$ for different energy-slices is added to figure 6.12b. The simulated and measured correlations overlap.

This shows, that the total chromatic correlation introduced by the beam optics can be directly measured from the spectrometer screen by applying the quadrupole-scan method

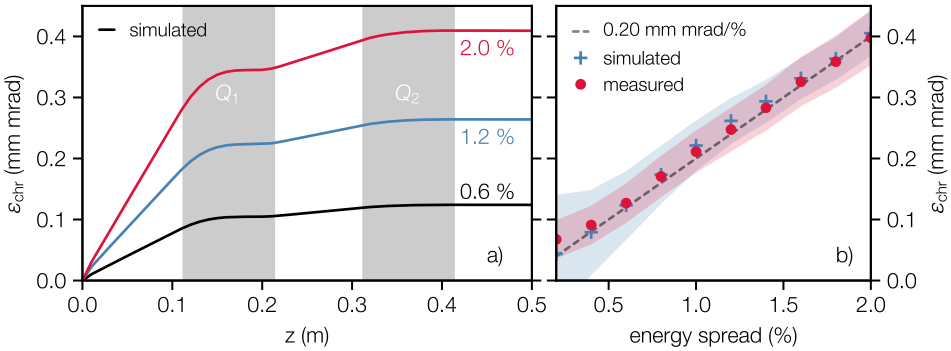

Figure 6.13. – Chromatic emittance growth. a) Simulation of the chromatic emittance evolution along the beamline for three different energy-spread beams. b) Measured and simulated chromatic emittance in dependence of the energy spread.

to an energy-slice with an energy offset ΔE. It further verifies that the chromatic effects on the electron phase-space can be directly measured from the beam size map in figure 6.9.

Accordingly, the total chromatic emittance growth imprinted by the beam transport can be measured from the data. In general, the projected beam size on a scintillator screen increases with the energy spread of the focused electron beam because different beam energies have different focus sizes in the screen plane. Since the beam energies are separated on screen by the spectrometer dipole, the projected beam size can easily be obtained by integrating the beam size over multiple energy-slices in the energy axis.

$$\langle x_{\mathrm{rms}}^2 \rangle = \frac{\int x_{\mathrm{rms}}^2 dE}{\int dE}. \tag{6.2}$$

The integration is performed over a symmetric interval arround the central energy E_c. The width of the integration interval ΔE can be freely chosen which allows to calculate the projected beam size in dependence of the energy spread.

The integrated beam size $\langle x_{\mathrm{rms}}^2 \rangle$ increases with the number of energy slices that are included in the projection. Equation 4.11 is computed as a function of the focused energy and the central energy E_c and fit to the projected beam size. The reconstructed emittance increases with the integrated energy spread. The chromatic fraction of the reconstructed projected emittance in dependence of the energy spread is plotted in figure 6.13b.

The reconstructed projected emittances are quadratically subtracted by the inital emittance of $\varepsilon_0 = 0.834\,\mathrm{mm\,mrad}$, only leaving the chromatic fraction of the emittance,

$$\varepsilon_{\mathrm{chr}} = \sqrt{\varepsilon_{\mathrm{tot}}^2 - \varepsilon_0^2}. \tag{6.3}$$

The chromatic emittance directly measured from the spectrometer linearly increases with the energy spread, as expected.

Again, the results are compared to particle tracking simulations. Random gaussian phase-space distributions are generated with the beam properties measured at the source. The particle distributions are combined and tracked through the beamline up to the spectrometer. Figure 6.13a shows the simulated evolution of the chromatic emittance along the beamline for an initial beam with 0.6 %, 1.2 % and 2.0 % full width, flat top energy spread. The chromatic emittance linearly grows in the first drift section. Inside the first quadrupole the electron beam is focused and the chromatic emittance growth is reduced. The chromatic emittance growth is finally mitigated after the second quadrupole magnet, when the beam divergence is reduced to a minimum.

The simulated chromatic emittance after the doublet is added to figure 6.13b and matches the measured data. The chromatic emittance growth rate is 0.2 mm mrad/%. In case of a 2 % energy spread beam, a chromatic emittance of 0.4 mm mrad builds up during beam transport which causes the total emittance to grow from 0.83 mm mrad at the source to 0.93 mm mrad at the spectrometer. This is a relative increase of the total emittance by only 10 %.

These numbers do of course not describe the full electron beam. As shown in figure 6.1, the width of the transmitted spectrum is far larger than the energy range analyzed with the quadrupole scan, respectively the chromatic emittance measurements. The projected emittance of the total energy spectrum inside the spectrometer is thus much larger.

However, the measurement of the energy-slices and the projected energy ranges are still correct. In particular, the presented diagnostics measures the energy-resolved phase-space properties after the plasma interaction and is therefore independent of the particular shape of the energy spectrum emitted from the plasma. Hence, in case the spectral width of the generated electron beams can be reduced to the few percent-level, for example by localizing the injection mechansim [24, 18] and using beam-loading to flatten the energy spectrum [108], the measured chromatic phase-space dynamics would still be the same.

Further, the emittance of the full energy spectrum is often not the quantity of interest for an experiment [109]. For example in case of a more complex beamline with multiple quadrupole magnets the spectral width of the initial energy spectrum that can be transported with the beam optics can narrow down to only a few %. In particular, only a small fraction of the spectrum can typically be transported with a reasonable conservation in beam quality [110]. Consequently, electrons outside the transmitted spectrum will not contribute to the phase-space available at the experiment and should therefore also not contribute to the emittance measurement.

Note, that only the chromatic emittance in the non-dispersive axis has been measured. In the other axis, where the electron beam is defocused by the first quadrupole magnet, simulations show a chromatic emittance growth 10-times larger than in the measured horizontal axis. This is on the one hand due to the first magnet increasing the divergence of the beam and the chromatic emittance quadratically scaling with the beam divergence. On the other hand, the beam is large inside the second magnet, is focused harder, and therefore experiences a greater chromaticity [111].

7. Conclusion

For this thesis, emittance measurements of laser-wakefield accelerated electron beams were performed with both a quadrupole-scan and the single-shot method first proposed by Weingartner et al. [19]. In contrast to other emittance diagnostics [32, 33, 35, 36, 37], the implemented methods at LUX enable an energy-resolved measurement of the electron phase-space. The phase-space properties of different energies in the spectrum were scanned in a narrow and a broad energy range of 6 MeV and 100 MeV, respectively.

The applicability of the single-shot method was verified for a narrow energy interval and for ionization injected beams at our setup. Inside this narrow energy range, for the first time, the phase-space of every individual energy-slice was measured using the quadrupole-scan method. No significant variation of the slice-phase-space was observed and the phase-space properties retrieved from the single-shot method and quadrupole-scan agree within 3 %.

The largest error onto the emittance measurement was identified to originate from initial beam pointing out of the plasma. The error in emittance was 5 % and 10 % with the single-shot and the quadrupole-scan method, respectively. A phase-space variation below this accuracy can therefore not be measured. The agreement of both methods results however does not imply a sensitivity of the single-shot method to a residual phase-space modulation within the measurment accuracy, if present at all.

For the analysis, a series of 31×300 consecutive shots at a repitition rate of 5 Hz had been recorded. The single-shot phase-space was measured to be constant during the 3 hour scan, which emphasizes the beam stability at the LUX accelerator and further validates the applicability of the quadrupole-scan method. An average normalized emittance of (0.83 ± 0.07) mm mrad was detected, which is roughly a factor of 2 smaller but comparable to recently published results from ionization injection [20].

Special care was taken on the theoretical description of the electron transport. Proper imaging of the electron beam from a virtual source to the spectrometer screen in both transverse axes was experimentally verified. The presented diagnostics allows to reconstruct the beam phase-space after the plasma interaction. Therefore, also a possible modulation of the phase-space by the plasma-vacuum transition is intrinsically included. The beams out of the plasma were measured to be correlated in phase-space, such that, assuming the phase-space correlation to originate from a free drift, the virtual electron

source was located 1 mm in front of the plasma target. Additionally, a shift of the virtual electron source was observed when changing the laser focus position into the plasma. It is therefore important to experimentally determine the imaging quality of the electron beams and, in contrast to an often used assumption of a non-correlated initial phase-space, to allow for an initial phase-space correlation out of the plasma.

The generated electron spectra were broadband with an average total beam charge of 20 pC. The phase-space properties for different energies in the spectrum from 90 MeV to 190 MeV were measured with the single-shot method. A complex dependence of the electron phase-space in this broader energy range was observed. Larger values of the normalized emittance, the beam size, and the beam divergence were measured at the peak of the spectrum at 175 MeV. The variation of the phase-space within the spectrum could originate from beam-loading effects. PIC simulations indicate the longitudinal phase-space of the generated electron beams to be positively correlated, therefore the head additionally focusing the tail of the beam. However, the underlaying mechanism cannot be verified with the available data and further experiments are required, for example also time-resolving the electron phase-space, such as transverse deflecting structures [106, 107] or transition radition diagnostics [104, 105].

Nonetheless, the measurements highlight that a variation of the electron phase-space over the energy spectrum can be possible. It further confirms the necessity of energy-resolved phase-space measurements for laser-wakefield accelerated beams.

Finally, the influence of the chromatic beam transport on the energy-slice phase-space was measured. By applying the quadrupole-scan method to different energy-slices on the spectrometer screen and introducing an energy shift, an additional phase-space correlation is reconstructed. This additional phase-space correlation was identified to be the total chromatic correlation that is picked up by an energy-slice during the beam transport.

By projecting the detected beam profiles on the spectrometer screen over multiple energy-slices, thus introducing an energy-spread, it was possible to reconstruct the total chromatic emittance growth imprinted by the beam transport. A linear increase of the chromatic emittance with the chosen energy-spread was observed. The results were found to be well modeled by linear beam transport theory and particle tracking simulations. In case of a 2 % energy-spread beam the emittance grows to 0.93 mm mrad, which is a relative growth of 10 %.

For the analysis of the chromatic transport effects only the narrow energy interval that was measured with the quadrupole-scan has been considered. This corresponds to only a fraction of roughly 3 % of the total spectrum, respectively of the total beam charge. Further, only the emittance in the non-dispersive axis of the spectrometer, i.e. the horizontal axis, can be measured with the presented diagnostics. According to simualtions, the chromatic emittance growth in the other axis, where the electron

beam is first defocused, is a factor of 10 larger. However, the emittance is conserved in both axes after the beam is focused by the quadrupole doublet.

Thinking of the electron beam as a driver for an experiment, it is important to measure the electron beam properties at the experiment, for example at the entrance of an undulator. The presented diagnostics enable an energy-resolved measurement of the phase-space that is available for the experiment, in particular after the plasma interaction and after beam transport. The chromatic shearing of the individual energy-slices of a multi-percent energy-spread beam can be detected. Chromaticity of the focusing optic causes the projected emittance to grow during transport. However, there are advanced beamoptic concepts, such as apochromatic lattices [110], that allow to reverse the chromatic effects on the beam phase-space under certain limitations. Here, a series of focusing optics is used to transport the beam such that the different energy-slices (almost) coinside at a single position of the beamline, i.e. at the final focus. The chromatic emittance imprinted by the beam optic can therefore in principle be reduced at this particular position in the beamline.

With the larger number of quadrupoles used for such a focusing scheme also the accurate imaging of the electron beam from the source becomes more important. In this case, the presented quadrupole-scan method can be used to experimentally determine the chromatic matching of the individual energy-slices at the final focus of an apochromatic lattice, for example with a quadrupole doublet behind the final focus, imaging the latter.

In order to quantify the chroamtic error by the beam optical elements onto the beam as a distribution the *chromatic amplitude* or *W-function* can be defined [110]. The chromatic amplitude introduced by a single quadrupole magnet approximately scales quadratically with the electron beam size inside the magnet and linearly with the quadrupole focusing strength k and quadrupole length L (see appendix C).

$$W \approx \frac{x_{\mathrm{rms}}^2 \, k \, L}{\varepsilon_x} \quad .$$

Consequently, the chromaticity of the beamoptic is mostly determined by the strongest focusing magnet (where the beam is typically largest) and, in particular, by the beam capturing section (typically with the strongest focusing strengths). At LUX, the chromaticity in the horizontal axis is therefore mostly determined by the first quadrupole magnet, and in the vertical by the second magnet. This explains the factor of 10 larger chromatic emittance in the vertical axis, due to the beam being defocused first and thus being large in the second magnet.

An apochromatic lattice can further only be used to compensate the chromatic effects for a limited energy range, which is approximately given by $1/W$ [110, 112]. For the

example of the LUX capturing optic, this limits the energy-spread of the electron beams to approximately 0.5 % to 1 %.

For many reasons, it is thus beneficial to reduce the chromaticity in the beamline. In conventional accelerators sextupole magnets in dispersive sections are typically used to compensate the chromaticity of the focusing optic [113, 114]. However, sextupole magnets are not considered as an option for state-of-the-art laser-wakefield accelerators, due to the higher complexity and non-linearity introduced to the beam transport.

A suitable approach would be to capture the beam closer to the plasma. In this case, stronger focusing is required for the shorter focal length, but, at the same time, the beam size inside the magnets reduces with the shorter drift distance. Thus the chromaticity of the capturing section linearly decreases with the distance to the plasma.
Permanent quadrupole magnets (PQM) could be used in order to achieve a higher focusing strength [115]. However, the field quality of small aperture (PQM) is typically worse than compared to conventional electro quadrupole magnets. This can in particular be problematic in the second magnet were the beam is largest. An intersting alternative would be the usage of an active-plasma-lens (APL) [116, 117, 118], since it radially focuses the beam and in addition can provide transverse field gradients on the kT-scale, thus can be installed maximum close to the plasma. However, these strong focusing fields are only reached from sub-mm-scale apertures, which raises a technical challenge when a transmission of the remaining TW-laser-pulse out of the plasma is required.

Another approach would be the reduction of the beam divergence out of the plasma. This could for example be achieved by tailoring the density downramp at the target exit [40, 39]. Reducing the beam divergence would come with the benefit of additionally suppressing the bunch lengthening along the transport optic due to different path lengths of the electrons for different offsets from the central axis.
The trivial solution of reducing the energy spread is not discussed.

However, with the calibrated phase-space diagnostics at LUX, a reliable online tool for energy-resolved emittance optimization for future experiments has been developed. Both either improving the beam divergence or reducing the chromaticity imprinted by the capturing optic can be quantified with the presented diagnostics.

A. Beam Transport

A.1. The LUX Coordinate System

The coordinate system of LUX used in this thesis is illustrated in figure A.1. The electron coordinate definitions are listed in table A.1. The laser and electron beam are propergating in positive z-direction. The Spectrometer dipole is deflecting the beam in the y-z-plane. The emittance is measured in the x-axis, which is the laser-polarization axis.

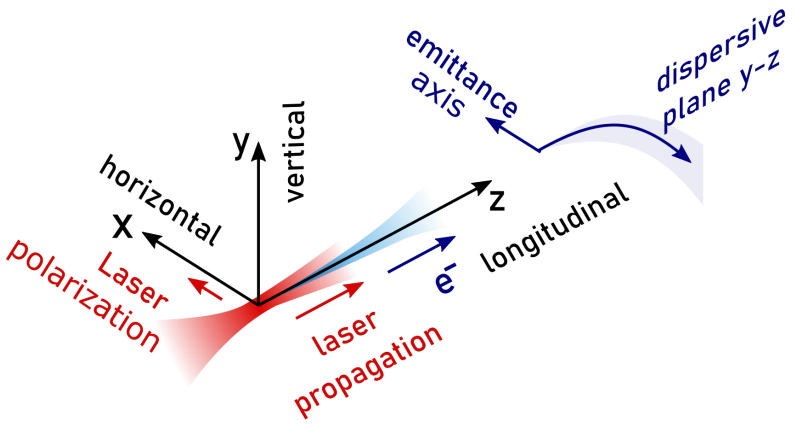

Figure A.1. – The coordinate system at LUX.

Table A.1. – Table of the coordinates.

x	horizontal position	p_x	horizontal momentum
y	vertical position	p_y	vertical momentum
z	longitudinal position	p_z	longitudinal momentum
x'	horizontal angle relative to z-axis		
y'	vertical angle relative to z-axis		

A.2. Particle Beams and Beam Transport

A.2.1. Emittance and Phase-Space

In this thesis the phase-space was defined as the x-x' space, which is often also referred to as trace-space [97]. In order to differentiate between phase-spaces, the canonical phase-space spanned by the electrons position x and the transverse canonical momentum p_x is defined. So far, only 2-dimensional phase-spaces have been discussed.

In general, an electron beam is fully described in a 6-dimensional phase-space spanned by the electrons position x, y, z, and the canonical electron momenta p_x, p_y, p_z [4]. The volume covered by the beam in this 6-dimensional phase-space is given by its statistical properties such as the variance and the correlation of the distribution between the single particle coordiantes. The electron beam is thus statistically described by the 6×6-dimensional covariance matrix $\Sigma_{6\mathrm{d}}$, which contains the second order momenta of the distribution in all possible pairs of coordinates.

$$\Sigma_{6\mathrm{d}} = \begin{pmatrix} \langle x^2 \rangle & \langle x\, p_x \rangle & \langle x\, y \rangle & \langle x\, p_y \rangle & \langle x\, z \rangle & \langle x\, p_z \rangle \\ \langle p_x\, x \rangle & \langle p_x^2 \rangle & \langle p_x\, y \rangle & \langle p_x\, p_y \rangle & \langle p_x\, z \rangle & \langle p_x\, p_z \rangle \\ \langle y\, x \rangle & \langle y\, p_x \rangle & \langle y^2 \rangle & \langle y\, p_y \rangle & \langle y\, z \rangle & \langle y\, p_z \rangle \\ \langle p_y\, x \rangle & \langle p_y\, p_x \rangle & \langle p_y\, y \rangle & \langle p_y^2 \rangle & \langle p_y\, z \rangle & \langle p_y\, p_z \rangle \\ \langle z\, x \rangle & \langle z\, p_x \rangle & \langle z\, y \rangle & \langle z\, p_y \rangle & \langle z^2 \rangle & \langle z\, p_z \rangle \\ \langle p_z\, x \rangle & \langle p_z\, p_x \rangle & \langle p_z\, y \rangle & \langle p_z\, p_y \rangle & \langle p_z\, z \rangle & \langle p_z^2 \rangle \end{pmatrix} \quad . \tag{A.1}$$

The 6d rms beam emittance is related to the 6-dimensional ellipsoid covering all electrons within 1 rms-width of the distribution. The 6-dimensional phase-space emittance is defined as the square-root of the determinant of the $\Sigma_{6\mathrm{d}}$ matrix with

$$\varepsilon_{6\mathrm{d}} = \sqrt{\det\left(\Sigma_{6\mathrm{d}}\right)} \quad . \tag{A.2}$$

Without explicitly calculating the determinant of this 6×6-matrix, it is clear that the corresponding sum will contain all possible combination of linear correlations in x, y, z, p_x, p_y and p_z. Further, this 6d emittance is always conserved within a drift section or a quadrupole magnet, since the linear correlations building up between the electron position x and the transverse and longitudinal momentum p_x and p_z are always correctly subtracted in the sum of the determinant in equation A.2.

Ontly due to the projection of the beam distribution onto a screen into 2-dimensional, respectively 4-dimension sub phase-space, the information of the other axis, i.e. the longitudinal beam properties, are lost. Accordingly, the projected emittance can grow, while the 6d emittance is conserved.

Figure A.2 illustrates the evolution in a drift section of 2-dimensional ellipses in the normalized phase-space x-x' (a) and the canonical phase-space x-p_x (b). In the foremost

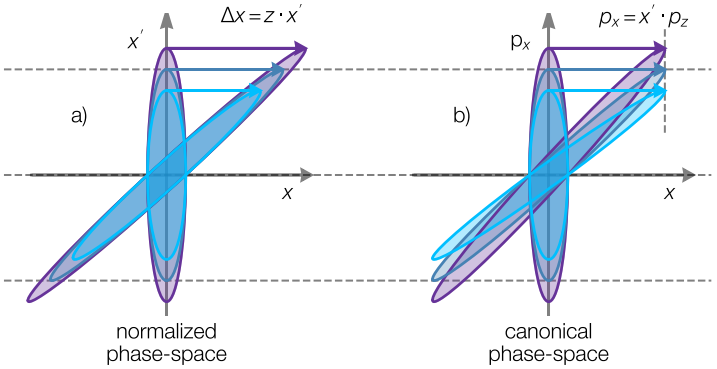

Figure A.2. – Shearing of ellipses during drift in normalized phase-space (a) and in canonical phase-space (b). The canonical phase-space emittance is not conserved in case of a large energy variation within the electron beam.

three ellipses with different initial beam divergence are plotted. Over a drift distance z, the ellipses shear coherently according to equation 4.4. Due to the normalization to the longitudinal electron momenta, the evolution in the x-x'-space is independent of the electron energy. The emittance in the x-x'-space is therefore always conserved in a drift section.

Figure A.2b shows the x-p_x-space ellipses of three beams with the same divergence but different mean energies. Here, the ellipses shear incoherently due to the difference in transverse momentum. The projected normalized emittance in canonical x-p_x phase-space

$$\varepsilon_{\mathrm{n,ph,x}} = \frac{1}{m_0 c}\sqrt{\langle x^2\rangle \langle {p_x}^2\rangle - \langle x\, p_x\rangle^2} \quad . \tag{A.3}$$

will grow with the drift space and can therefore not be conserved in case of a large energy variation within the beam. However, chromatic emittance growth is not limited to drift sections only nor to the canonical phase-space [97]. In general, it describes a mismatch between the phase-space ellipses due to energy dependent beam transport. For example, also the emittance in the x-x'-space will grow when a multi-percent energy spread beam enters a focusing section, as illustrated in figure 4.1.

A.2.2. Beam Transport

The linear motion of an electron in a magnet optic is desribed by a transport matrix M. The matrix M in general is a 6×6 matrix and is applied to the electron coordinate vector $\boldsymbol{v} = (x, x', y, y', z, \delta)^T$. δ is the relative deviation of the electrons total momentum. At LUX, the three coordinate-axis x, y, z are decoupled and the single 2×2-matrices can therefore be considered individually.

As mentioned above, only statistical beam properties such as the mean and rms of the electron distribution are accessable. The mean is defined as

$$\langle u \rangle = \frac{1}{N} \sum_{i}^{N} u_i,$$

where N denotes the total number of electrons in the distribution. The rms-width of a distribution is the square-root of the variance and defined as

$$u_{\mathrm{rms}} = \sqrt{\langle u^2 \rangle} = \sqrt{\frac{1}{N} \sum_{i}^{N} (u_i - \langle u \rangle)^2}$$

The transport of these statistical beam properties can also be expressed via a matrix multiplication. Here, the transformation is shown for the example of a 2×2 matrix, but is equivalently defined for the 6×6 case.

$$M = \begin{pmatrix} M_{11} & M_{12} \\ M_{21} & M_{22} \end{pmatrix} \qquad S = \begin{pmatrix} \langle x^2 \rangle & \langle x\, x' \rangle \\ \langle x\, x' \rangle & \langle x'^2 \rangle \end{pmatrix}$$

$$S_s = M\, S_0\, M^T$$

The above equation can be rewritten in the form

$$\begin{pmatrix} \langle x^2 \rangle_s \\ \langle x\, x' \rangle_s \\ \langle x'^2 \rangle_s \end{pmatrix} = \begin{pmatrix} M_{11}^2 & 2\, M_{11} M_{12} & M_{12}^2 \\ M_{11} M_{21} & M_{11} M_{22} + M_{12} M_{21} & M_{12} M_{22} \\ M_{21}^2 & 2\, M_{21} M_{22} & M_{22}^2 \end{pmatrix} \begin{pmatrix} \langle x^2 \rangle_0 \\ \langle x\, x' \rangle_0 \\ \langle x'^2 \rangle_0 \end{pmatrix} \tag{A.4}$$

The product above results three equations, which are the equations 4.11 to 4.13 in section 4.2.

In case of non-descrete but i.e. binned data, the mean and rms-width are calculated similarly with

$$\langle u \rangle = \frac{\sum_i^N c_i u_i}{\sum_i^N c_i},$$

$$u_{\mathrm{rms}} = \sqrt{\langle u^2 \rangle} = \sqrt{\frac{\sum_i^N c_i (u_i - \langle u \rangle)^2}{\sum_i^N c_i}},$$

where u_i are the bin positions which are weighted by the bin counts c_i.

B. Spectrometer Calibration

B.1. Spectrometer Camera Lens Distortion Coefficients

Table B.1 lists the polynomial coefficients used for the electron spectrometer lens distortion correction. These numbers are used for the pixel coordinate transformations as described in section 3.3.2.

Table B.1. – Polynomial coefficients of the electron spectrometer lens distortion correction.

symbol	cam 1	cam 2
k_1	3.308×10^{-8}	5.236×10^{-8}
k_2	3.654×10^{-14}	4.2582×10^{-14}
k_3	-5.062×10^{-20}	-1.151×10^{-19}
k_4	2.127×10^{-26}	6.627×10^{-26}
p_1	1.073×10^{-5}	6.955×10^{-7}
p_2	-5.041×10^{-6}	-3.379×10^{-6}
p_3	-1.020×10^{-7}	2.099×10^{-7}
θ_{rot}	5.593×10^{-3}	1.681×10^{-3}
c_z	1.010×0.998	0.994×0.998

C. Chromatic Amplitude

The chromatic amplitude is a measure of the chromatic error on the beam as a distribution. Following [110], the chromatic amplitude W is defined as

$$W = \sqrt{\left(\frac{\partial\alpha}{\partial\delta} - \frac{\alpha}{\beta}\frac{\partial\beta}{\partial\delta}\right)^2 + \left(\frac{1}{\beta}\frac{\partial\beta}{\partial\delta}\right)^2} \quad , \tag{C.1}$$

where α and β are the Courant-Snyder functions of the optic [4]. α is proportional to the phase-space correlation $\langle x\, x' \rangle$ and $\beta = x_{\mathrm{rms}}^2/\varepsilon$ (and equivalent for the y-axis). The derivatives are evaluated at $\delta = 0$ and δ is the relative energy deviation of the electron beam. At LUX, the largest chromatic amplitudes are given by the quadrupole magnets. A quadrupole magnet is in first order changing the beam divergence, respectively the phase-space correlation, but not changing the beam size. For example, a change in beam size is then obtained by an additional drift space behind the quadrupole magnet.

In order to approximate the chromatic amplitude of a quadrupole magnet the thin-lens approximation [4, 96] is considered, which means that the beam size inside the quadrupole is approximately constant. This is equivalent to the focal length f being much longer than the magnets length L, $f \gg L$. Note, that the quadrupole magnets at LUX are not well approximated by thin lenses, in particular $f \approx L$. However, the thin lens approximation still allows to find the most dominant dependencies of the chromatic amplitude.

Since β is approximately constant inside the quadrupole, also the change rate of β with the beam energy $\frac{\partial\beta}{\partial\delta}$ is negected. The transport matrix of a thin lens quadrupole in the focusing plane is given by

$$M_{\mathrm{thin,Q}} = \begin{pmatrix} 1 & 0 \\ -kL & 1 \end{pmatrix} \quad , \tag{C.2}$$

where k is the quadrupole focusing strength and $f^{-1} = kL$. According to equation 4.12, α_1 behind the quadrupole is

$$\alpha_1 = (kL)\beta_0 + \alpha_0 \quad , \tag{C.3}$$

where index 0 referse to the Courant-Snyder parameters in front of the quadrupole magnet. Thus the total change in α is

$$\Delta\alpha = \alpha_1 - \alpha_0 = (k\,L)\,\beta_0 \quad . \tag{C.4}$$

Accordingly, the total chromatic amplitude introduced by a single quadrupole magnet is approximately given by

$$W \approx kL\beta = \beta/f \quad . \tag{C.5}$$

Using the relation $x_{\mathrm{rms}} = \sqrt{\beta_x \, \varepsilon_x}$ this yields

$$W \approx k \, L \, x_{\mathrm{rms}}^2/\varepsilon_x \quad , \tag{C.6}$$

and equivalently for the y-axis.

Bibliography

[1] M. Altarelli, R. Brinkmann, M Chergui, W. Decking, B. Dobson, S. Düsterer, G. Grübel, W. Graeff, H. Graafsma, J Hajdu, J. Marangos, J. Pflüger, H. Redlin, D. Riley, I. Robinson, J. Rossbach, A. Schwarz, K. Tiedtke, T. Tschentscher, I. Vartaniants, H. Wabnitz, H. Weise, R. Wichmann, K. Witte, A. Wolf, M. Wulff, and M. Yurkov. Xfel technical design report. *European XFEL, Hamburg, Germany*, 2006.

[2] J Stohr. Linac coherent light source ii (lcls-ii) conceptual design report. Technical report, SLAC National Accelerator Lab., Menlo Park, CA (United States), 2011.

[3] Ties Behnke, James E. Brau, Brian Foster, Juan Fuster, Mike Harrison, James McEwan Paterson, Michael Peskin, Marcel Stanitzki, Nicholas Walker, and Hitoshi Yamamoto. The international linear collider technical design report - volume 1: Executive summary, 2013.

[4] Helmut Wiedemann. *Particle accelerator physics*. Springer, 2015.

[5] P. Schmüser, M. Dohlus, and J. Rossbach. *Ultraviolet and Soft X-Ray Free-Electron Lasers: Introduction to Physical Principles, Experimental Results, Technological Challenges*. Springer, first edition, 2008.

[6] Michael Benedikt, Daniel Schulte, and Frank Zimmermann. Optimizing integrated luminosity of future hadron colliders. *Phys. Rev. ST Accel. Beams*, 18:101002, Oct 2015.

[7] Y. Ding, A. Brachmann, F.-J. Decker, D. Dowell, P. Emma, J. Frisch, S. Gilevich, G. Hays, Ph. Hering, Z. Huang, R. Iverson, H. Loos, A. Miahnahri, H.-D. Nuhn, D. Ratner, J. Turner, J. Welch, W. White, and J. Wu. Measurements and simulations of ultralow emittance and ultrashort electron beams in the linac coherent light source. *Phys. Rev. Lett.*, 102:254801, Jun 2009.

[8] Hans Weise and Winfried Decking. Commissioning and First Lasing of the European XFEL. In *Proceedings, 38th International Free Electron Laser Conference, FEL2017*, page MOC03, 2018.

[9] A Grassellino, A Romanenko, D Sergatskov, O Melnychuk, Y Trenikhina, A Crawford, A Rowe, M Wong, T Khabiboulline, and F Barkov. Nitrogen and argon doping of niobium for superconducting radio frequency cavities: a pathway to highly efficient accelerating structures. *Superconductor Science and Technology*, 26(10):102001, aug 2013.

[10] T. Tajima and J. M. Dawson. Laser electron accelerator. *Phys. Rev. Lett.*, 43:267–270, Jul 1979.

[11] F. Grüner, S. Becker, U. Schramm, T. Eichner, M. Fuchs, R. Weingartner, D. Habs, J. Meyer-ter Vehn, M. Geissler, M. Ferrario, L. Serafini, B. van der Geer, H. Backe, W. Lauth, and S. Reiche. Design considerations for table-top, laser-based vuv and x-ray free electron lasers. *Appl. Phys. B*, 86:431–435, 2007.

[12] C. B. Schroeder, E. Esarey, C. G. R. Geddes, C. Benedetti, and W. P. Leemans. Physics considerations for laser-plasma linear colliders. *Phys. Rev. ST Accel. Beams*, 13:101301, Oct 2010.

[13] J. Faure, Y. Glinec, A. Pukhov, S. Kiselev, S. Gordienko, E. Lefebvre, J.-P. Rousseau, F. Burgy, and V. Malka. A laserâĂŞplasma accelerator producing monoenergetic electron beams. *Nature*, 431(7008):541–544, September 2004.

[14] S. P. D. Mangles, C. D. Murphy, Z. Najmudin, A. G. R. Thomas, J. L. Collier, A. E. Dangor, E. J. Divall, P. S. Foster, J. G. Gallacher, C. J. Hooker, D. A. Jaroszynski, A. J. Langley, W. B. Mori, P. A. Norreys, F. S. Tsung, R. Viskup, B. R. Walton, and K. Krushelnick. Monoenergetic beams of relativistic electrons from intense laserâĂŞplasma interactions. *Nature*, 431(7008):535–538, September 2004.

[15] C. G. R. Geddes, Cs Toth, J. van Tilborg, E. Esarey, C. B. Schroeder, D. Bruhwiler, C. Nieter, J. Cary, and W. P. Leemans. High-quality electron beams from a laser wakefield accelerator using plasma-channel guiding. *Nature*, 431(7008):538–541, September 2004.

[16] A. J. Gonsalves, K. Nakamura, J. Daniels, C. Benedetti, C. Pieronek, T. C. H. de Raadt, S. Steinke, J. H. Bin, S. S. Bulanov, J. van Tilborg, C. G. R. Geddes, C. B. Schroeder, Cs. Tóth, E. Esarey, K. Swanson, L. Fan-Chiang, G. Bagdasarov, N. Bobrova, V. Gasilov, G. Korn, P. Sasorov, and W. P. Leemans. Petawatt laser guiding and electron beam acceleration to 8 gev in a laser-heated capillary discharge waveguide. *Phys. Rev. Lett.*, 122:084801, Feb 2019.

[17] Omid zarini. *Measuring sub-femtosecond temporal structures in multi-ten kiloampere electron beams.* PhD thesis, Helmholtz-Zentrum Dresden - Rossendorf, 2019. ISSN 2191-8716.

[18] JP Couperus, R Pausch, A Köhler, O Zarini, JM Krämer, M Garten, A Huebl, R Gebhardt, U Helbig, S Bock, K. Zeil, A. Debus, M. Bussmann, U. Schramm, and A. Irman. Demonstration of a beam loaded nanocoulomb-class laser wakefield accelerator. *Nature communications*, 8(1):487, 2017.

[19] R. Weingartner, S. Raith, A. Popp, S. Chou, J. Wenz, K. Khrennikov, M. Heigoldt, A. R. Maier, N. Kajumba, M. Fuchs, B. Zeitler, F. Krausz, S. Karsch, and F. Grüner. Ultralow emittance electron beams from a laser-wakefield accelerator. *Phys. Rev. ST Accel. Beams*, 15:111302, Nov 2012.

[20] S. K. Barber, J. van Tilborg, C. B. Schroeder, R. Lehe, H.-E. Tsai, K. K. Swanson, S. Steinke, K. Nakamura, C. G. R. Geddes, C. Benedetti, E. Esarey, and W. P. Leemans. Measured emittance dependence on the injection method in laser plasma accelerators. *Phys. Rev. Lett.*, 119:104801, Sep 2017.

[21] Paul Emma, R. Akre, J. Arthur, R. Bionta, C. Bostedt, J. Bozek, A. Brachmann, P. Bucksbaum, Ryan Coffee, F.-J. Decker, Y. Ding, D. Dowell, S. Edstrom, A. Fisher, J. Frisch, S. Gilevich, J. Hastings, G. Hays, Ph. Hering, Z. Huang, R. Iverson, H. Loos, M. Messerschmidt, A. Miahnahri, S. Moeller, H.-D. Nuhn, G. Pile, , D. Ratner, J. Rzepiela, D. Schultz, T. Smith, P. Stefan, H. Tompkins, J. Turner, J. Welch, W. White, J. Wu, G. Yocky, and J. Galayda. First lasing and operation of an ångstrom-wavelength free-electron laser. *nature photonics*, 4(9):641, 2010.

[22] B. B. Pollock, C. E. Clayton, J. E. Ralph, F. Albert, A. Davidson, L. Divol, C. Filip, S. H. Glenzer, K. Herpoldt, W. Lu, K. A. Marsh, J. Meinecke, W. B. Mori, A. Pak, T. C. Rensink, J. S. Ross, J. Shaw, G. R. Tynan, C. Joshi, and D. H. Froula. Demonstration of a narrow energy spread, ~ 0.5 GeV electron beam from a two-stage laser wakefield accelerator. *Phys. Rev. Lett.*, 107:045001, Jul 2011.

[23] A. Buck, J. Wenz, J. Xu, K. Khrennikov, K. Schmid, M. Heigoldt, J. M. Mikhailova, M. Geissler, B. Shen, F. Krausz, S. Karsch, and L. Veisz. Shock-front injector for high-quality laser-plasma acceleration. *Phys. Rev. Lett.*, 110:185006, May 2013.

[24] Jérôme Faure, Clément Rechatin, A Norlin, Agustin Lifschitz, Y Glinec, and Victor Malka. Controlled injection and acceleration of electrons in plasma wakefields by colliding laser pulses. *Nature*, 444(7120):737, 2006.

[25] W. T. Wang, W. T. Li, J. S. Liu, Z. J. Zhang, R. Qi, C. H. Yu, J. Q. Liu, M. Fang, Z. Y. Qin, C. Wang, Y. Xu, F. X. Wu, Y. X. Leng, R. X. Li, and Z. Z. Xu. High-brightness high-energy electron beams from a laser wakefield accelerator via energy chirp control. *Phys. Rev. Lett.*, 117:124801, Sep 2016.

[26] Stuart PD Mangles, Alexander George Roy Thomas, Olle Lundh, Filip Lindau, MC Kaluza, Anders Persson, C-G Wahlström, Karl Krushelnick, and Zulfikar

Najmudin. On the stability of laser wakefield electron accelerators in the monoenergetic regime. *Physics of plasmas*, 14(5):056702, 2007.

[27] J. Osterhoff, A. Popp, Zs. Major, B. Marx, T. P. Rowlands-Rees, M. Fuchs, M. Geissler, R. Hörlein, B. Hidding, S. Becker, E. A. Peralta, U. Schramm, F. Grüner, D. Habs, F. Krausz, S. M. Hooker, and S. Karsch. Generation of stable, low-divergence electron beams by laser-wakefield acceleration in a steady-state-flow gas cell. *Phys. Rev. Lett.*, 101:085002, Aug 2008.

[28] Eduard Prat, Masamitsu Aiba, Simona Bettoni, Bolko Beutner, Sven Reiche, and Thomas Schietinger. Emittance measurements and minimization at the swissfel injector test facility. *Physical Review Special Topics-Accelerators and Beams*, 17(10):104401, 2014.

[29] Michiko G Minty and Frank Zimmermann. *Measurement and control of charged particle beams*. Springer Science & Business Media, 2013.

[30] B W Montague. Linear optics for improved chromaticity correction. LEP Notes - 1979, Jul 1979.

[31] A. Mostacci, M. Bellaveglia, E. Chiadroni, A. Cianchi, M. Ferrario, D. Filippetto, G. Gatti, and C. Ronsivalle. Chromatic effects in quadrupole scan emittance measurements. *Phys. Rev. ST Accel. Beams*, 15:082802, Aug 2012.

[32] S. Fritzler, E. Lefebvre, V. Malka, F. Burgy, A. E. Dangor, K. Krushelnick, S. P. D. Mangles, Z. Najmudin, J.-P. Rousseau, and B. Walton. Emittance measurements of a laser-wakefield-accelerated electron beam. *Phys. Rev. Lett.*, 92:165006, Apr 2004.

[33] E. Brunetti, R. P. Shanks, G. G. Manahan, M. R. Islam, B. Ersfeld, M. P. Anania, S. Cipiccia, R. C. Issac, G. Raj, G. Vieux, G. H. Welsh, S. M. Wiggins, and D. A. Jaroszynski. Low emittance, high brilliance relativistic electron beams from a laser-plasma accelerator. *Phys. Rev. Lett.*, 105:215007, Nov 2010.

[34] A. Cianchi, D. Alesini, M.P. Anania, M. Bellaveglia, M. Castellano, E. Chiadroni, D. Di Giovenale, M. Ferrario, A. Mostacci, P. Musumeci, R. Pompili, C. Ronsivalle, A.R. Rossi, L. Serafini, and F. Villa. Issues with phase space characterization of laser-plasma generated electron beams. *Physics Procedia*, 52:75 – 79, 2014. Proceedings of the workshop "Physics and Applications of High Brightness Beams:Towards a Fifth Generation Light Source".

[35] G. R. Plateau, C. G. R. Geddes, D. B. Thorn, M. Chen, C. Benedetti, E. Esarey, A. J. Gonsalves, N. H. Matlis, K. Nakamura, C. B. Schroeder, S. Shiraishi, T. Sokollik, J. van Tilborg, Cs. Toth, S. Trotsenko, T. S. Kim, M. Battaglia,

Th. Stöhlker, and W. P. Leemans. Low-emittance electron bunches from a laser-plasma accelerator measured using single-shot x-ray spectroscopy. *Phys. Rev. Lett.*, 109:064802, Aug 2012.

[36] A. Curcio, M. Anania, F. Bisesto, E. Chiadroni, A. Cianchi, M. Ferrario, F. Filippi, D. Giulietti, A. Marocchino, M. Petrarca, V. Shpakov, and A. Zigler. Trace-space reconstruction of low-emittance electron beams through betatron radiation in laser-plasma accelerators. *Phys. Rev. Accel. Beams*, 20:012801, Jan 2017.

[37] S. Kneip, C. McGuffey, J. L. Martins, M. S. Bloom, V. Chvykov, F. Dollar, R. Fonseca, S. Jolly, G. Kalintchenko, K. Krushelnick, A. Maksimchuk, S. P. D. Mangles, Z. Najmudin, C. A. J. Palmer, K. Ta Phuoc, W. Schumaker, L. O. Silva, J. Vieira, V. Yanovsky, and A. G. R. Thomas. Characterization of transverse beam emittance of electrons from a laser-plasma wakefield accelerator in the bubble regime using betatron x-ray radiation. *Phys. Rev. ST Accel. Beams*, 15:021302, Feb 2012.

[38] K. A. Nugent, B. Luther-Davies, and A. Perry. *Penumbral Imaging of X-Rays and Neutrons*, pages 531–544. Springer US, Boston, MA, 1986.

[39] I. Dornmair, K. Floettmann, and A. R. Maier. Emittance conservation by tailored focusing profiles in a plasma accelerator. *Phys. Rev. ST Accel. Beams*, 18:041302, Apr 2015.

[40] R. Ariniello, C. E. Doss, K. Hunt-Stone, J. R. Cary, and M. D. Litos. Transverse beam dynamics in a plasma density ramp. *Phys. Rev. Accel. Beams*, 22:041304, Apr 2019.

[41] M. Migliorati, A. Bacci, C. Benedetti, E. Chiadroni, M. Ferrario, A. Mostacci, L. Palumbo, A. R. Rossi, L. Serafini, and P. Antici. Intrinsic normalized emittance growth in laser-driven electron accelerators. *Phys. Rev. ST Accel. Beams*, 16:011302, Jan 2013.

[42] P. Antici, A. Bacci, C. Benedetti, E. Chiadroni, M. Ferrario, A. R. Rossi, L. Lancia, M. Migliorati, A. Mostacci, L. Palumbo, and L. Serafini. Laser-driven electron beamlines generated by coupling laser-plasma sources with conventional transport systems. *Journal of Applied Physics*, 112(4):044902, 2012.

[43] A. R. Maier. 24-hour operation of a laser-plasma accelerator. submitted, 2019.

[44] E. Esarey, C. B. Schroeder, and W. P. Leemans. Physics of laser-driven plasma-based electron accelerators. *Rev. Mod. Phys.*, 81:1229–1285, Aug 2009.

[45] Andreas R. Maier, Manuel Kirchen, and Florian Grüner. *Brilliant Light Sources driven by Laser-Plasma Accelerators*, pages 1–22. Springer International Publishing, Cham, 2016.

[46] A Modena, Z Najmudin, AE Dangor, CE Clayton, KA Marsh, C Joshi, Victor Malka, CB Darrow, C Danson, D Neely, and F. N. Walsh. Electron acceleration from the breaking of relativistic plasma waves. *nature*, 377(6550):606, 1995.

[47] Andrea R. Rossi, Alberto Bacci, Marco Belleveglia, Enrica Chiadroni, Alessandro Cianchi, Giampiero Di Pirro, Massimo Ferrario, Alessandro Gallo, Giancarlo Gatti, Cesare Maroli, Andrea Mostacci, Vittoria Petrillo, Luca Serafini, Paolo Tomassini, and Cristina Vaccarezza. The external-injection experiment at the sparc-lab facility. *Nuclear Instruments and Methods in Physics Research Section A: Accelerators, Spectrometers, Detectors and Associated Equipment*, 740:60 – 66, 2014. Proceedings of the first European Advanced Accelerator Concepts Workshop 2013.

[48] E. Gschwendtner, E. Adli, L. Amorim, R. Apsimon, R. Assmann, A.-M. Bachmann, F. Batsch, J. Bauche, V.K. Berglyd Olsen, M. Bernardini, R. Bingham, B. Biskup, T. Bohl, C. Bracco, P.N. Burrows, G. Burt, B. Buttenschön, A. Butterworth, A. Caldwell, M. Cascella, E. Chevallay, S. Cipiccia, H. Damerau, L. Deacon, P. Dirksen, S. Doebert, U. Dorda, J. Farmer, V. Fedosseev, E. Feldbaumer, R. Fiorito, R. Fonseca, F. Friebel, A.A. Gorn, O. Grulke, J. Hansen, C. Hessler, W. Hofle, J. Holloway, M. Hüther, D. Jaroszynski, L. Jensen, S. Jolly, A. Joulaei, M. Kasim, F. Keeble, Y. Li, S. Liu, N. Lopes, K.V. Lotov, S. Mandry, R. Martorelli, M. Martyanov, S. Mazzoni, O. Mete, V.A. Minakov, J. Mitchell, J. Moody, P. Muggli, Z. Najmudin, P. Norreys, E. Öz, A. Pardons, K. Pepitone, A. Petrenko, G. Plyushchev, A. Pukhov, K. Rieger, H. Ruhl, F. Salveter, N. Savard, J. Schmidt, A. Seryi, E. Shaposhnikova, Z.M. Sheng, P. Sherwood, L. Silva, L. Soby, A.P. Sosedkin, R.I. Spitsyn, R. Trines, P.V. Tuev, M. Turner, V. Verzilov, J. Vieira, H. Vincke, Y. Wei, C.P. Welsch, M. Wing, G. Xia, and H. Zhang. Awake, the advanced proton driven plasma wakefield acceleration experiment at cern. *Nuclear Instruments and Methods in Physics Research Section A: Accelerators, Spectrometers, Detectors and Associated Equipment*, 829:76 – 82, 2016. 2nd European Advanced Accelerator Concepts Workshop - EAAC 2015.

[49] Sébastien Corde, Cédric Thaury, Agustin Lifschitz, Guillaume Lambert, K Ta Phuoc, X Davoine, R Lehe, D Douillet, Antoine Rousse, and Victor Malka. Observation of longitudinal and transverse self-injections in laser-plasma accelerators. *Nature Communications*, 4:1501, 2013.

[50] AJ Gonsalves, Kei Nakamura, Chen Lin, Dmitriy Panasenko, Satomi Shiraishi, Thomas Sokollik, Carlo Benedetti, CB Schroeder, CGR Geddes, Jeroen Van Tilborg, J. Osterhoff, E. Esarey, C. Toth, and W. P. Leemans. Tunable laser plasma accelerator based on longitudinal density tailoring. *Nature Physics*, 7(11):862, 2011.

[51] C. G. R. Geddes, K. Nakamura, G. R. Plateau, Cs. Toth, E. Cormier-Michel, E. Esarey, C. B. Schroeder, J. R. Cary, and W. P. Leemans. Plasma-density-

gradient injection of low absolute-momentum-spread electron bunches. *Phys. Rev. Lett.*, 100:215004, May 2008.

[52] E. Oz, S. Deng, T. Katsouleas, P. Muggli, C. D. Barnes, I. Blumenfeld, F. J. Decker, P. Emma, M. J. Hogan, R. Ischebeck, R. H. Iverson, N. Kirby, P. Krejcik, C. O'Connell, R. H. Siemann, D. Walz, D. Auerbach, C. E. Clayton, C. Huang, D. K. Johnson, C. Joshi, W. Lu, K. A. Marsh, W. B. Mori, and M. Zhou. Ionization-induced electron trapping in ultrarelativistic plasma wakes. *Phys. Rev. Lett.*, 98:084801, Feb 2007.

[53] Remi Lehe, Manuel Kirchen, Igor A. Andriyash, Brendan B. Godfrey, and Jean-Luc Vay. A spectral, quasi-cylindrical and dispersion-free particle-in-cell algorithm. *Computer Physics Communications*, 203:66 – 82, 2016.

[54] C. Rechatin, X. Davoine, A. Lifschitz, A. Ben Ismail, J. Lim, E. Lefebvre, J. Faure, and V. Malka. Observation of beam loading in a laser-plasma accelerator. *Phys. Rev. Lett.*, 103:194804, Nov 2009.

[55] Timon Johannes Mehrling. *Theoretical and numerical studies on the transport of transverse beam quality in plasma-based accelerators.* PhD thesis, Hamburg U., 2014.

[56] I. Dornmair. *Advanced Beam Dynamicsand Diagnostics Concepts forLaser-Plasma Accelerators.* PhD thesis, Hamburg University, 2017.

[57] D. Strickland and G. Mourou. Compression of amplified chirped optical pulses. *Optics Communications*, 56(3):219–221, 1985.

[58] P. Maine, D. Strickland, P. Bado, M. Pessot, and G. Mourou. Generation of ultrahigh peak power pulses by chirped pulse amplification. *IEEE Journal of Quantum Electronics*, 24(2):398–403, Feb 1988.

[59] Vincent Leroux. *On the wavefront of ultrahigh intensity lasers : spatial contrast and gratings deformation.* PhD thesis, Universität Hamburg, Von-Melle-Park 3, 20146 Hamburg, 2018.

[60] A. R. Maier, S. W. Jolly, V. Leroux, and M. Schnepp. Integration of the angus 200 tw laser-system into the accelerator infrastructure at desy. In *2017 Conference on Lasers and Electro-Optics (CLEO)*, pages 1–2, May 2017.

[61] N. Delbos, C. Werle, I. Dornmair, T. Eichner, L. Hübner, S. Jalas, S.W. Jolly, M. Kirchen, V. Leroux, P. Messner, M. Schnepp, M. Trunk, P.A. Walker, P. Winkler, and A.R. Maier. Lux âĂŞ a laserâĂŞplasma driven undulator beamline. *Nuclear Instruments and Methods in Physics Research Section A: Accelerators, Spectrometers, Detectors and Associated Equipment*, 909:318 – 322, 2018. 3rd European Advanced Accelerator Concepts workshop (EAAC2017).

[62] FASTLITE. Dazzler - ultrafast pulse shaper.

[63] Pierre Tournois. Acousto-optic programmable dispersive filter for adaptive compensation of group delay time dispersion in laser systems. *Optics Communications*, 140(4):245 – 249, 1997.

[64] Frédéric Druon, Gilles Chériaux, Jérôme Faure, John Nees, Marc Nantel, Anatoly Maksimchuk, Gérard Mourou, Jean Christophe Chanteloup, and Gleb Vdovin. Wave-front correction of femtosecond terawatt lasers by deformable mirrors. *Opt. Lett.*, 23(13):1043–1045, Jul 1998.

[65] Vincent Leroux, Spencer W. Jolly, Matthias Schnepp, Timo Eichner, Sören Jalas, Manuel Kirchen, Philipp Messner, Christian Werle, Paul Winkler, and Andreas R. Maier. Wavefront degradation of a 200 tw laser from heat-induced deformation of in-vacuum compressor gratings. *Opt. Express*, 26(10):13061–13071, May 2018.

[66] Hrvoje Jasak, Aleksandar Jemcov, and Zeljko Tukovic. Openfoam: A c++ library for complex physics simulations. In *International workshop on coupled methods in numerical dynamics*, volume 1000, pages 1–20. IUC Dubrovnik Croatia, 2007.

[67] C. Werle. *First Undulator Experiments at the LUX Beamline: Towards a Plasma-Based Accelerator as a Soft X-ray Source*. PhD thesis, Universität Hamburg, 2019.

[68] A.F. Lifschitz, X. Davoine, E. Lefebvre, J. Faure, C. Rechatin, and V. Malka. Particle-in-cell modelling of laserâĂŞplasma interaction using fourier decomposition. *Journal of Computational Physics*, 228(5):1803 – 1814, 2009.

[69] Manuel Kirchen, Remi Lehe, Brendan B Godfrey, Irene Dornmair, Soeren Jalas, Kevin Peters, J-L Vay, and Andreas R Maier. Stable discrete representation of relativistically drifting plasmas. *Physics of Plasmas*, 23(10):100704, 2016.

[70] O. Buneman, C.W. Barnes, J.C. Green, and D.E. Nielsen. Principles and capabilities of 3-d, e-m particle simulations. *Journal of Computational Physics*, 38(1):1 – 44, 1980.

[71] John M. Dawson. Particle simulation of plasmas. *Rev. Mod. Phys.*, 55:403–447, Apr 1983.

[72] Sören Jalas, Irene Dornmair, Rémi Lehe, Henri Vincenti, J-L Vay, Manuel Kirchen, and Andreas R Maier. Accurate modeling of plasma acceleration with arbitrary order pseudo-spectral particle-in-cell methods. *Physics of Plasmas*, 24(3):033115, 2017.

[73] M. Santarsiero, D. Aiello, R. Borghi, and S. Vicalvi. Focusing of axially symmetric flattened gaussian beams. *Journal of Modern Optics*, 44(3):633–650, 1997.

[74] Alexander George Roy Thomas. Scalings for radiation from plasma bubbles. *Physics of Plasmas*, 17(5):056708, 2010.

[75] W. An, M. Zhou, N. Vafaei-Najafabadi, K. A. Marsh, C. E. Clayton, C. Joshi, W. B. Mori, W. Lu, E. Adli, S. Corde, M. Litos, S. Li, S. Gessner, J. Frederico, M. J. Hogan, D. Walz, J. England, J. P. Delahaye, and P. Muggli. Strategies for mitigating the ionization-induced beam head erosion problem in an electron-beam-driven plasma wakefield accelerator. *Phys. Rev. ST Accel. Beams*, 16:101301, Oct 2013.

[76] B. Krause and A. Petrov. Technical specifications version a for quadrupole xqa. Technical report, Deutsches Elektronen-Synchrotron, DESY, 2009.

[77] Group3 Technology Ltd. Mpt-141spec.doc. Technical report, Group3 Technology Ltd., Mai 2005. http://www.group3technology.com/.

[78] A. K. Jain. Harmonic coils. *CERN Accelerator School on Measurement and Alignment of Accelerator and Detector Magnets, April 1997*, 5:175–217, 1998.

[79] Nirav Yashvantray Joshi. *Design and analysis techniques for cavity beam position monitor systems for electron accelerators.* PhD thesis, University of London, 2013.

[80] Ronald Lorenz. Cavity beam position monitors. In *AIP Conference Proceedings*, volume 451, pages 53–73. AIP, 1998.

[81] D Lipka, D Nölle, M Siemens, S Vilcins, Friedhelm Caspers, M Stadler, DM Treyer, H Maesaka, and T Shintake. Orthogonal Coupling in Cavity BPM with Slots. Technical Report CERN-BE-2009-034, CERN, Geneva, May 2009.

[82] Boris Keil, R Baldinger, R Ditter, R Kramert, G Marinkovic, Patrick Pollet, M Roggli, M Rohrer, V Schlott, M Stadler, D. M. Treyer, W. Decking, D. Lipka, D. Nölle, M. Siemens, T. Traber, S. Vilcins, C. Simon, O. Napoly, N. RouviÃĺre, and J.-P. Prestel. The european xfel beam position monitor system. *Proc. IPAC*, 10:1125, 2010.

[83] Christian Wiebers, Maximilian Holz, G Kube, D Noelle, G Priebe, and H-Ch Schröder. Scintillating screen monitors for transverse electron beam profile diagnostics at the european xfel. *proceedings of IBIC*, 2013.

[84] Gero Kube, Christopher Behrens, and Werner Lauth. Resolution studies of inorganic scintillation screens for high energy and high brilliance electron beams. *Proceedings of IPAC10, Kyoto, Japan*, pages 906–908, 2010.

[85] M. MoszyÅĎski, T. Ludziejewski, D. Wolski, W. Klamra, and L.O. Norlin. Properties of the yag:ce scintillator. *Nuclear Instruments and Methods in Physics Research Section A: Accelerators, Spectrometers, Detectors and Associated Equipment*, 345(3):461 – 467, 1994.

[86] Helmholtz-zentrum dresden-rossendorf (hzdr).

[87] SENIS. Integrated 3-axis hall probe c-h3a-xx. Technical report, SENIS, Sep 2007.

[88] Hübner Lars. Single shot emittance measurements of laser-wakefield accelerated electron beams at lux. Master's thesis, Universität Hamburg, 2018.

[89] CST EM studio. http://www.cst.com.

[90] Alexander Buck, K Zeil, Antonia Popp, Karl Schmid, A Jochmann, SD Kraft, B Hidding, T Kudyakov, CMS Sears, Laszlo Veisz, S. Karsch, J. Pawelke, R. Sauerbrey, T. Cowan, F. Krausz, and U. Schramm. Absolute charge calibration of scintillating screens for relativistic electron detection. *Review of Scientific Instruments*, 81(3):033301, 2010.

[91] C Brown Duane. Close-range camera calibration. *Photogramm. Eng*, 37(8):855–866, 1971.

[92] Jason P. de Villiers, F. Wilhelm Leuschner, and Ronelle Geldenhuys. Centi-pixel accurate real-time inverse distortion correction. In John T. Wen, Dalibor Hodko, Yukitoshi Otani, Jonathan Kofman, and Okyay Kaynak, editors, *Optomechatronic Technologies 2008*, volume 7266, pages 320 – 327. International Society for Optics and Photonics, SPIE, 2008.

[93] Tru components, leuchtfolie grün (l x b x h) 138 x 34 x 0.5 mm, 2019.

[94] Michael Bass et al. *Handbook of optics.* McGraw-Hill„ 2000.

[95] Klaus Flöttmann. Astra: A space charge tracking algorithm. *Manual*, 3, Oct 2011.

[96] J. Rossbach. Basic course on accelerator optics. *CERN Accelerator Schools*, 4:1–76, 1992.

[97] Klaus Floettmann. Some basic features of the beam emittance. *Phys. Rev. ST Accel. Beams*, 6:034202, Mar 2003.

[98] Jack T Tanabe. *Iron dominated electromagnets: design, fabrication, assembly and measurements*. World Scientific Publishing Company, 2005.

[99] J Prenting, M Schlösser, A Herty, J Green, G Grzelak, A Mitra, and A Reichold. High precision survey and alignment of large linear accelerators. pages 690–692. Joint Accelerator Conferences Website (JACoW), 2017.

[100] Hubert Björn. Beam-based alignment of the lux beam optics. Master's thesis, Universität Hamburg, 2019.

[101] Heinrich Hora. Theory of relativistic self-focusing of laser radiation in plasmas. *J. Opt. Soc. Am.*, 65(8):882–886, Aug 1975.

[102] Edward Della Torre. *Magnetic hysteresis*. Wiley, 2000.

[103] Kazuhisa Nakajima, Hyung Taek Kim, Tae Moon Jeong, and Chang Hee Nam. Scaling and design of high-energy laser plasma electronÂăacceleration. *High Power Laser Science and Engineering*, 3:e10, 2015.

[104] Stephan Wesch, Bernhard Schmidt, Christopher Behrens, Hossein Delsim-Hashemi, and Peter Schmüser. A multi-channel thz and infrared spectrometer for femtosecond electron bunch diagnostics by single-shot spectroscopy of coherent radiation. *Nuclear Instruments and Methods in Physics Research Section A: Accelerators, Spectrometers, Detectors and Associated Equipment*, 665:40 – 47, 2011.

[105] O. Zarini, A. Köhler, J. Couperus, R. Pausch, T. Kurz, S. Schöbel, H. MeiÃ§ner, M. Bussmann, U. Schramm, A. Irman, and A. Debus. Advanced methods for temporal reconstruction of modulated electron bunches. In *2018 IEEE Advanced Accelerator Concepts Workshop (AAC)*, pages 1–5, Aug 2018.

[106] R Akre, P Emma, P Krejcik, and L Bentson. Bunch length measurements using a transverse rf deflecting structure in the slac linac. Technical report, Stanford Linear Accelerator Center, Stanford University, Stanford, CA 94309, 2002.

[107] Gregor Loisch, Galina Asova, Prach Boonpornprasert, Reinhard Brinkmann, Ye Chen, Johannes Engel, James Good, Matthias Gross, Florian Grüner, Holger Huck, Davit Kalantaryan, Mikhail Krasilnikov, Osip Lishilin, Alberto Martinez de la Ossa, Timon J. Mehrling, David Melkumyan, Anne Oppelt, Jens Osterhoff, Houjun Qian, Yves Renier, Frank Stephan, Carmen Tenholt, Valentin Wohlfarth, and Quantang Zhao. Observation of high transformer ratio plasma wakefield acceleration. *Phys. Rev. Lett.*, 121:064801, Aug 2018.

[108] M. Tzoufras, W. Lu, F. S. Tsung, C. Huang, W. B. Mori, T. Katsouleas, J. Vieira, R. A. Fonseca, and L. O. Silva. Beam loading in the nonlinear regime of plasma-based acceleration. *Phys. Rev. Lett.*, 101:145002, Sep 2008.

[109] A. R. Maier, A. Meseck, S. Reiche, C. B. Schroeder, T. Seggebrock, and F. Grüner. Demonstration scheme for a laser-plasma-driven free-electron laser. *Phys. Rev. X*, 2:031019, 2012.

[110] C. A. Lindstrøm and E. Adli. Design of general apochromatic drift-quadrupole beam lines. *Phys. Rev. Accel. Beams*, 19:071002, Jul 2016.

[111] Jean Buon. Beam phase space and emittance. Technical report, Paris-11 Univ., 1992.

[112] C. A. Lindstrøm. *Emittance growth and preservation in a plasma-based linear collider*. PhD thesis, Oslo University, 2019.

[113] Pantaleo Raimondi and Andrei Seryi. Novel final focus design for future linear colliders. *Phys. Rev. Lett.*, 86:3779–3782, Apr 2001.

[114] Henri Zyngier. Strategy for correcting for chromaticity. Technical report, Paris University, 1977.

[115] Paul Winkler, Dariusz Kocon, Andreas Maier, Alexander Molodozhentsev, Lukas Pribyl, and Maximilian Trunk. Measurements of High-Order Magnetic Field Components of Permanent Quadrupole Magnets for a Laser-Plasma-Driven Undulator X-Ray Source. In *Proceedings, 8th International Particle Accelerator Conference (IPAC 2017): Copenhagen, Denmark, May 14-19, 2017*, page THPIK022, 2017.

[116] J. van Tilborg, S. Steinke, C. G. R. Geddes, N. H. Matlis, B. H. Shaw, A. J. Gonsalves, J. V. Huijts, K. Nakamura, J. Daniels, C. B. Schroeder, C. Benedetti, E. Esarey, S. S. Bulanov, N. A. Bobrova, P. V. Sasorov, and W. P. Leemans. Active plasma lensing for relativistic laser-plasma-accelerated electron beams. *Phys. Rev. Lett.*, 115:184802, Oct 2015.

[117] J Van Tilborg, SK Barber, C Benedetti, CB Schroeder, F Isono, H-E Tsai, CGR Geddes, and WP Leemans. Comparative study of active plasma lenses in high-quality electron accelerator transport lines. *Physics of Plasmas*, 25(5):056702, 2018.

[118] C. A. Lindstrøm, E. Adli, G. Boyle, R. Corsini, A. E. Dyson, W. Farabolini, S. M. Hooker, M. Meisel, J. Osterhoff, J.-H. Röckemann, L. Schaper, and K. N. Sjobak. Emittance preservation in an aberration-free active plasma lens. *Phys. Rev. Lett.*, 121:194801, Nov 2018.

Acknowledgement

First of all, I would like to thank my supervisors Andreas R. Maier and Bernhard Schmidt for the extensive support during the last four years and also before.

I would also like to thank Prof. Florian Grüner for raising my interest in plasma-acceleration during his proseminar, which I got stuck with.

I would also like to thank the group members of FLA, in particular Stephan Wesch, Nils Lockmann, Steffen Wunderlich, Simon Bohlen, Kris Poder, Lukas Schaper, Gabriele Tauscher, Theresa Staufer and Maik Dinter for a fun time in 28g and in the BondLab.

I would also like to thank the technical groups at DESY, namely MEA, MKK, MDI, MVS, MCS, and the university workshops for the support during the construction phases at LUX and the too often quick fixes.

And especially, I would like to thank all LUX members, in particular Philipp Messner, Sören Jalas, Manuel Kirchen, Vincent Leroux, Spencer Jolly, Max Trunk, Matthias Schnepp, Timo Eichner, Thomas Huelsenbusch, Lars Huebner, Benno Zeitler, Chris Werle, Niels Delbos and the ones not listed for the exciting and fun times, for example cleaning flanshes, screwing flanshes, mounting chambers or climbing on racks routing cables.

I would also like to thank my dear friends Sascha, Eli, Hauke, Lukas, Bea, Kathi, Anna, Sassi, Matze and Philipp for not being physicists.

Finally I want to thank my dear family for their loving support. Thanks to you, the only thing I had to worry about during my studies and promotion were the studies and promotion itself.